Micro-mechanical Analysis of Hydrogen Assisted Damage in Metallic Microstructures

A Thesis Submitted

in Partial Fulfilment of the Requirements

for the Degree of

DOCTOR OF PHILOSOPHY

by

Vishal Singh

(2017MEZ0019)

DEPARTMENT OF MECHANICAL ENGINEERING

INDIAN INSTITUTE OF TECHNOLOGY ROPAR

January, 2024

Your Full Name: *VISHAL SINGH*

This thesis is dedicated to my teachers and parents
(For their endless love, support, and encouragement)

Declaration of Originality

I hereby declare that the work which is being presented in the thesis entitled **Micro-mechanical Analysis of Hydrogen Assisted Damage in Metallic Microstructures** has been solely authored by me. It presents the result of my own independent investigation/research conducted during the time period from January 2018 to January 2024 under the supervision of Dr. Dhiraj K Mahajan, Associate Professor, Mechanical Engineering Department. To the best of my knowledge, it is an original work, both in terms of research content and narrative, and has not been submitted or accepted elsewhere, in part or in full, for the award of any degree, diploma, fellowship, associateship, or similar title of any university or institution. Further, due credit has been attributed to the relevant state-of-the-art and collaborations (if any) with appropriate citations and acknowledgments, in line with established ethical norms and practices. I also declare that any idea/data/fact/source stated in my thesis has not been fabricated/ falsified/ misrepresented. All the principles of academic honesty and integrity have been followed. I fully understand that if the thesis is found to be unoriginal, fabricated, or plagiarized, the Institute reserves the right to withdraw the thesis from its archive and revoke the associated Degree conferred. Additionally, the Institute also reserves the right to appraise all concerned sections of society of the matter for their information and necessary action (if any). If accepted, I hereby consent for my thesis to be available online in the Institute's Open Access repository, inter-library loan, and the title & abstract to be made available to outside organizations.

Signature *Vishal Singh*

Name: Vishal Singh

Entry Number: 2017MEZ0019

Program: PhD

Department: Mechanical Engineering

Indian Institute of Technology Ropar

Rupnagar, Punjab 140001

Date:16/01/2024

Acknowledgement

Certificate

This is to certify that the thesis entitled **Micro-mechanical Analysis of Hydrogen Assisted Damage in Metallic Microstructures**, submitted by **Vishal Singh (2017MEZ0019)** for the award of the degree of **Doctor of Philosophy** of Indian Institute of Technology Ropar, is a record of bonafide research work carried out under my (our) guidance and supervision. To the best of my knowledge and belief, the work presented in this thesis is original and has not been submitted, either in part or full, for the award of any other degree, diploma, fellowship, associateship or similar title of any university or institution.

In my (our) opinion, the thesis has reached the standard fulfilling the requirements of the regulations relating to the Degree.

Signature of the Supervisor(s)

Dr. Dhiraj K. Mahajan

Department of Mechanical Engineering

Indian Institute of Technology Ropar

Rupnagar, Punjab 140001

Date:16/01/2024

Lay Summary

The presence of hydrogen in metallic materials diminishes their structural durability, rendering them more prone to failure. This poses a significant challenge in the safe storage and transportation of hydrogen within metallic structures. Although various material-specific micro-level mechanisms have been proposed in recent years, the precise mechanism responsible for material failures in hydrogen-rich environments continues to remain elusive. This research is focused on elucidating the micro-mechanics of how hydrogen affects the durability of metals, with a specific emphasis on nickel and pipeline steel materials. In this work, a combination of computer simulations and experimental investigations is employed to explore the diverse micro-level, material-specific mechanisms through which hydrogen can lead to a loss of structural durability. As the first task of this research, computer simulations are conducted, centering around one of the many mechanisms known as the 'hydrogen enhanced localized plasticity (HELP)', by which hydrogen can lead to premature failure of metals under externally applied tensile loads. In the second task of this work, a unique type of specially designed tensile specimens, known as 'tensile oligocrystals', containing nearly one layer of grains along the thickness direction, is employed to investigate the effect of hydrogen on the failure behavior of nickel material. To gain a comprehensive understanding of the failure behavior of these oligocrystals during tensile deformation under a hydrogen atmosphere, the experimental results are first conducted and then corroborated through computer simulations. Unlike in nickel, exposure of pipeline steels to a hydrogen environment results in near-surface damage (cracks and blisters) even in the absence of externally applied loads. In the third objective, the effect of these hydrogen charging-induced cracks/blisters on tensile as well as fatigue crack growth behavior in pipeline X65 grade steel is investigated experimentally. This thesis work contributes to the development of a material-specific, micro-level understanding of hydrogen-induced premature failures in metals and alloys.

Abstract

Hydrogen-induced loss in structural integrity of metallic materials is a major obstacle to the future of sustainable and eco-friendly hydrogen-based energy solutions. The intricate interplay between the small size of hydrogen and its complex interaction with microstructural constituents poses formidable challenges in characterizing the site-specific role of hydrogen in the microstructure. Consequently, despite years of research, a common understanding of the underlying mechanism contributing to hydrogen-assisted damage remains elusive. As a major part of this thesis work, both numerical simulations and experimental investigations are used to elucidate the underlying micro-mechanisms responsible for hydrogen embrittlement (HE) in Nickel. As the first objective in the present work, a numerical framework comprising the crystal plasticity model coupled with the hydrogen transport model is used to understand the possible failure scenarios emanating from the hydrogen-enhanced localized plasticity (HELP) mechanism of HE. In this two-way numerical framework, while deformation affects hydrogen redistribution, the effect of hydrogen concentration on dislocation activities is also considered. This first study helped in understanding the mico-mechanics of HE possible under the proposition of the HELP mechanism. In the second objective, an oligocrystal approach is employed to study the transition in failure mode from ductile transgranular to HE-induced brittle intergranular fracture in nickel. To discern the exact role of hydrogen, at first different types of tensile oligocrystals are tested at different strain rates. Thereafter these experimental results are corroborated with a coupled crystal plasticity and phase field fracture model. This combined experimental and numerical approach rationalized the reduction in grain boundary cohesion energy to promote intergranular fracture in H-charged oligocrystals, particularly along the random high-angle grain boundaries (RHAGBs).

Similar to the other metallic materials, the hydrogen-rich service environment results in HE in pipeline steels. However, one of the uncertainties associated with evaluating the HE sensitivity of pipeline steels is their high susceptibility to hydrogen-induced blistering/cracking (HIC). In the third and final objective, the role of hydrogen charging-induced blisters on tensile as well as short fatigue crack growth behavior in pipeline X65 grade steel is investigated experimentally. The results in this work highlight the significant contribution of hydrogen-induced blisters (developed during the hydrogen-charging process prior to mechanical loading) in expediting the loss of structural integrity during the external mechanical loading of hydrogen-charged samples.

This thesis work contributes not only to the advancement of the mechanics of materials understanding but also to the development of innovative strategies, ultimately fostering the understanding required for a more sustainable and hydrogen-based energy economy.

Keywords: Hydrogen embrittlement, Hydrogen induced cracking, Oligocrystals, Crystal plasticity, Phase-field, Hydrogen diffusion

List of Publications

Journal Publications

- **Vishal Singh**, Rakesh Kumar, Yann Charles, Dhiraj K. Mahajan, Coupled diffusion-mechanics framework for simulating hydrogen assisted deformation and failure behavior of metals, *International Journal of Plasticity*, 157, 2022, 103392.

- **Vishal Singh**, Rajwinder Singh, Kanwer Singh Arora, Dhiraj K. Mahajan, Hydrogen induced blister cracking and mechanical failure in X65 pipeline steels, *International Journal of Hydrogen Energy*, 44(39), 2019, 22039-22049.

- **Vishal Singh**, Aswin Raj, Dhiraj K. Mahajan, Investigation into hydrogen assisted fracture in Nickel oligocrystals. *(Under review)*

- Rajwinder Singh, **Vishal Singh**, Aman Arora, Dhiraj K. Mahajan, In-situ investigations of hydrogen influenced crack initiation and propagation under tensile and low cycle fatigue loadings in RPV steel, *Journal of Nuclear Materials*, 529, 2020,151912.

Conference Proceedings

- **Vishal Singh**, Rajwinder Singh, Amanjot Singh, Dhiraj K.Mahajan, Tracking hydrogen embrittlement using short fatigue crack behavior of metals. Presented in ECF22 held from 26. to 31. August, 2018. in Belgrade, Serbia.

- **Vishal Singh**, Kanwar S. Arora, Dhiraj K. Mahajan, Investigation into hydrogen-induced blister cracking and mechanical failure in pipeline steels. Presented in 3rd International Conference - Structure Integrity Conference and Exhibition 2020.

- **Vishal Singh**, Rakesh Kumar, Dhiraj K. Mahajan, Phase field modeling of crack propagation in crystalline microstructures under hydrogen atmosphere, Oral presentation in 3rd International Conference - Structure Integrity Conference and Exhibition 2020.

Contents

List of Figures

List of Tables

Nomenclature & Abbreviations

α	Slip system index
∇	Gradient operator
$\boldsymbol{\sigma}$	Cauchy stress
$\chi_{\alpha\beta}$	Taylor coefficient matrix
$\Delta\sigma$	Stress range
$\dot{\gamma}^{\alpha}$	Slip rate on α slip system
$\dot{\rho}^{\alpha}$	Rate of dislocation density evolution
η^{α}	Internal state variable for accumulated slip on α slip system
γ_{acc}^{α}	Accumulated slip on the α slip system
$\hat{\psi}^{e}$	Elastic strain energy of the intact material
$\hat{\psi}^{p}$	Stored plastic energy due to defect formation
$\mathcal{C}$	Fourth-order elastic stiffness tensor
μ_L	Chemical potential of lattice hydrogen
μ_L^0	Reference lattice chemical potential
ω	Angle between the grain boundary plane normal and the tensile axis
ϕ	Phase field parameter
ϕ_{rgb}	Phase field for regularizing material properties at grain boundary
ψ	Total internal free energy for a damaged material
ψ^{e}	Elastic contribution to free energy
ψ^{p}	Plastic contribution to free energy
ψ^{ϕ}	Fracture contribution to free energy
ρ^{α}	Dislocation density on α slip system
σ_f	Flow stress
σ_N	Grain boundary normal stress
τ^{α}	Resolved shear stress along the α slip system

τ_c^α	Critical resolved shear stress on α slip system
τ_f^α	Initial slip resistance on the α slip system
$\boldsymbol{J}$	Hydrogen flux
$\mathbf{C}$	Right Cauchy Green deformation tensor
$\mathbf{E}^e$	Elastic Green–Lagrange strain tensor
$\mathbf{F}$	Total deformation gradient
$\mathbf{F}_e$	Elastic deformation gradient
$\mathbf{F}_p$	Lattice-preserving inelastic deformation gradient
$\mathbf{I}$	Identity tensor
$\mathbf{L}$	Velocity gradient
$\mathbf{L}_e$	Elastic distortion-rate tensor
$\mathbf{L}_p$	Plastic distortion-rate tensor
$\mathbf{S}$	Second Piola-Kirchhoff stress
$\boldsymbol{m}^\alpha$	Orthonormal vector normal to slip plane on α Slip System
$\boldsymbol{s}^\alpha$	Orthonormal vector in the direction of slip on α slip system
θ_L	Occupancy of hydrogen atoms in lattice sites
θ_T^α	Occupancy of hydrogen in dislocations at the α slip system
ζ_b^α	Back stress on the α slip system
b	Burgers vector length
c_1	Material-dependent first constant for back stress evolution
c_2	Material-dependent second constant for back stress evolution
C_L	Hydrogen concentration in lattice sites
C_T	Total hydrogen concentration trapped by dislocations
C_T^α	Hydrogen concentration trapped by dislocations along the α slip system
C_{Tot}	Total hydrogen concentration
D_L	Lattice diffusion coefficient for hydrogen
$g(\phi)$	Phase field fracture degradation function

G_c	Griffith-type energy release rate
$h(\phi_{rgb})$	Grain boundary phase field interpolation function
k_c	Constant related to hydrogen effect on dislocation annihilation rate
k_{annih}	Dislocation annihilation parameter
k_{annih}^H	Dislocation annihilation rate with hydrogen effect
k_{multi}	Dislocation multiplication parameter
k_{multi}^H	Dislocation multiplication rate with hydrogen effect
l_c	Constant related to hydrogen effect on dislocation multiplication rate
l_ϕ	Length scale parameter for phase-field fracture
l_{rgb}	Length scale parameter for grain boundary phase field
m_{avg}	Average Schmid factor
m_{g1}	Schmid factor of grain 1 adjacent to the grain boundary
m_{g2}	Schmid factor of grain 2 adjacent to the grain boundary
n	Strain-rate sensitivity constant
N_L	Number of lattice sites
N_s	Total number of slip systems
N_T^α	Trap density along the α slip system
R	Universal gas constant
R_A	Reduction in the cross-sectional area uncharged sample
R_H	Reduction in the cross-sectional area H-charged sample
T	Absolute temperature
$T(\phi)$	Threshold energy for fracture initiation
v_0	Reference velocity
V_H	Partial molar volume of hydrogen in metals
w_c	Specific fracture energy per unit volume
w_m	Specific fracture energy of matrix
w_{rgb}	Specific fracture energy at grain boundaries

API	American Petroleum Institute
BCC	Body-Centered Cubic
BWC	Blister Wall Cracks
CP	Crystal Plasticity
CZM	Cohesive Zone Models
DDP	Discrete Dislocation Plasticity
EBSD	Electron Backscatter Diffraction
EDS	Energy-Dispersive X-ray Spectroscopy
FCC	Face-Centered Cubic
FEM	Finite Element Method
GNB	Geometric Necessary Boundary
GROD	Grain Reference Orientation Deviation
HEI	Hydrogen Embrittlement Index
HIC	Hydrogen-Induced Cracking
IDB	Incidental Dislocation Boundary
LAGB	Low Angle Grain Boundary
LEFM	Linear Elastic Fracture Mechanics
M/A	Martensite/Austenite
NACE	National Association of Corrosion Engineers
PFM	Phase Field Fracture Model
RHAGB	Random High-Angle Grain Boundaries
SEM	Scanning Electron Microscope
SENT	Single Edge Notch Tension
SKPFM	Scanning Kelvin Probe Force Microscopy
SMGBS	Schmid-Modified Grain Boundary Stress
SRF	Slip-Rate Factor
TEM	Transmission Electron Microscopy

UEL	User Defined Element
UMAT	User defined Material
UMATHT	User defined Material for Heat Transfer
w-EDM	Wire Electron Discharge Machine
XFEM	Extended Finite Element Method

Chapter 1

Introduction

1.1 Introduction

In the pursuit of sustainable and eco-friendly energy solutions, hydrogen-based energy emerges as a promising contender. The growing significance of hydrogen in the worldwide energy landscape is evident from its increasing proportion in the overall final energy usage. In 2020, hydrogen constituted a mere fraction, less than 0.1%, but projections indicate that it is poised to escalate to 2% by 2030 and a noteworthy 10% by 2050 [2, 3, 4]. The rising adoption of hydrogen-based energy solutions requires cost-effective materials that can facilitate the safe production, storage, and transportation of hydrogen; which otherwise is a major challenge due to decades-old known problem of hydrogen-induced damage to metallic materials [5, 6, 7]. Atomic hydrogen readily dissolves in most metallic materials and results in the loss of structural integrity of these materials. The degradation of metallic materials induced by hydrogen was first observed by Johnson in 1874 [8] and validated by Reynolds one year later [9]. Since then, extensive research has been conducted, and various explanations have been provided regarding the phenomenon of hydrogen-assisted degradation of metallic materials [5].

Dissolved atomic hydrogen in metal and alloys can induce a transition in fracture mode during external loading from ductile to brittle, a phenomenon called hydrogen embrittlement (HE). Hydrogen dissolved in metallic microstructure resides at normal interstitial lattice sites and defect sites (such as dislocations, vacancies, grain boundaries, carbides, and inclusion interfaces). Depending upon the concentration and interaction of hydrogen with the various defect sites, different HE mechanisms are proposed [5, 10]. In non-hydride-forming metals, modern research has identified hydrogen-enhanced decohesion (HEDE) and hydrogen-enhanced localized plasticity (HELP) as the two most important mechanisms responsible for HE. As per the HEDE mechanism, the reduction in metallic bond strength induced by high hydrogen concentrations at crack tips, grain/phase boundaries, and interfaces leads to brittle fracture [11, 12]. The HELP mechanism suggests that hydrogen enhances dislocation mobility by the shielding or screening effect of hydrogen on dislocations [13, 14]. The enhanced mobility of dislocations caused by hydrogen is believed to increase dislocation densities, accelerate the formation of localized shear bands, and influence void nucleation, growth, and coalescence, ultimately leading to the development of premature brittle fracture. In recent years, there have been discussions regarding the synergistic effect of more than one mechanism, such as HELP and HEDE, which can operate simultaneously or where HELP may promote the HEDE mechanism in

governing HE [5, 7, 15, 16].

At certain defect sites (such as grain boundaries, and matrix-inclusion interfaces), dissolved atomic hydrogen accumulates, recombines, and precipitates the gaseous hydrogen molecules when the hydrogen solubility limit of the material is reached. This precipitation creates an incipient crack/blister, and the growth of this crack/blister is propelled by the pressure of hydrogen gas trapped within it. This kind of hydrogen atmosphere-induced damage of metals (in the absence of externally applied stress), where the driving force for crack propagation is molecular hydrogen pressure build-up within the crack is called Hydrogen-induced cracking (HIC) [17]. National Association of Corrosion Engineers (NACE) specifically states that the term HIC covers the now obsolete terms of step-wise cracking, hydrogen-induced step-wise cracking, blister cracking, and hydrogen pressure cracking [17].

The process of HE, in general, requires an applied force and does not generally have hydrogen gas precipitation within the material. Moreover, HE affects various classes of metals, whereas hydrogen-induced cracking (HIC) is primarily a concern in non-austenitic steels [5, 17]. Other metals/alloys typically do not exhibit HIC unless they are exposed to extremely aggressive electrochemical hydrogen charging. Unlike the HE effect, where materials may still perform in a ductile manner once hydrogen is removed, HIC is irreversible. In HIC, cracks or blisters, once formed, will remain there even after the removal of hydrogen. Though the process of HE and HIC is different, HE likely plays a crucial role in the HIC process. On the other hand, the molecular hydrogen-induced cracks and blisters are likely to act as potential sites of stress concentration during mechanical loading thus altering the H-redistribution locally favorable for intensifying localized activated HE mechanism. However, the integration of the HIC and HE toward the overall H-assisted degradation of metals is the least investigated.

The small size of hydrogen atoms poses significant challenges to precisely characterize the site-specific presence of hydrogen dissolved in the microstructure. Moreover, the intricate dependence of hydrogen trapping and diffusion behavior on micro-mechanical factors (such as grain size, orientation, grain boundary type, and loading conditions) further makes the comprehension of H-assisted damage mechanics extremely challenging. To address these challenges, one appropriate approach is to investigate H-metal interaction using numerical simulations at diverse length scales. The length scale associated with the crystal plasticity models makes it a more suitable choice to simulate individual contribution or synergistic effect of multiple H-assisted mechanisms under different loading conditions [18, 19, 20, 21]. Crystal plasticity models can be readily informed with insights gained from atomistic and discrete dislocation dynamics simulations as well as from experimental analysis. Therefore, to gain a comprehensive understanding of H-metal interaction toward H-assisted degradation under different micro-mechanical conditions, the use of crystal plasticity models coupled with hydrogen transport models and/or appropriate fracture models seems to be a valuable and promising approach [18, 22]. Another promising approach to comprehending the complex H-metal interaction could be the use

of advanced characterization tools with relatively simple microstructural configurations, such as bi-crystals and/or oligocrystals.

1.2 Scope and outline of thesis

Due to its relatively simple microstructure and its non-susceptibility to HIC under moderate H-charging conditions, Nickel (Ni) as the material model is extensively used to investigate the fundamentals of HE. In the polycrystalline configuration, Ni manifests the HE by a transition of fracture mode from ductile transgranular (TG) to brittle intergranular (IG) [5, 15, 18, 23, 24]. There are discussions on the role of individual or concurrent activity of HE mechanisms (such as HELP or HEDE, HELP+HEDE, HELP mediated HEDE among others) responsible for IG fracture, each with a magnitude governed by local factors, such as hydrogen content, strain rate, testing temperature and crystallographic texture among other [5, 7, 15, 25, 23]. However, despite many years of research, the exact micro-mechanics of HE responsible for IG fracture in Ni is debatable and still open for research. Hence, a major part of this work is dedicated to investigating the possible scenarios of IG fracture due to HE in Ni material using novel numerical and experimental strategies.

Pipelines are considered a safe and economical means for the transportation of oil and gas. Similar to the other metallic materials, the hydrogen-rich service environment can result in HE in pipeline steels [5, 26, 27, 28]. However, one of the uncertainties associated with measuring and evaluating the hydrogen embrittlement (HE) sensitivity of pipeline steels is their high susceptibility to hydrogen-induced cracking (HIC) [27, 29, 30]. As the second part of the present work, the integration of HE and HIC toward the tensile and fatigue behavior is investigated for a pipeline steel X65 grade. This thesis work forwards the novel simulation and experimental strategies to investigate the H-metal interaction in metallic materials under different scenarios. The three objectives of the present work are defined as,

1. Development of a computational framework consisting of dislocation density-based crystal plasticity coupled with slip-rate-based hydrogen trapping model to simulate two-way effect i.e. the role of local microstructural deformation on hydrogen distribution and vice-versa.

2. Investigation into hydrogen assisted intergranular fracture in Ni using oligocrystal approach.

   - Experimental investigation of Hydrogen embrittlement in Ni oligocrystals.

   - Development of a computational framework for simulating tensile fracture behavior for uncharged and H-charged oligocrystals.

3. Investigation toward the hydrogen-induced blister cracking and mechanical failure in X65 pipeline steels.

These three research objectives of the present work are structured and elaborated upon across seven chapters, as outlined below:

In **Chapter 1**, a general introduction, scope, and layout of the thesis are provided.

Chapter 2 is focused on Objective 1, dedicated to developing a computational finite element framework for investigating the possible hydrogen embrittlement (HE) scenarios arising from the interaction between hydrogen and dislocations under the proposition of the HELP mechanism of HE. The developed computational framework comprises a dislocation density-based crystal plasticity model coupled with a slip rate-based hydrogen diffusion/trapping model to simulate the two-way effect. In the two-way effect, while hydrostatic stresses and dislocation density affect the hydrogen re-distribution in microstructure; hydrogen trapped at the dislocations affects the interaction strength and multiplication/annihilation behavior of dislocations. This framework is implemented using the UMAT (User-defined Material) and UMATHT (User-defined Material with Heat Transfer) subroutines in commercial finite element solver Abaqus. UMAT is used to solve the dislocation density-based crystal plasticity model, whereas UMATHT is used to solve the hydrogen transport model. The material model presented is calibrated against experimental tensile stress-strain data for Nickel single crystals oriented for a single slip system (both for the uncharged and hydrogen-charged cases) using an inverse identification algorithm. A material model with calibrated constants is thereafter extended to simulate the hydrogen effect on the tensile behavior of single crystal oriented for multi-slip and then polycrystal configurations. The results are discussed in terms of the potential contributions from the HELP mechanism of HE in Nickel material failure.

Chapter 3 is focused on the first part of objective 2. This chapter includes an experimental study aimed at examining the HE behavior of Nickel-201 alloy through the use of miniaturized tensile oligocrystal samples. To understand the role of microstructure in HE behavior, various types of tensile oligocrystals (True-oligocrystals, Quasi-oligocrystals, Identical-oligocrystals, and Bi-crystal type oligocrystals) with different microstructure (in terms of Schmid factor distribution and grain boundary types) are generated using the combination of heat treatment and slicing method. Some of these oligocrystals are then exposed to the electrochemical H-charging method to introduce hydrogen. All the specimens (hydrogen-charged and uncharged) are deformed with a constant strain rate using the mini-tensile machine. Electron backscatter diffraction (EBSD) analysis and fractographic investigation are conducted to make a one-to-one correlation between the microstructure and HE mechanisms. By employing the novel identical oligocrystal approach, the macroscopic tensile stress-strain response and microscopic fracture pattern of both hydrogen-free and hydrogen-charged conditions are compared to provide captivating insights into the H-effect on fracture behavior. The bi-crystal type oligocrystal samples are tested to investigate the unique contribution of each type of grain boundary to the hydrogen-induced IG fracture. The results are discussed in terms of the role of microstructural features and the observed activated mechanisms of HE.

Chapter 4 is an extension of the first part of objective 2. In this chapter, the effect of hydrogen on the tensile deformation behavior of the oligocrystal specimens is investigated at variable strain rates. This work aims to provide a deep comprehension of the exact contribution of deformation in hydrogen-induced IG fracture. The results obtained from this work are discussed in terms of the significance of hydrogen diffusion during deformation, hydrogen transport by mobile dislocations, and the activated HE mechanisms governing IG fracture.

Chapter 5 is focused on the second part of objective 2. Based upon the observations from experimental work in Chapter 3 and Chapter 4, in this work, a crystal plasticity-phase field fracture model (CP-PFM) based finite element framework is developed to simulate the macroscopic tensile response and corresponding microscopic fracture evolution behavior for hydrogen-free and hydrogen-charged oligocrystals. This coupled modeling framework is implemented in commercial finite element solver Abaqus using the two-layer scheme. Layer one solves for the dislocation density-based crystal plasticity model in the UMAT subroutine, whereas the phase field degree of freedom is solved in the UEL (User defined Element) subroutine. The developed model accurately simulated the macroscopic tensile response and corresponding microscopic ductile transgranular as well as brittle H-induced IG fracture for investigated oligocrystals. The findings from this study are employed to corroborate the observations made in the preceding chapters.

Chapter 6 is focused on objective 3, dedicated to investigating the integration of HE and HIC phenomenon toward the degradation of the structural integrity of pipeline X65 grade steel. During electrochemical hydrogen charging, this material exhibited the formation of blisters and cracks (HIC) near the sample surface. First, the role of microstructural constituents in the formation of these cracks and blisters during the hydrogen charging process is discussed. Subsequently, to confirm the impact of these hydrogen charging-induced blisters and cracks on mechanical deformation behavior, tensile and in-situ short fatigue crack growth analyses are conducted. The results obtained from this applied research highlight the significant role of hydrogen-induced blisters (developed during the hydrogen charging process prior to mechanical loading) in expediting the loss of structural integrity during the external mechanical loading of hydrogen-charged samples.

Chapter 7 summarized the findings in this thesis and discussed the future scope of the work.

Chapter 2

Coupled Crystal Plasticity - Hydrogen Transport Model for HELP Mechanism

2.1 Introduction

Hydrogen-induced premature failure in structural metallic materials is a foremost concern toward the sustainable hydrogen economy. With no common consensus on the dominance of the underlying mechanism, over the past years, multiple mechanisms are projected as viable explanations of hydrogen embrittlement (HE) [5, 10, 31, 32]. Hydrogen Enhanced Decohesion (HEDE) and Hydrogen Enhanced Localized Plasticity (HELP) are the two most prevalent mechanisms [33]. As per HEDE, high hydrogen concentration can promote the quasi-brittle cleavage type failure by reducing the cohesive strength at grain/phase boundaries, crack tip, and interfaces [34]. HELP can be summarized as an effect of dislocation-solute interaction to expedite localized plasticity by promoting dislocation activities [13, 35]. The multifaceted problem of HE cannot be expounded with one single mechanism, hence it is usually considered as a synergistic effect of more than one mechanism [7]. Experimental investigations [15, 25] confirmed the HE by hydrogen-enhanced plasticity-mediated decohesion (HELP-mediated HEDE). According to the HELP-mediated HEDE mechanism, the accelerated dislocation activities induced by hydrogen (via HELP mechanism) can increase local hydrogen concentration and stress levels at fracture sites to promote decohesion (via HEDE) [7, 15, 25]. Depending upon localized microstructure, solute concentration, and loading conditions, microscopic softening instigated by hydrogen-defect interaction can result in macroscopic hardening and/or softening [13]. To comprehend the complex HE phenomenon, and to understand the exact HE mechanism, it is advisable to interpret the macroscopic deformation behavior in the light of the microscopic bits of evidence i.e. defect concentration and distribution [25]. Based upon the evidence emanating from experiments [14, 36, 37], theoretical calculations [38, 39], and multi-scale simulations [40, 41, 42], hydrogen-dislocation interaction emerges as the most crucial factor to comprehend the HE response of materials [5].

Hydrogen affects the dislocation nucleation [43, 44], mobility [45, 46], and interaction [19, 36, 47] behavior significantly. Beachem [35] observed that hydrogen enhances ductility

(localized) by unlocking the dislocation (instead of locking) and allows dislocations to multiply and move at lower stress levels. Sirois and Birnbaum [45] reported a decrease in the activation-free enthalpy and the activation-free energy of dislocation slip for hydrogenated samples. The reduction in activation-free enthalpy and the activation-free energy indicates a lesser energy requirement for the movement of dislocations under a hydrogen atmosphere [37, 48]. Nanoindentation studies have reported a decrease in "pop-in" load in the presence of hydrogen and this can be interpreted as a decrease in the load to produce dislocations homogeneously [43, 44]. In-situ transmission electronic microscopy (TEM) investigations conducted under hydrogen atmosphere on a variety of materials ensured an increase in dislocation mobility, decrease in spacing between dislocations, and decrease in cross-slip probability [36]. Birnbaum and Sofronis [13] originated the concept of "hydrogen elastic shielding" which accounts for the HELP mechanism partially. According to this, hydrogen shields the interaction of dislocations with elastic stress centers, consequently yields in reduced spacing in pile-ups while enhancing the mobility of dislocations. Based upon the shielding effect mechanism, Chateau et al. [49] introduced a 'screening index' to capture the relative reduction in pair interactions in the presence of bulk hydrogen. Delafosse [39] incorporated this screening index in classical expressions of the line energy and line tension to discuss the effect of hydrogen on increased dislocation nucleation, weakening of dislocation junctions, and decrease in cross-slip probability. Recently, Gu and El-Awady [40] developed a 3D discrete dislocation dynamics framework and simulated the hydrogen elastic shielding effect similar to the one observed in experimentation but only at high hydrogen concentration. Sills and Cai [50] introduced the significance of interactions between hydrogen atoms on the dislocation core region as solute-solute interactions alter the dislocation core energy. [41, 42] performed the discrete dislocation plasticity (DDP) simulations by considering both hydrogen elastic shielding [40] and the effect of hydrogen on the dislocation core energy [50]. Hydrogen was observed to decrease the core energy of dislocations, which reduced the dislocation core force. Authors referred to this as "hydrogen core force shielding". Similar to the "hydrogen elastic shielding", "hydrogen core force shielding" resulted in enhanced dislocation generation, reduction in flow stress of dislocations, and reduced spacing in pile-ups but at much lower hydrogen concentration realistic for FCC and BCC metals [41, 42]. The authors observed clear supremacy of hydrogen core force shielding, whereas the contribution of hydrogen elastic shielding was negligible at realistic (low) hydrogen concentrations. Informed by atomistic data, these DDP simulations [40, 41, 42] complement the experimental evidence of increased dislocation density along with a decrease in dislocation pile-ups spacing [36, 51, 52]. These small-scale simulations on discrete dislocation level along with experimental knowledge are highly informative. However, the length scale associated with DDP simulations puts a limit on their use to model the synergistic role of various microstructural and external factors affecting hydrogen distribution, segregation, and associated HE mechanisms at a larger scale [22, 39]. The length scale associated with the finite element-based crystal plasticity

(CP) makes it the most promising choice for simulating the interconnection of small-scale phenomena with their macroscopic consequences. Castelluccio et al. [19] made an initial attempt to model the hydrogen effect on the macroscopic response of Nickel (Ni) single crystal by just varying the materials parameters informed by multi-scale simulations. However, their argument of hydrogen-induced hardening in FCC metals by an increase in activation energy contradicted the experimental observations. Various other researchers [20, 21, 53, 54, 55, 56] used coupled crystal plasticity and hydrogen diffusion/trapping model to study the role of hydrostatic stress, yield strength, hydrogen content and plastic deformation on the distribution of hydrogen in polycrystalline materials. Recently, Kumar and Mahajan [18] developed a dislocation density-based (one-way) coupled crystal plasticity-hydrogen diffusion/trapping model to simulate the effect of loading conditions on hydrogen distribution in the microstructure. However, during the event of hydrogen embrittlement, while the evolution of hydrostatic stress and plastic deformation affects the hydrogen distribution behavior; hydrogen concentration also affects the deformation behavior. Consequently, there is a requirement for a coupled diffusion-mechanics framework capable of simulating the real-time hydrogen distribution and its effect on defect evolution behavior controlling the overall deformation behavior in single crystal and polycrystalline configurations. Summarizing the recent experimental observations conducted to study the hydrogen effect (H-effect) on single crystal with single-slip orientation, single crystal with multiple-slip orientation and polycrystals, following points can be concluded: (a) hydrogen effect depends upon initial crystal orientation (hydrogen resulting stage-II hardening in single-slip orientation [39, 51] can result softening in the multiple-slip orientation [57]) (b) there is direct correlation between the hydrogen effect on fundamental properties of dislocations and the macroscopic behavior [51, 52, 57], (c) configurations subjected to high degree of multiple-slip i.e. polycrystals and single crystals oriented for multiple-slip exhibits similar H-effect on dislocation structure [52, 57], (d) for same nominal strain level, hydrogen develops an advanced state of deformation favourable for instigating localized failure [51, 52], (e) all the above discussed points can be very well explained by the hydrogen-dislocation interaction under the proposition of HELP mechanism, and lastly, (f) absence of modeling framework capable to predict these experimental observations (a-e) accurately.

Under the impression of the above discussion, and motivated by the need, this chapter presents a predictive coupled diffusion-mechanics framework to simulate the H-effect ranging from single crystal to polycrystalline configurations. Dedicated to simulating the hydrogen-assisted deformation and failure behavior emanating from the hydrogen-dislocation interaction under the proposition of HELP mechanism, the presented computational framework comprises a dislocation density-based crystal plasticity model coupled with a hydrogen diffusion/trapping model to simulate the two-way effect [58, 59, 60]. In the two-way effect, while hydrostatic stresses and dislocation density is affecting the hydrogen redistribution; hydrogen trapped at the dislocations is affecting the associated critical stresses, interaction strength of dislocations, and multiplication/annihilation

behavior of dislocations. As advisable [22], the framework is calibrated with the micromechanical tests performed on the same materials with and without hydrogen.

The theoretical foundation of the developed two-way diffusion-mechanics framework is detailed in Section 2.2. Section 2.3 describes the simulation results obtained for the single-crystal and polycrystalline configurations. Obtained results are discussed in Section 2.4 comparing the macroscopic flow behavior with the microscopic dislocation structures evolution observed experimentally for with and without hydrogen. Results show that the proposed framework is capable of predicting the hydrogen-induced modified dislocation structures similar to the one observed in experiments. Hydrogen-induced premature failure emerging from accelerated dislocation activities due to the hydrogen-induced shielding substantiates the failure caused by the HELP mechanism of hydrogen embrittlement. Section 2.5 presents the various conclusions drawn from the present work followed by the reference section.

2.2 Theory

2.2.1 Hydrogen diffusion/ trapping model

Hydrogen dissolved in metals is considered to reside at two sites i.e., normal interstitial lattice sites giving hydrogen concentration as C_L and trap sites giving the trapped part of hydrogen concentration as C_T. Considering dislocations as the only kind of trapping site in the present work, the total hydrogen trapped by dislocations lying at α slip system is written as C_T^α. Hence, $C_T = \sum_{\alpha=1}^{N_s} C_T^\alpha$ is the total hydrogen concentration trapped by dislocations along all the slip systems at a material point. N_s is the total number of slip systems (here for FCC N_s=12). Accordingly, the total hydrogen concentration at a material point is:

$$C_{Tot} = C_L + \sum_{\alpha=1}^{N_s} C_T^\alpha \tag{2.1}$$

Considering, only C_L as responsible for diffusion, the chemical potential of lattice hydrogen μ_L under the influence of hydrostatic stress (σ_H) is [61]:

$$\mu_L = \mu_L^0 + RTln\frac{C_L}{N_L} - V_H\sigma_H \tag{2.2}$$

where μ_L^0 is the reference lattice chemical potential, R is the universal gas constant, T is the absolute temperature, N_L is the number of lattice sites and V_H is the partial molar volume of hydrogen in metals. Considering the evolution of total hydrogen concentration in an enclosed volume dV of a metallic microstructure equal to the net hydrogen flux, $\boldsymbol{J}$, at the surface with unit normal vector $\boldsymbol{n}$, and surface area dS, the mass conservation equation takes the form as,

10

$$\frac{\partial}{\partial t}\int_{V}(C_L + \sum_{\alpha=1}^{N_s} C_T^{\alpha})dV + \int_{S} \boldsymbol{J}.\boldsymbol{n}dS = 0 \tag{2.3}$$

The hydrogen flux through the surface can be expressed as,

$$\boldsymbol{J} = -\frac{D_L C_L}{RT}\boldsymbol{\nabla}\mu_L \tag{2.4}$$

where D_L is the diffusion coefficient for hydrogen. On substituting the expression of chemical potential eqn. (2.2) in eqn. (2.4), we get

$$\boldsymbol{J} = -D_L\boldsymbol{\nabla}C_L + \frac{D_L C_L V_H}{RT}\boldsymbol{\nabla}\sigma_H \tag{2.5}$$

By using the eqn. (2.5) in eqn. (2.3),

$$\frac{\partial}{\partial t}\int_{V}(C_L + \sum_{\alpha=1}^{N_s} C_T^{\alpha})dV + \int_{S}(-D_L\boldsymbol{\nabla}C_L + \frac{D_L C_L V_H}{RT}\boldsymbol{\nabla}\sigma_H).\boldsymbol{n}dS = 0 \tag{2.6}$$

Using the divergence theorem, the above equation can be rewritten as,

$$\frac{\partial C_L}{\partial t} + \sum_{\alpha=1}^{N_s}\frac{\partial C_T^{\alpha}}{\partial t} - \boldsymbol{\nabla}.(D_L\boldsymbol{\nabla}C_L) + \boldsymbol{\nabla}.(\frac{D_L C_L V_H}{RT}\boldsymbol{\nabla}\sigma_H) = 0 \tag{2.7}$$

Considering the occupancy of hydrogen atoms in lattice sites as θ_L, and the occupancy of hydrogen in dislocations at α slip system as θ_T^{α}, the hydrogen concentrations in lattice and trap sites can be written as:

$$C_L = \theta_L N_L \qquad \& \qquad C_T^{\alpha} = \theta_T^{\alpha}N_T^{\alpha} \tag{2.8}$$

where, N_T^{α} is the trap density along α slip system. For FCC materials N_T^{α} is expressed in terms of the total dislocation densityρ^{α}, as [62],

$$N_T^{\alpha} = \frac{\sqrt{3}}{a}\rho^{\alpha}\frac{1}{N_A} \tag{2.9}$$

where, a is the lattice parameter, N_A is the Avogadro number. The equilibrium between the occupancy of the hydrogen atoms in lattice and trap sites is given by Oriani [63]. Here, it is assumed that the distribution of hydrogen between the lattice sites and dislocation cores lying along a particular slip system could be achieved by using the Oriani equilibrium [63] as,

$$\frac{\theta_T^{\alpha}}{(1-\theta_T^{\alpha})} = \frac{\theta_L}{(1-\theta_L)}\exp\left(-W_b/RT\right) \tag{2.10}$$

where W_b is the trapped binding energy assumed to be independent of the slip system. Using the eqn. (2.10), the concentration of hydrogen trapped at dislocations along α slip

system can be obtained as,

$$C_T^\alpha = \frac{\theta_L N_T^\alpha K_T}{(1 - \theta_L) + K_T \theta_L} \tag{2.11}$$

where, a constant $K_T = \exp\left(-W_b/RT\right)$ is used. Following Krom et al. [64] and Kumar and Mahajan [18] the partial derivative of the trap hydrogen concentration with respect to time is defined as,

$$\frac{\partial C_T^\alpha}{\partial t} = \frac{\partial C_T^\alpha}{\partial C_L}\frac{\partial C_L}{\partial t} + \theta_T^\alpha \dot{N}_T^\alpha \tag{2.12}$$

where, $N_T^\alpha = N_T^\alpha(\rho^\alpha(|\gamma^\alpha|))$. The rate of change of N_T^α with plastic flow i.e. with the evolution of dislocation density is given as:

$$\dot{N}_T^\alpha = \frac{\partial N_T^\alpha}{\partial \rho^\alpha}\frac{\partial \rho^\alpha}{\partial \gamma^\alpha}|\dot{\gamma}^\alpha| \tag{2.13}$$

Using eqn. (2.13) in eqn. (2.12),

$$\frac{\partial C_T^\alpha}{\partial t} = \frac{\partial C_T^\alpha}{\partial C_L}\frac{\partial C_L}{\partial t} + \theta_T^\alpha \frac{\partial N_T^\alpha}{\partial \rho^\alpha}\frac{\partial \rho^\alpha}{\partial \gamma^\alpha}|\dot{\gamma}^\alpha| \tag{2.14}$$

Following eqn. (2.11) we have,

$$\frac{\partial C_T^\alpha}{\partial C_L} = \frac{K_T N_L N_T^\alpha}{(N_L + (K_T - 1)C_L)^2} \tag{2.15}$$

Using the aforementioned equations in the mass conservation eqn. (2.7), a slip rate-based hydrogen diffusion/trapping model (an adaptation from [64]) can be written as,

$$\left(1 + \sum_{\alpha=1}^{N_s}\frac{\partial C_T^\alpha}{\partial C_L}\right)\frac{\partial C_L}{\partial t} - \boldsymbol{\nabla}.(D_L\boldsymbol{\nabla}C_L) + \boldsymbol{\nabla}.\left(\frac{D_L C_L V_H}{RT}\boldsymbol{\nabla}\sigma_H\right)$$
$$+ \sum_{\alpha=1}^{N_s}\left(\theta_T^\alpha \frac{\partial N_T^\alpha}{\partial \rho^\alpha}\frac{\partial \rho^\alpha}{\partial \gamma^\alpha}|\dot{\gamma}^\alpha|\right) = 0 \tag{2.16}$$

As perceptible, in the above hydrogen diffusion/trapping model, the calculation of the hydrogen distribution is coupled with the hydrostatic stress and plastic deformation. This model accounts for the continuous evolution of both interstitial lattice sites and trapping site occupancies with plastic deformation and hydrogen diffusion at any given location. The last term in the hydrogen diffusion/trapping model, eqn. (2.16), is the slip-rate factor (SRF) balancing the total hydrogen concentration C_{Tot} at a given location by facilitating a corresponding reduction in C_L and subsequent rise of C_T due to the increase in trap density during plastic deformation [18]. Note that the dislocations are considered as trapping sites only, H-transport by the dislocations needs additional considerations [62] which are not considered in this work.

2.2.2   Crystal plasticity model

Kinematics

Following the multiplicative decomposition [65], the total deformation gradient, $\mathbf{F}$ reads as,

$$\mathbf{F} = \mathbf{F}_e \mathbf{F}_p \tag{2.17}$$

where $\mathbf{F}_p$ is the lattice-preserving inelastic deformation gradient that maps to the plastic configuration and $\mathbf{F}_e$ is an elastic deformation gradient that maps from the inelastic to the deformed configuration. The velocity gradient, $\mathbf{L}$ can be written as,

$$\mathbf{L} = \mathbf{L}_e + \mathbf{F}_e \mathbf{L}_p \mathbf{F}_e^{-1} \tag{2.18}$$

where, $\mathbf{L}_e = \dot{\mathbf{F}}_e \mathbf{F}_e^{-1}$ is the elastic distortion-rate tensor and $\mathbf{L}_p = \dot{\mathbf{F}}_p \mathbf{F}_p^{-1}$ is plastic distortion-rate tensor. In the used crystal plasticity framework, the plastic velocity gradient $\mathbf{L}_p$ is composed of slip rates $\dot{\gamma}^\alpha$ on each slip systems as,

$$\mathbf{L}_p = \dot{\mathbf{F}}_p \mathbf{F}_p^{-1} = \sum_{\alpha=1}^{N} \dot{\gamma}^\alpha \, \boldsymbol{s}^\alpha \otimes \boldsymbol{m}^\alpha \tag{2.19}$$

where, $\boldsymbol{s}^\alpha$ and $\boldsymbol{m}^\alpha$ are the orthonormal vectors in the direction of slip and normal to slip plane respectively, for α slip system. $'\otimes'$, symbolizes the tensorial product. Second Piola Kirchhoff stress, $\mathbf{S}$ in the intermediate configuration is given as,

$$\mathbf{S} = \mathcal{C}^e : \frac{\mathbf{F}_e^T \mathbf{F}_e - \mathbf{I}}{2} \tag{2.20}$$

where, $\mathcal{C}^e$ is fourth order anisotropic elastic stiffness tensor and $\mathbf{I}$ is an identity tensor. The resolved shear stress along α slip system is determined as,

$$\tau^\alpha = \mathbf{S} : \boldsymbol{s}^\alpha \otimes \boldsymbol{m}^\alpha \tag{2.21}$$

The Cauchy stress, $\boldsymbol{\sigma}$ in the current configuration is obtained using push forward approach as,

$$\boldsymbol{\sigma} = det(\mathbf{F}_e)^{-1} \mathbf{F}_e \mathbf{S} \mathbf{F}_e^{T} \tag{2.22}$$

Flow rule and hardening law for dislocation density-based CP model

The slip-rate $\dot{\gamma}^\alpha$ along α slip system is determined as [66],

$$\dot{\gamma}^\alpha = \rho^\alpha b v_0 \left| \frac{\tau^\alpha - \zeta_b^\alpha}{\tau_c^\alpha} \right|^n sign(\tau^\alpha - \zeta_b^\alpha) \tag{2.23}$$

where, n is strain-rate sensitivity, b is the Burgers vector length and v_0 is reference velocity. ρ^α, τ^α and τ_c^α are the dislocation density, resolved shear stress, and critical resolved shear stress respectively, along α slip system [67]. ζ_b^α is the back stress on α slip

system introduced to account for the kinematic hardening. The evolution of the resolved backstress follows the nonlinear Frederik-Armstrong type hardening as,

$$\dot{\zeta}_b^\alpha = c_1\dot{\gamma}^\alpha - c_2|\dot{\gamma}^\alpha|\zeta_b{}^\alpha \tag{2.24}$$

where, c_1 and c_2 are material dependent parameters. Also, the accumulated slip on α slip system is defined as $\gamma_{acc}^\alpha = \int_0^t |\dot{\gamma}^\alpha|dt$. Following Mecking and Kocks [68], the dislocation density on slip system α is considered to emerge from the balance between the dislocation multiplication and annihilation along that slip system, as:

$$\dot{\rho}^\alpha = (k_{multi}\sqrt{\rho^\alpha} - k_{annih}\rho^\alpha)|\dot{\gamma}^\alpha| \tag{2.25}$$

where, k_{multi} and k_{annih} are the constants related to dislocation multiplication and annihilation, respectively. During deformation, hardening is controlled by the evolution of dislocation density and strength of interaction among dislocations on various slip systems. Following the generalized Taylor equation [69], critical resolved shear stress is defined as [70],

$$\tau_c^\alpha = \tau_f^\alpha + c_3\mu b\sqrt{\sum_{\beta=1}^{N_s} \chi_{\alpha\beta}\rho^\beta} \tag{2.26}$$

where τ_f^α is the strain-independent initial slip resistance on slip system α due to frictional resistance and solute atoms, here assumed to be same on all the slip systems. c_3 is a fitting constant. $\chi_{\alpha\beta}$ is the Taylor co-efficient matrix representing the strength of interactions between various slip systems [69]. In FCC crystals with 12 slip systems, the $\chi_{\alpha\beta}$ contains 12^2 coefficients that can be reduced to six independent constants using symmetries. These coefficients are associated with six types of interactions in dislocation on various slip systems (see Appendix-I). Dislocations gliding on parallel slip systems involve the self-interaction (a_0) and coplanar (a_1) interaction coefficients. The remaining four coefficients account for the interactions between non-coplanar slip systems such as Hirth locks (a_2), collinear interactions (a_3), glissile junctions (a_4), and Lomer–Cottrell locks (a_5). Collinear interactions are considered to generate a strong hardening effect due to the partial annihilation of gliding collinear dislocations segments resulting in the generation of highly curved dislocations that require a higher stress to recover a flowing state [71].

2.2.3 Two-way coupling

During the event of hydrogen embrittlement, while the stress state affects the hydrogen redistribution, hydrogen concentration also affects the stress-strain response of materials by altering local deformation behavior. In the proposed crystal plasticity model, dislocation activities govern the overall material deformation response. Solute hydrogen segregated at the core of dislocation alters the dislocation interactions behavior and hence the evolved stress-strain response [41, 50]. The occupancy of hydrogen trapped at

dislocations $\left(\theta_T^\alpha = \frac{C_T^\alpha}{N_T^\alpha}\right)$ is assumed as a key quantity to capture the effect of hydrogen on dislocation activities. $\theta_T^\alpha = 1$ narrates that all the trap sites at dislocations along the α slip system are fully occupied and give an upper bound for the effect of hydrogen on dislocation activities. θ_T^α, derives its value from lattice occupancy (hence from C_L) and trap binding energy of dislocations (W_b). In FCC, commonly reported trap binding energy (W_b) of dislocation is -10 kJ/mol, whereas in BCC it is -50 kJ/mol [62]. Traps with $W_b = -50$ kJ/mol will saturate at lower C_L values whereas traps with $W_b = -10$ kJ/mol saturate at relatively very high C_L. Selection of θ_T^α as coupling factor can relate the HE at relatively low hydrogen concentration in BCC comparison to FCC materials. Hydrogen-induced shielding (elastic shielding [13] and/or core force shielding [41, 42] accounting for the HELP mechanism) reduces the critical activation stress of Frank-Read sources and accelerate the expansion of dislocation loops [40, 41, 42]. This constitutes an increase in the dislocation multiplication rate. Also, the hydrogenated materials exhibit slip planarity due to the reduced probability of cross-slip, which inhibits the onset of dynamic recovery [37, 39]. Parameters k_{multi} and k_{annih} in dislocation density evolution law (eqn. (5.11)) denotes the dislocation multiplication and annihilation kinetics, consequently to capture the hydrogen effect on dislocation generation and annihilation rate these parameters are assumed to depend upon θ_T^α. Accordingly, the dislocation evolution law used in the current CP model (eqn. (5.11)) is modified to capture the role of hydrogen on dislocation evolution rate as:

$$\dot{\rho}^\alpha = (k_{multi}^H \sqrt{\rho^\alpha} - k_{annih}^H \rho^\alpha)|\dot{\gamma}^\alpha| \tag{2.27}$$

with

$$k_{multi}^H = (1 + l_c \theta_T^\alpha)k_{multi} \tag{2.28}$$

k_{multi}^H, capture the effect of hydrogen on dislocation storage rate per slip system. The high value of k_{multi}^H corresponds to an increase in dislocation multiplication rate. Accordingly, to capture the increased dislocation generation rate under the hydrogen atmosphere constant l_c is assumed to take a positive value. On the other hand, k_{annih}^H captures the effect of hydrogen on the annihilation rate as:

$$k_{annih}^H = (1 + k_c \theta_T^\alpha)k_{annih} \tag{2.29}$$

The small value of k_{annih}^H corresponds to a decrease in the annihilation rate. Accordingly, to capture the role of hydrogen toward the decrease in annihilation rate (due to a decrease in annihilation distance and stacking fault energy; hence decreases in cross-slip probability under hydrogen) constant k_c is assumed to take a negative value.

Apart from the increase in the dislocation density, the hydrogen-induced shielding effect toward the weakening of interaction strength of dislocations can be captured by decreasing the coefficients of interaction matrix ($\chi_{\alpha\beta}$) [22]. Castelluccio et al. [19] considered the weakening of the self-interaction coefficient only to explain hydrogen-induced closed spacing in dislocation pile-ups, whereas Yu et al. [47] reported the weakening of Lomer junction strength for FCC material under hydrogen atmosphere. Based upon the multiple

DDP-based observations, Tarleton [22] recommended considering the H-effect on the whole interaction matrix. To the best of the author's knowledge, it is still not clear whether hydrogen affects all types of dislocation interactions equally or in different magnitudes. To explore the possible H-induced failure scenarios (developed by HELP mechanism alone or in support with additional mechanisms) due to the mutual interactions of hydrogen-induced increase in dislocation density along with weakening of dislocation interactions behavior, here we have considered two different situations as:

Case 1- Hydrogen reduces the strength of all types of dislocation interactions equally [22]. To account for the equal effect of hydrogen-induced-weakening of all type dislocation interactions, $\chi_{\alpha\beta}$ in eqn. (2.26) is replaced with:

$$\chi_{\alpha\beta}^{H} = (1 + H_c \theta_T^{\alpha}) \chi_{\alpha\beta} \qquad (2.30)$$

where H_c is a constant with a negative value indicating the hydrogen-induced decrease in interaction strength.

Case 2- Hydrogen reduces the strength of the self-hardening coefficient only [19]. Accordingly, only coefficient a_0 in $\chi_{\alpha\beta}$ (in this case, rest of the components of $\chi_{\alpha\beta}$ will remain unaffected) is replaced with:

$$a_0^{H} = (1 + a_c \theta_T^{\alpha}) a_0 \qquad (2.31)$$

where a_c is a constant with a negative value indicating the hydrogen-induced decrease in interaction strength.

The role of hydrogen in yield strength is quite complicated. Structural materials may exhibit an increase or decrease in yield strength depending upon the propensity of dislocation pining due to solute drag effect, vacancy-hydrogen complex formation, and surface-damage/blister formation, which further depends upon crystal structure, material purity, test temperature, hydrogen concentration, and strain rate [72, 73, 74]. To restrict attention only to hydrogen-dislocation interaction accounting for the HELP mechanism, other phenomena such as solute drag and vacancy concentration effect are not considered in this work. However, the effect of hydrogen on yield strength is incorporated by changing, τ_f^{α} in eqn. (2.26) to $\tau_f^{\alpha H} = (1 + T_c \theta_T^{\alpha}) \tau_f^{\alpha}$. Here, constant T_c assumes sign and value as per the effect of hydrogen on yield strength. Note, a linear dependence of the affected parameters (whole interaction matrix or the self-interaction matrix element only, initial slip resistance, dislocation multiplication and annihilation) on hydrogen (by θ_T^{α}) is assumed as first approximation adapted from the recommendation based upon DDP [22] and crystal plasticity simulations [60, 75].

2.2.4 Numerical implementation

A summary of governing equations and boundary conditions for the coupled displacement-diffusion problem is provided in Appendix-II. The proposed modeling framework is implemented using UMAT (User defined Material) and UMATHT (User

defined Material for Heat Transfer) subroutines in the commercial finite element solver Abaqus. UMAT is used to solve the dislocation density-based crystal plasticity model, whereas UMATHT is used to solve the hydrogen diffusion/trapping equation (following the analogy between heat transfer and diffusion equation exploited in earlier work by [76]). To solve the hydrogen diffusion equation in UMATHT, the gradient of hydrostatic stress is calculated using the procedure as in [21]. The gradient of hydrostatic stress, slip-rates along slip systems, derivatives such as $\frac{\partial N_T^\alpha}{\partial \rho^\alpha}$ and $\frac{\partial \rho^\alpha}{\partial \gamma^\alpha}$ obtained from the previous converged time increment are then provided to UMATHT to solve the slip-rate-based hydrogen diffusion/trapping model and to provide hydrogen distribution in the current time increment. To implement a two-way coupling scheme for capturing the role of hydrogen on crystal plasticity parameters, θ_T^α from the previously converged time step is provided to the UMAT to solve the mechanical behavior at the current time increment.

The material model presented here is calibrated against the experimental stress-strain curves for Ni single crystal. The parameter identification has been performed using a least square method, using a python script based on the Abaqus 2020 library. This script is directly launched in the CAE console of Abaqus using the SciPy optimization tool [77] and the Nelder–Mead algorithm which has been shown to be the more efficient for other H-related inverse parameter identification [78]. The implemented optimization strategy performs crystal plasticity finite element simulation(s) and tries to minimize the chosen objective function (OF) by adjusting the parameter space over iterations. In the present work, the deviation between the simulated and experimental single-crystal stress–strain data served as the objective function for calibrating the constitutive crystal plasticity parameters. Figure 2.1a illustrates the general layout of the used optimization strategy (see [79] for more details). The optimization algorithm is used in two steps. In the first step, the crystal plasticity parameters are calibrated to replicate the tensile behavior of Ni single crystal without hydrogen. With these calibrated crystal plasticity parameters, in the second step hydrogen effect is captured by optimizing the l_c, k_c, H_c or a_c and T_c parameters.

Experimental tensile stress-strain curves of Ni single crystal with $\langle -167 \rangle$ orientation (favor initial single slip system activation) obtained for hydrogen charged and uncharged conditions (see, Fig. 2.1b and Fig. 2.2a) from the work of Yagodzinskyy et al. [1] are used as reference data for calibration purpose. The tensile curve for $\langle -167 \rangle$ orientation exhibits stage-I followed by stage-II hardening behavior. The addition of hydrogen results in an extension of stage-I with delayed onset of stage-II followed by an increase in stage-II hardening [1, 39, 51]. This complexity in tensile behavior (with and without hydrogen) makes this particular orientation a perfect candidate for a good calibration process. However, the hydrogen effect depends upon the crystal orientation, also the polycrystalline microstructure favors the high degree of multi-slip systems activation controlling the overall deformation behavior [52, 57]. Consequently, to validate the generality of the proposed framework, and to gain a thorough understanding of the hydrogen effect on single crystal to polycrystalline configurations, after validating on single crystal with single-slip

configuration, simulations for single crystal with multi-slip orientation and polycrystals were performed.
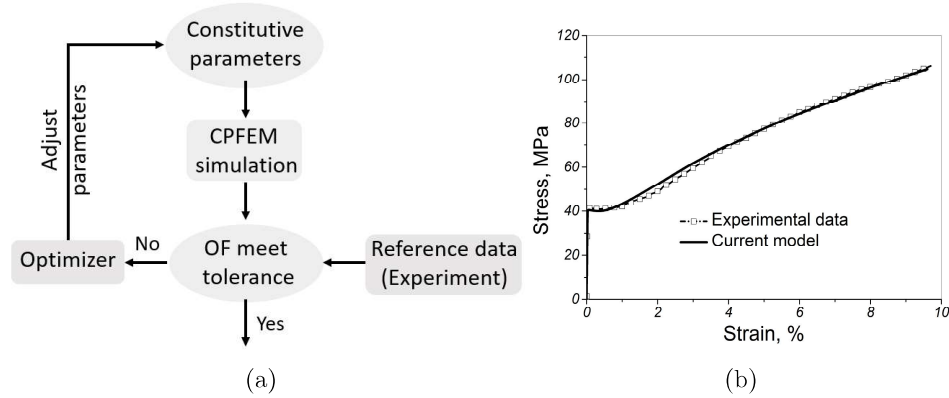
Figure 2.1: (a) Schematic of optimization algorithm and (b) stress-strain curve of Ni single crystal with $\langle -167 \rangle$ orientation without hydrogen. (Experimental data adapted from [1])

The single crystal simulations are performed on full dog bone shape tensile specimen (with dimensions of gauge section as $0.3 \times 3 \times 8$ mm^3) similar to the one used in the experimental work of Yagodzinskyy et al. [1]. For polycrystal simulation, an artificial microstructure of size $500 \times 500 \times 5$ μm^3 containing 30 randomly oriented columnar grains obtained from Neper software [80] is imported to Abaqus using python scripts [81]. For polycrystal, grain boundaries are considered as simply the boundary between two adjacent grains of different orientations (i.e. no special treatment in terms of diffusivity, binding energy, slip transmission, etc. is provided [18]). C3D8T-type elements are used for all types of simulations. All the simulations are performed under a uniform strain rate of 9.0×10^{-5} s^{-1}. For simulation under a hydrogen atmosphere, all the samples are assumed to be precharged with uniform initial lattice hydrogen concentration. Also, the specimen boundaries are assumed as insulated so that there is no flux of hydrogen away from the specimen.

2.3 Results

2.3.1 Tensile behavior of single crystal oriented for single-slip

Inverse identification strategy identified ρ_0, k_{multi}, and k_{annih} as adjustable parameters to match the simulated stress-strain curve of Ni single crystal oriented for easy glide region with experimental data. Figure 2.1b presents experimental and simulated uniaxial tensile curves obtained after optimization for Ni single crystal (without hydrogen) with tensile axis aligned with $\langle -167 \rangle$ orientation. A good agreement between the experimental and simulated stress-strain curves in terms of yield stress and hardening behavior shows a successful calibration of the CP model parameters. The proposed model replicates the typical stage I and stage II deformation behavior for $\langle -167 \rangle$ orientation [1]. Table 2.1 presents the values of constitutive as well as calibrated CP parameters. Table 2.2 presents

the value of parameters used in the hydrogen diffusion/trapping model. After optimizing the CP parameters for uncharged condition, inverse optimization was applied to identify l_c, k_c, H_c or a_c, and T_c parameters to replicate the hydrogen effect on the stress-strain curve. Two different sets of values for these constants obtained for Case 1 and Case 2 are shown in Table 2.3.

Table 2.1: The crystal plasticity related parameters used in model

Parameter	Symbol	Magnitude	Units	Reference
	C_{11}	246	GPa	
Elastic constant	C_{12}	147	GPa	[75]
	C_{44}	124	GPa	
Inverse strain-rate sensitivity	n	20	-	[18]
Burgers vector length	b	2.5×10^{-7}	mm	[18]
Slip systems	N_s	12	-	
Initial dislocation density	ρ_0	9.3×10^5	mm^{-2}	Calibrated
Reference dislocation velocity	v_0	5	mm·s^{-1}	[18]
Dislocation multiplication const.	k_{multi}	303503	mm^{-1}	Calibrated
Dislocation annihilation const.	k_{annih}	10	-	Calibrated
Initial slip resistance	τ_f^α	4	MPa	Assumed a priori
Scaling constant	c_3	1.0	-	Assumed a priori
Back stress parameter	c_1	200	-	Assumed a priori
Back stress parameter	c_2	100	-	Assumed a priori
	a_0	0.122	-	
	a_1	0.122	-	
Interaction coefficients	a_2	0.058	-	[82]
	a_3	0.658	-	
	a_4	0.137	-	
	a_5	0.122	-	

Table 2.2: Hydrogen diffusion/trapping model related parameters

Parameter	Symbol	Magnitude	Units	Reference
Number of lattice sites	N_L	9.14×10^{-4}	mol·mm^{-3}	[75]
Dislocation binding energy	W_b	-10	kJ.mol^{-1}	[83]
Initial lattice H concentration	C_{L0}	1.57×10^{-7}	mol· mm^{-3}	-
Hydrogen diffusivity	D_L	6.0×10^{-8}	$mm^2 \cdot s^{-1}$	[84]
Partial molar volume of H	V_H	2000	$mm^3 \cdot mol^{-1}$	[84]
Temperature	T	300	K	-
Lattice parameter	a	3.52×10^{-7}	mm	-
Gas constant	R	8314	N·mm· $mol^{-1} \cdot K^{-1}$	-

Table 2.3: Hydrogen fitting constants

Model type	l_c	k_c	H_c or a_c	T_c
Case 1	47.0	-89.0	-91.0 (H_c)	528.0
Case 2	15.0	-55.0	-75.0 (a_c)	185.0

Figure 2.2a presents the simulated tensile stress-strain curves obtained with calibrated parameters for hydrogen-charged and uncharged conditions. Under hydrogen-charged

conditions, Case 1 and Case 2 resulted in the same tensile curve as they are calibrated against the same experimental data. Hydrogen-induced increase in yield strength, delay in onset of stage II, and increase in stage II hardening are replicated. Consistent with the Schmid factor calculations, slip system B4 (refer to Appendix-I for used Schmid and Boas notation of slip systems) dominated as the primary slip system for hydrogen-charged and uncharged conditions. This was followed by the activation of A3 as the next dominant slip system during tensile deformation under all conditions. Contribution from the rest of the slip systems was relatively insignificant, hence, not discussed further.

(a)   (b)
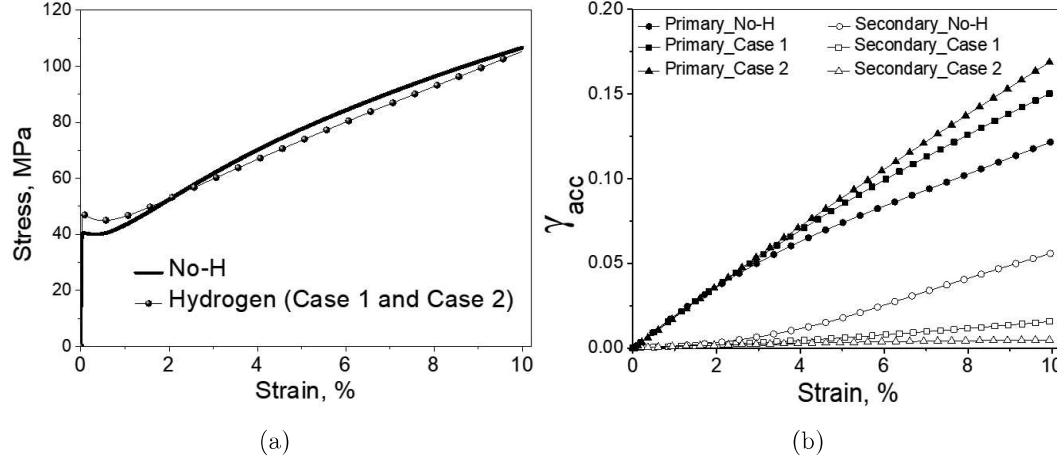
Figure 2.2: Simulated (a) stress-strain curves and (b) accumulated slip evolution on primary and secondary slip systems for single crystal with $\langle -167 \rangle$ orientation without and with hydrogen (Case 1 and Case 2)

In contrast to the uncharged condition, both cases under hydrogen charged condition resulted in an increased accumulated slip on the primary slip system (B4), while accumulated slip decreased on the secondary slip system (A3) (see Fig. 2.2b). More localized slip on the primary slip system in Case 2 than in Case 1 (as shown in Fig. 2.2b) is due to the difference in calibration parameters used for both cases under hydrogen conditions. Figure 2.3 presents the dislocation density for hydrogen-charged and uncharged conditions. Hydrogen charging increased the total dislocation density for both the cases considered here. However, hydrogen increased the dislocation density on the primary slip system while it decreased on the secondary slip system. Figure 2.3 signifies that enhanced total dislocation density under hydrogen arises from the increase in dislocation density on the primary slip system. Hydrogen-induced slip localization with an increase in dislocation density on a particular slip system is considered to emerge as closely spaced dislocations with planar structure. Under hydrogen-charged conditions, Case 1 experience a strong softening effect due to hydrogen-induced weakening of all type of dislocation interactions, whereas the softening effect is moderate in Case 2 as only self-hardening is compromised. Hence, to exhibit the same tensile flow curve in both cases, Case 1 exhibits higher dislocation density than Case 2 (see Fig. 2.3).

Figures 2.4(a-d) are showing the variation in lattice occupancy θ_L, trap occupancy $\theta_T =$
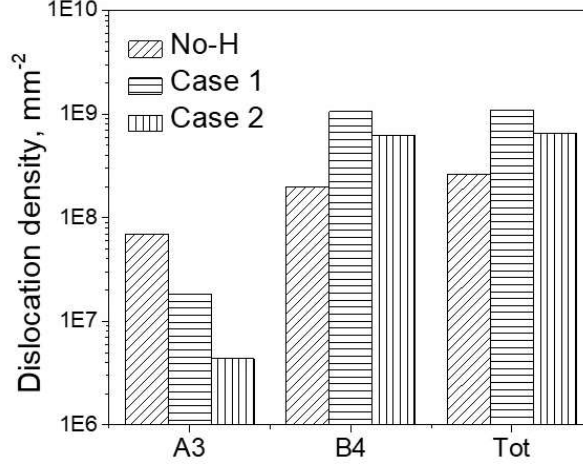
Figure 2.3: Dislocation density on primary slip system (B4), secondary slip system (A3), and total dislocation density at the end of deformation for single crystal with $\langle -167 \rangle$ orientation without and with hydrogen (Case 1 and Case 2)

$\sum \theta_T^\alpha / 12$, total trap concentration C_T and total dislocation density with strain for both the hydrogen charged cases. With increasing strain value, an increase in dislocation density and total trapped hydrogen concentration (C_T) can seen in Fig.2.4c and 2.4d, respectively. On the contrary, a decrease in lattice occupancy (θ_L) and trap occupancy (θ_T) with strain level can be seen in Fig. Fig.2.4a and 2.4b, respectively. As the lattice H-concentration is (i.e. $C_L = \theta_L N_L$, with N_L as constant) is governed by the θ_L only, a decrease in C_L can also be understood. Moreover, as per Oriani's equilibrium, the θ_T or θ_T^α drives its value from the θ_L (hence C_L), accordingly with decrease in θ_L, the trap occupancy θ_T is also decreasing. This further implies that with increase in C_T at a material point, the hydrogen availability per trap at that point will decrease. Accordingly, the effect of hydrogen on dislocation activities and critical resolved shear stress value (which derives its value as collective effect of hydrogen on dislocation multiplication, annihilation and interaction for case 1 and case 2) will decrease with the strain evolution. Moreover, a different values of θ_L, θ_T and C_T with strain for both the H-charged cases is due to the difference in dislocation density evolution. It is further to emphasize here that in the currently developed model, the lattice hydrogen concentration at material points is driven by the gradient of the hydrostatic stress. For the case of uniaxial tension test in single crystals the hydrostatic stress is nearly uniform throughout the gauge section (also reported earlier by [75]) i.e. there are no hydrostatic stress peaks at which there will be significant accumulation of lattice hydrogen. Hence, it is only the plasticity (N_T in C_T) which results in increase in C_T at the expense of θ_L (hence C_L) to balance the total hydrogen concentration. However, the decrease in θ_L over the course of deformation can be seen to be less than 1 %. This indicates that the initial hydrogen concentration (H inserted during the charging) has a more significant impact on the single crystal's behavior, while the effect hydrogen redistribution appears to be relatively insignificant. However, in polycrystals, there is always significant heterogeneity in hydrostatic stress as well as

plasticity levels which can affect the H-redistribution.
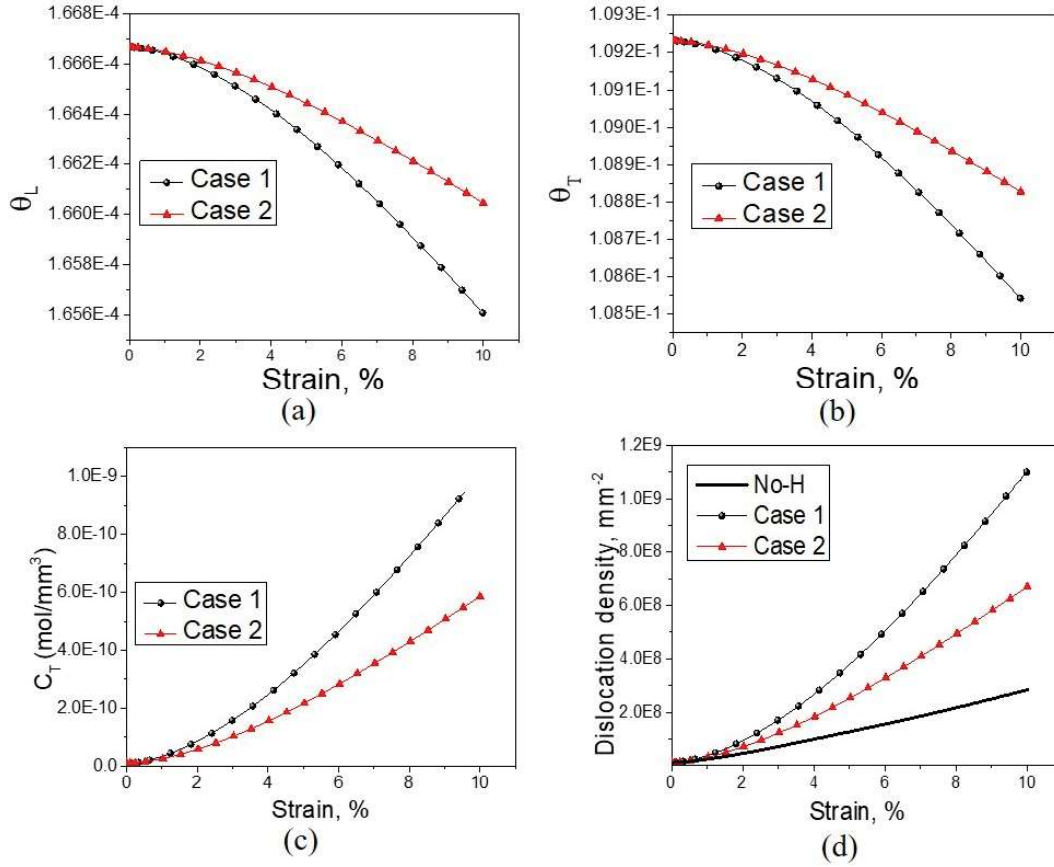
Figure 2.4: Evolution of (a) θ_L, (b) θ_T, (c) C_T, and (d) total dislocation density for single crystal oriented for single-slip

2.3.2 Tensile behavior of single crystal oriented for multi-slip

CP and hydrogen-related parameters calibrated for single-slip orientation are also applied to simulate the effect of hydrogen on a single crystal with multi-slip orientation $\langle 001 \rangle$. Figure 2.5a presents the tensile stress-strain curve without and with hydrogen for this orientation. The uncharged sample exhibited the absence of stage I and linear hardening in stage II (typical for multi-slip orientation) with overall tensile flow behavior in close approximation to experimental results [57, 85]. Hydrogen addition exhibited an increase in yield strength followed by two extreme conditions of macroscopic softening (for Case 1) and hardening (for Case 2) in reference to the uncharged conditions. Figure 2.5b presents the total dislocation density evolution in uncharged and hydrogen-charged samples for $\langle 001 \rangle$ orientation. As also observed for $\langle -167 \rangle$ orientation, in $\langle 001 \rangle$ orientation hydrogen charging increased the total dislocation density for both Case 1 and Case 2. Case 1, however, exhibited a high dislocation density in comparison to Case 2. Despite the high evolution rate of dislocation density, Case 1 exhibit low hardening rate than Case 2. In multi-slip orientation, all types of dislocation interactions in $\chi_{\alpha\beta}$ contribute to

the hardening rate significantly. In Case 1, hydrogen weakens all types of dislocation interactions; whereas in Case 2, only self-hardening is compromised due to hydrogen with no effect on the rest of the dislocation interactions type. Consequently, in Case 1 strong effect of hydrogen-induced-weakening of dislocation interactions is dominating the increased hardening rate due to an increase in dislocation density. On the contrary in Case 2, since only the self-hardening component is getting affected, a moderate softening effect is dominated by the hardening effect of hydrogen-induced increase in dislocation density. In view of these observations, a comparison of tensile curve behavior specific to Case 1 of single-slip and multi-slip orientation indicates that simulated same HE mechanism that yields hardening at single-slip dominated orientation can cause softening in another (multi-slip) orientation.

(a)   (b)
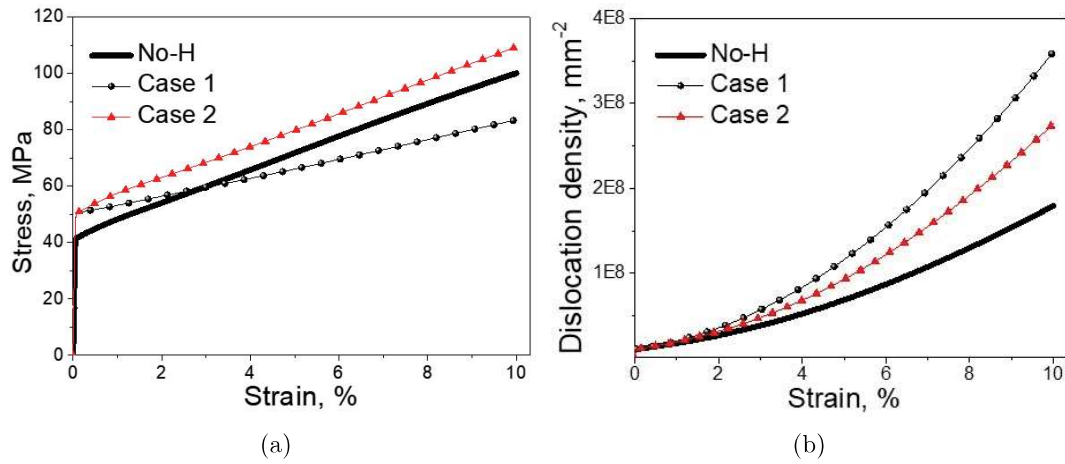
Figure 2.5: Simulated (a) stress-strain curve and (b) total dislocation density evolution of single crystal oriented for multi-slip without and with hydrogen (Case 1 and Case 2)

Specific to the investigated multi-slip orientation, a total of eight slip systems (A2, A3, B2, B4, C1, C3, D1, D4) with the same Schmid factor were activated. During the course of deformation, activated slip systems exhibited an insignificant difference in the evolution of accumulated slip for uncharged and both hydrogen-charged cases (see Appendix-III). Moreover, hydrogen (for both cases) increased the dislocation density on all the activated slip systems (see Appendix-III), unlike in the single-slip orientation where dislocation density increased on one of the slip systems (primary slip system) while decreased on the other (secondary) slip systems. An insignificant difference in the slip accumulation behavior on the activated slip systems for uncharged and hydrogen-charged cases corresponds to the experimental observation that hydrogen does not alter the formation process of dislocation structures for this multi-slip orientation [57]. Moreover, using the similitude concept [52], an increase in total dislocation density can be linked with relatively small cell size observed experimentally for multi-slip dominating configurations. Lawrence et al. [85] reported a hydrogen-induced increase in yield strength and hardening rate (as observed for Case 2). In contradiction to Lawrence et al. [85], with nearly similar hydrogen concentration Ghermaoui et al. [57] reported a hydrogen-induced increase in

yield strength followed by a decrease in hardening rate (as observed for Case 1). Moreover, [57] reported a hydrogen-induced decrease in dislocation cell size but with decreased dislocation density, which contradicts the increase in dislocation density simulated for Case 1. The disparity between the experimental results of Lawrence et al. [85] and Ghermaoui et al. [57] along with the observed disparity for simulated dislocation density for Case 1 with experimental observation put forward the need to investigate other factors such as the role of hydrogen on vacancy formation, interaction of dislocations with vacancy-hydrogen complexes which otherwise is not in the scope of present work.

2.3.3   Tensile behavior of polycrystal

In polycrystalline microstructure, grain level elastic and plastic anisotropy results in a variation of stress-strain distribution throughout the microstructure. During deformation, while the evolution of hydrostatic stress and plastic deformation affects the hydrogen distribution; hydrogen concentration is also affecting the deformation behavior. Unlike the case of single crystals with nearly homogeneous hydrostatic stress distributions, polycrystals exhibit significant variation in hydrostatic stress as well as in plastic deformation. To simulate the effect of hydrogen on multigrain systems, an artificial polycrystal with randomly oriented grains is generated (see Section 2.2.4 for detailed procedure). Figure 2.6a presents the initial microstructure containing 30 columnar grains with random crystallographic orientation (inverse pole figure (IPF) key in Fig. 2.6b). The simulation model for the polycrystal after meshing in Abaqus is shown in Fig. 2.6c. The polycrystal model is subjected to displacement-controlled uniaxial tension in the Y-direction. During the loading process, all the surfaces stay flat through the linear constraint method to approximately ensure periodicity.

(a)   (b)   (c)
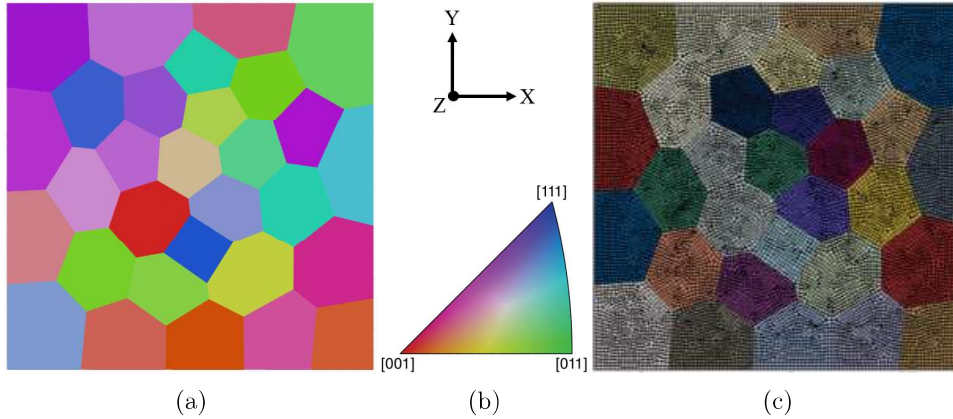
Figure 2.6: (a) Polycrystal with randomly oriented grains generated with Neper, (b) inverse pole figure (IPF) key for the grains in figure (a), and (c) finite element mesh obtained from Abaqus

Figure 2.7 presents the evolution of hydrostatic stress, lattice hydrogen concentration, trap hydrogen concentration, and total hydrogen concentration in microstructure at the end of deformation. Figure 2.7(a,d,g, and j) presents the results of one-way coupling

only i.e. deformation can alter the hydrogen distribution but hydrogen concentration has no effect on the stress-strain behavior. Figure 2.7(b,e,h,k) and 2.7(c,f,i,l) present the results of two-way coupling for Case 1 and Case 2, respectively. A significant effect of hydrostatic stress distribution on the evolution of lattice hydrogen concentration is evident from Fig. 2.7(a-f). Lattice hydrogen is diffusing from the low hydrostatic stress to the high hydrostatic stress region as also reported earlier [20, 21]. Initial hydrogen concentration, trap concentration (dislocation density), and the associated trap binding energy considered for the current material system resulted in trapped hydrogen concentration almost two orders lower than the lattice hydrogen concentration. Consequently, the distribution of total hydrogen concentration is dominated by the lattice hydrogen concentration (see Fig. 2.7 (j-l)) with the trivial effect of trap hydrogen concentration. This observation is similar to the already reported results by Ilin et al. [53] and Hussein et al. [20]. As a result of these observations specific to the current material system, hydrostatic stress gradient is concluded as a dominating factor to control hydrogen concentration distribution.

Different crystal orientations of the adjacent grains experience different hydrostatic stress across the grain boundaries. High heterogeneity in σ_H at the grain boundaries resulted in local high C_L (and hence C_{Tot}) near the grain boundaries and triple junctions. Relatively high hydrostatic stress gradient resulted in a comparatively high gradient in C_L throughout the polycrystal for Case 2 than the other two cases. Figure 2.8 presents the contour plots of total dislocation density for hydrogen-charged and uncharged conditions. Trapped hydrogen accumulated at the regions of high dislocation density (see Fig. 2.7(g-i) and Fig. 2.8). Hydrogen charging increased the dislocation density as well as fortified heterogeneity in the distribution for both Case 1 and Case 2. However, Case 1 resulted in relatively high dislocation density, subsequently higher values of C_T than the one-way model and Case 2 (see Fig.2.7 (g-i)).

Figure 2.9 (a and b) presents the stress-strain curves and corresponding total dislocation density evolution obtained for one-way, Case 1 and Case 2. In comparison to the one-way model, polycrystal exhibited hydrogen-induced macroscopic softening and hardening for Case 1 and Case 2, respectively. Each randomly oriented grain in polycrystal experiences a different number of active slip systems with a significant role of all types of dislocation interactions during deformation. In Case 1, hydrogen reduces the strength of all types of dislocation interactions resulting in a strong softening effect, whereas in Case 2 only self-hardening is reduced by hydrogen resulting in a moderate softening effect. Consequently, for Case 1 even if the dislocation density is high the softening effect is dominating and results in overall macroscopic softening after hydrogen charging. However, for Case 2, the moderate softening effect is dominated by the dislocation density induced hardening (even the dislocation density is lower than Case 1) and hence resulted in macroscopic hardening (see Fig. 2.9a for tensile curves). These results highlight the important role of hydrogen on macroscopically observed softening or hardening emerging from the trade-off between the hydrogen-induced microscopic softening (emerging from weak dislocation interactions and decreased stress to bow out the dislocation under the
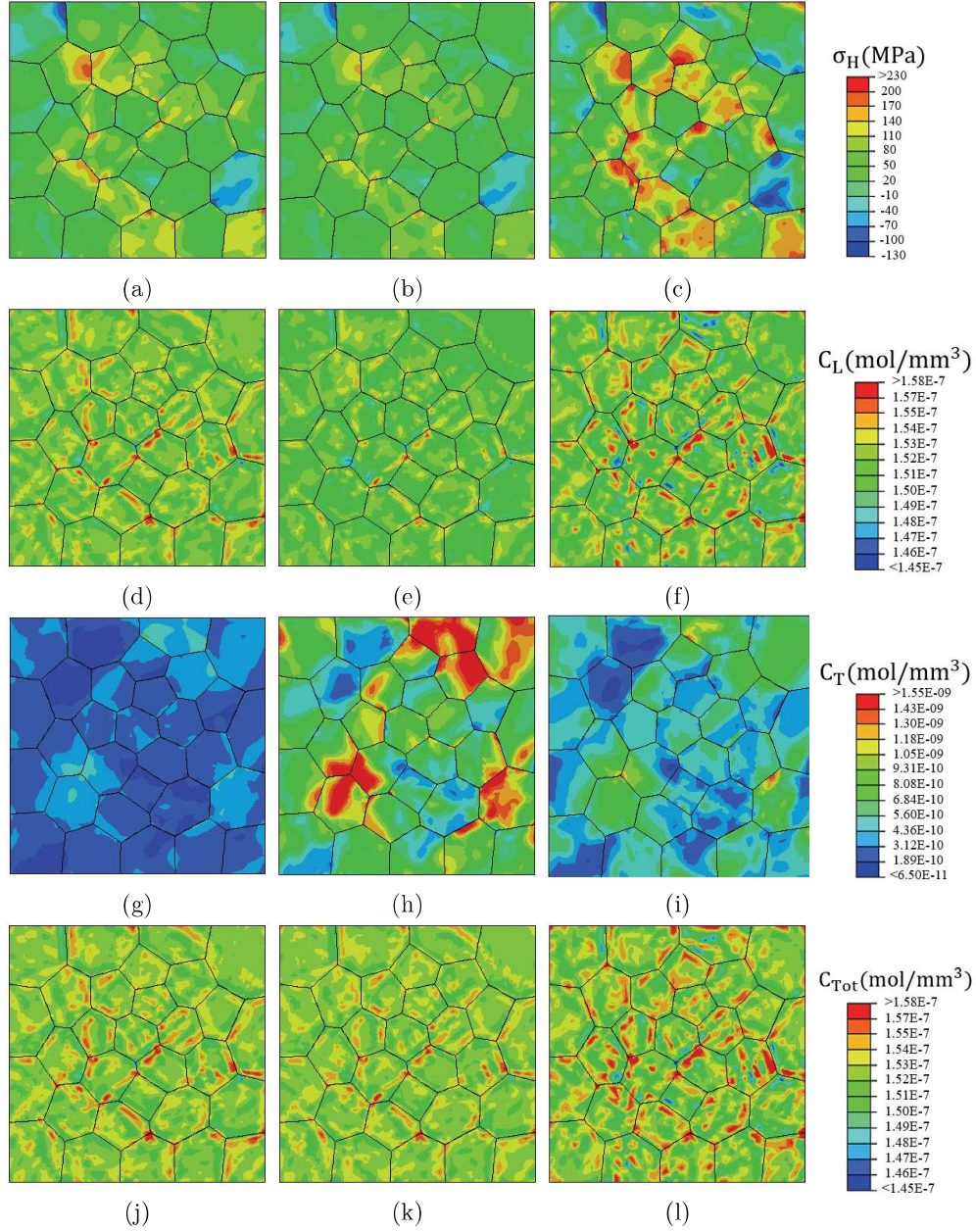
Figure 2.7: The evolution of (a-c) hydrostatic stress (σ_H) (d-f) lattice hydrogen (C_L) (g-i) trapped hydrogen (C_T) and (j-l) total hydrogen concentration (C_{Tot}) at the end of deformation. Figures (a,d,g,j) present the results obtained using the one-way coupling, (b,e,h,k) and (c,f,i,l) of the two-way coupling model for Case 1 and Case 2, respectively

(a)   (b)   (c)
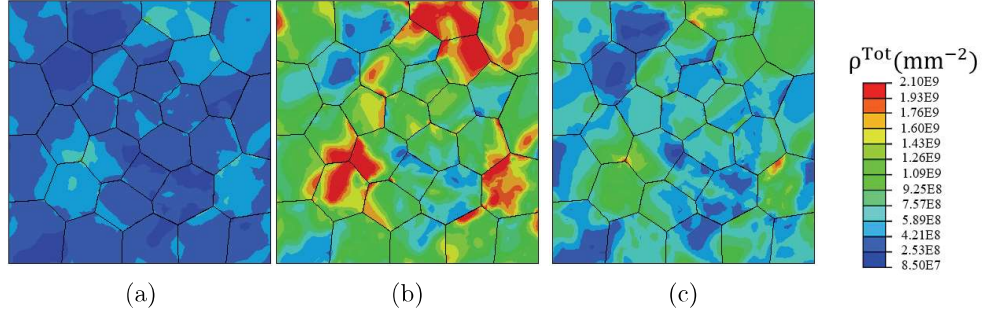
Figure 2.8: Evolution of total dislocation density at the end of deformation for the (a) one-way model, (b) Case 1, and (c) Case 2 of two-way coupling model

hydrogen atmosphere) and defect concentration-induced hardening effect.

(a)   (b)
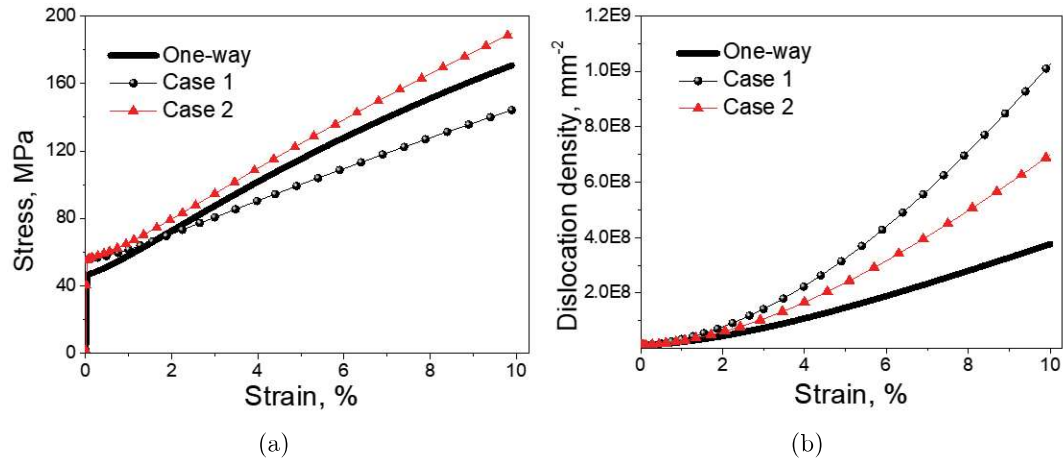
Figure 2.9: (a) Tensile stress-strain curve and (b) total dislocation density evolution for polycrystal under various conditions

Figure 2.10 presents the contour plots of von Mises stress distribution in polycrystal under different conditions. Case 2 developed concentrated stress spots in comparison to the one-way model and Case 1. These concentrated stress spots developed near/at the grain boundaries and triple junctions (see Fig. 2.10c) correspond to the location of hydrogen-induced high dislocation density (see Fig. 2.8c). Subject to the stress elevation beyond a critical value at these locations, a stress-controlled premature brittle intergranular failure can be triggered. Hence, Case 2 can be seen as one of the possible scenarios developed by the HELP mechanism to cause brittle inter-granular failure [41]. The absence of intense stress spots in Case 1 even with very high dislocation density as shown in Fig. 2.10b is attributed to the dominating role of hydrogen-induced weakening in dislocation interactions as discussed earlier.

2.4   Discussion

For uncharged conditions, FCC single crystals oriented for initially single-slip develop the dislocation pattern comprising geometric necessary boundaries (GNBs) and equiaxed
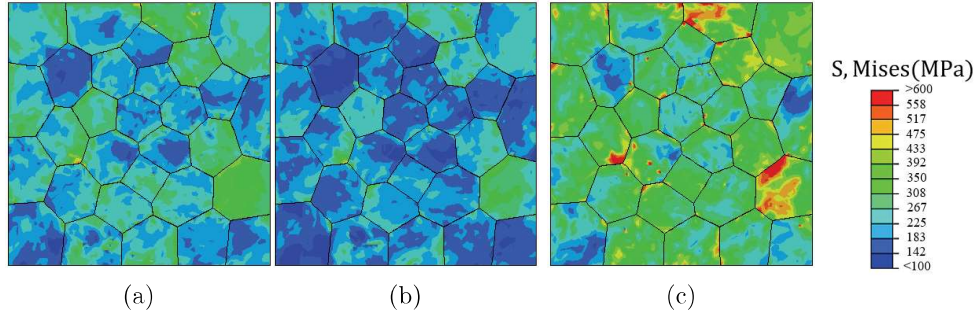
Figure 2.10: Evolution of von Mises stress at the end of deformation for (a) one-way model, (b) Case 1, and (c) Case 2 of two-way coupling model

dislocation cells between these walls [51]. However, the high degree of multiple-slip for single-crystal with tensile axis oriented for multi-slip and polycrystals develop dislocation pattern comprising mainly the well-defined equiaxed cells where the boundaries of these equiaxed cells are referred to as incidental dislocation boundaries (IDBs) [52, 57]. Recent TEM observations [51, 52, 57] conducted for the same nominal strain demonstrated the effect of hydrogen addition on the dislocation structure evolution. The presence of hydrogen promoted the planar GNBs with reduced spacing for single crystal oriented for single-slip [51]. However for polycrystals [52] and single crystal oriented for multiple-slip [57], hydrogen is observed to accelerate the evolution of dislocation structures without modifying the dislocation structures formation process (appears as comparatively refined dislocation cells with dense dislocation walls after hydrogen). The simulation results specific to single crystal oriented for initially single-slip predicted hydrogen-induced closely spaced planar dislocation structure. These closely spaced planar dislocation structures i.e. pile-ups formed during an early stage of deformation under hydrogen atmosphere are considered to evolve as planar GNBs with reduced spacing during large deformations [51]. Furthermore, these GNBs act as a screen to the dislocation motion and increase the hardening rate further as observed by Girardin et al. [51]. In contrast to single-slip orientation, simulation results for multi-slip orientation revealed insignificant differences in the slip accumulation behavior for uncharged and hydrogen-charged cases that can be associated with the experimental observation [57] that hydrogen does not alter the formation process of dislocation structures for this multi-slip orientation. These observations reveal the crystallographic orientation-dependent hydrogen effect on dislocation pattern evolution, which controls the hardening behavior. In polycrystals, Wang et al. [52] reported a smaller dislocation cell size with dense dislocation walls for Ni material deformed for high-pressure torsion under a hydrogen atmosphere. This observed dislocation structure was attributed to a hydrogen-induced decrease in dislocation spacing with increased dislocation density under a hydrogen atmosphere. An increase in total dislocation density observed for polycrystalline simulation under a hydrogen atmosphere can be associated with the experimentally observed hydrogen-induced decreased cell size with higher dislocation density in cell walls [52]. Moreover, the configurations

subjected to the high degree of multi-slip (i.e. polycrystal and multi-slip oriented single crystal) exhibited similar macroscopic softening and hardening for Case 1 and Case 2, respectively. By considering the direct correlation between the hydrogen effect on fundamental properties of dislocations and the macroscopic behavior, it can be concluded that the polycrystals and single crystals oriented for multiple-slip should exhibit similar H-effect on dislocation structure. Altogether, it can be concluded that the hydrogen develops an advanced state of deformation leading to deformation-induced boundaries (i.e. dislocation cell walls/IDBs and cell block walls/GNBs) with high dislocation density. High dislocation density facilitates the rapid void nucleation and growth along these deformation-induced boundaries at a lower stress level [86]. Martin et al. [87] correlated the sub-surface intense and highly localized deformation to the ridges like quasi-cleavage fracture surface arising from the growth and coalescence of voids. Accordingly, the hydrogen-induced increase in dislocation density simulated for both Case 1 and Case 2 can be viewed as a proposition of the hydrogen-induced rapid void formation along these deformation-induced boundaries within the framework of the hydrogen-enhanced localized plasticity (HELP) mechanism for hydrogen embrittlement [87, 5]. Moreover, recent DDP simulations [41] reported that the increased dislocation density piling up against the obstacles develops concentrated stress zones leading to premature failure around that obstacle. Case 2 (in Fig. 2.10c) replicates one such scenario of developed concentrated stress spots around grain boundaries and triple junctions with elevated stress values under a hydrogen atmosphere. These stress spots are formed due to high dislocation density at those locations (see Fig. 2.8c and Fig. 2.10c under hydrogen-charged conditions for Case 2). Stress value elevated beyond a critical value is considered to induce a stress-driven premature failure around these grain boundaries and triple junctions [41]. On the other hand for Case 1, hydrogen induced increased dislocation density but lower stress levels (due to the strong softening effect considered) puts the need for an additional HE mechanism to govern ultimate fracture. Though not investigated here explicitly, high dislocation density implies increased hydrogen transport by mobile dislocations. This mechanism is considered to transport the excess amount of hydrogen toward the grain boundaries and triple junctions leading to decohesion by reducing the grain boundary cohesive energy (via the HEDE mechanism). Increased dislocation activities in both cases can indeed assist in transporting excess hydrogen toward the grain boundaries/obstacles. In case 1, the primary role of H-induced increase in dislocation activities will be to raise hydrogen concentration at the obstacles/grain boundaries to promote final fracture ultimately by the HEDE mechanism. Meanwhile, Case 2 replicates a typical scenario where the HELP mechanism can independently raise stresses, leading to premature failure, and also contributes to increasing hydrogen concentration at the grain boundaries, which is required for the HEDE mechanism. These observations can be viewed in light of earlier experimental observations of Martin et al. [15, 25] where hydrogen-induced increased plasticity is established as an essential ingredient toward the hydrogen-induced inter-granular failure either by elevated stress values or by high

dislocation density induced excessive hydrogen concentration at grain boundaries leading to decohesion. Depending upon the above discussion it can be concluded that hydrogen presence can result in void-induced quasi-cleavage fracture or inter-granular fracture at grain boundaries and triple junctions but under all conditions hydrogen induced acceleration of microstructure emanating from H-dislocation interactions under the HELP mechanism remains an important ingredient. In summary, the presented novel two-way framework helped to understand the hydrogen-dislocation interactions under the HELP mechanism toward accelerating the evolution of the microstructure favorable for rapid void nucleation, stress elevation, and also for providing the local high hydrogen concentrations at obstacles leading to decohesion type (HEDE) mechanism, thus controlling the final failure.

2.5   Conclusion

To simulate hydrogen-assisted deformation and failure behavior of metals instigated by the HELP mechanism of HE, a novel two-way computational crystal plasticity framework is developed. Dedicated to simulating the hydrogen-dislocation interaction under the HELP mechanism, the role of hydrogen in dislocation multiplication, annihilation, and dislocation interaction behavior is well included. Simulation results obtained for single and polycrystalline configurations are discussed in terms of experimentally observed macroscopic tensile curves and microscopically observed dislocation structure evolution behavior. The following are the conclusions drawn from the present work:

1. For Ni material containing weak dislocation type of traps investigated here, hydrogen distribution is primarily dependent on the hydrostatic stress distribution.

2. Early stage deformations simulated in the present work validate the hydrogen-induced modifications in dislocation structures observed experimentally in single crystal and polycrystalline FCC materials.

3. HELP mechanism, simulated in this work, induces macroscopic softening and/or hardening as a result of a trade-off between the hydrogen-induced weakening of dislocation interactions and hydrogen-induced increased dislocation density pointing towards the role of HELP mechanism alone or additional mechanisms (HEDE) required for causing early failure.

Informed by the dislocation-hydrogen interactions, understood earlier via experiments and/or multi-scale modeling techniques, this chapter presented a dislocation density-based crystal plasticity model coupled with a hydrogen diffusion/trapping model to understand the hydrogen-assisted deformation and failure scenarios possible under the HELP mechanism of hydrogen embrittlement. In this work, for polycrystal configuration, grain boundaries are considered as simply the boundary between two adjacent grains of different orientations. Intentionally, no special treatment to grain boundaries in terms of hydrogen

diffusivity, and binding energy is provided, as this chapter is focused on answering the pressing question regarding the role of the HELP mechanism (primarily controlled by dislocation type of traps) towards the final fracture of the material. Nickel-based alloys manifest hydrogen embrittlement by the transition from ductile transgranular (TG) fracture to brittle intergranular (IG) fracture. Besides the interaction between hydrogen and dislocations as studied in this chapter, the grain boundaries (GBs) play a significant role in governing hydrogen-induced intergranular fracture. Different types of GBs, depending on their crystallographic character, can exhibit varying H-diffusivity, trap binding energy, defect concentration, and fracture energy. For the various types of grain boundaries present in complex polycrystal configurations, there is no clear consensus on H-related parameters. Consequently, crystal plasticity-hydrogen transport models capable of accurately simulating hydrogen-dislocation-grain boundary interactions are still in the early stages of development.

Recognizing the limitations inherent in the current state of crystal plasticity-hydrogen transport modeling (CP-HTM) for simulating multifaceted hydrogen-dislocation-grain boundary interactions, and understanding the challenges involved in experimental investigations of complex hydrogen embrittlement (HE) studies, the next chapter introduces a unique experimental strategy employed for the first time in HE research. This upcoming chapter introduces the utilization of tensile *oligocrystal* samples to gain insights into some of the crucial aspects related to the HE behavior of nickel material.

Chapter 3

Hydrogen Embrittlement in Nickel Oligocrystals - Effect of Microstructure

3.1 Introduction

Hydrogen embrittlement (HE) in metallic materials is a longstanding issue and a major bottleneck for a sustainable hydrogen economy. The intricate interplay between hydrogen trapping/transport phenomena, microstructure, and loading conditions, poses a significant challenge in unraveling the precise micro-mechanics responsible for HE. Consequently, the exact mechanism governing the HE in metallic materials is still debatable and is a matter of ongoing research [5, 10]. Due to relatively simple microstructure, Nickel as a material model in single crystal and polycrystalline configuration is extensively investigated for HE studies [1, 15, 23, 48, 51, 52, 57, 85, 88, 89, 90, 91, 92, 93]. In the polycrystalline configuration, HE in Nickel based alloys manifest by transition of fracture mode from ductile transgranular (TG) to brittle intergranular (IG) [15, 23, 24, 25, 89]. Depending upon the hydrogen-dislocation-grain boundaries interaction, there are debates regarding the contribution of individual and concurrent activity of HELP (hydrogen-enhanced localized plasticity) and HEDE (hydrogen-enhanced decohesion) mechanisms of HE to govern the intergranular fracture in Nickel [7, 15, 23, 24, 25, 85].

Though controversy reigns over the exact HE mechanism, the crystallographic character of the grain boundaries (GBs) is considered to be of paramount importance in governing the IG fracture [89, 91]. In general, owing to the less-ordered arrangement of the atoms at the GB plane usually associated with an excess volume, high-angle, high-energy random grain boundaries are considered to have weak resistance to the fracture whereas low-energy and low-angle GBs are more resistant [94]. Also, the high-angle and high-energy random GBs are reported to be more attractive for solute segregation than low-angle, low-energy, and symmetric tilt GBs [95]. Specific to the HE, Oudriss et al., [91, 96] highlighted the impact of grain boundaries type on hydrogen distribution in polycrystalline Nickel. Authors reported the fast hydrogen diffusion along the random high-angle grain boundaries (RHAGBs), whereas the coincidence site lattice (CSL) $\Sigma 3^n$ GBs and low-angle grain boundaries (LAGBs) with low hydrogen diffusivity were observed. Considering these results, in polycrystals with a high fraction of RHAGBs and their connectivity, the short

circuit diffusion of hydrogen along random GBs was considered to be the major cause of HE [91]. Bechtle et al., [89] showed that Ni-201 with an increased fraction of special Σ3 grain boundaries was less susceptible to H-induced intergranular fracture. Hu et al., [97], suggested the improvement of HE resistance through grain boundary engineering (GBE), not only by increasing the number of special boundaries but also by disrupting the connectivity of the RHAGBs network. These findings robustly support the concept of H-resistant materials achieved through GBE, involving the formation of annealing twins or CSL Σ3 type boundaries, optimizing their distribution, and enhancing mutual connectivity [89, 96, 97]. Earlier findings also indicate that only CSL Σ3 grain boundaries are 'special' against the HE as other types of CSL, for instance, Σ5, and Σ11 are susceptible to cracking under H-environment [98, 99, 100]. In contrast to the above observations, Matteo Seita [101] found that the Σ3 twin boundaries in Inconel 725 were most susceptible to crack initiation but resistant to crack propagation. In addition to the absence of a clear consensus regarding the grain boundary type's role in hydrogen-induced intergranular fracture, there is also ongoing research focused on whether hydrogen segregated before the deformation at the GBs alone is sufficient to induce IG fracture or if the presence of impurities other than H (e.g. S), or the involvement of other mechanisms such as hydrogen transport to the GBs by mobile dislocations is necessary to cause IG fracture [7, 25, 95, 102].

It is important to note that the aforementioned observations and associated incongruities are derived while investigating hydrogen embrittlement in polycrystalline configurations. During hydrogen charging of polycrystalline materials, hydrogen preferentially ingresses into the specimens in the proximity of GB intersections with the surface. Referring to hydrogen trapping and diffusion dependent on the GB type, the GB connectivity can majorly affect the hydrogen diffusion from the surface to the bulk of the sample. Specific to the FCC structure of Ni material, the low diffusivity and high solubility of hydrogen lead to a hydrogen concentration gradient along the thickness direction (i.e. high hydrogen in the vicinity of the sample surface and relatively low hydrogen at the mid-sample thickness). Taking into account the impact of dissolved hydrogen on mechanical properties (as also described in Chapter 2), the presence of this H-concentration gradient can result in notable modifications to the mechanical properties of the grains and grain boundaries that are in close proximity to the sample surface, in comparison to the interior grains and GBs [95]. Furthermore, in polycrystals, the grains present along the thickness direction affect the deformation behavior of grains visible on the surface and thus can significantly interfere with the conclusion drawn regarding the activated localized HE mechanism apparent on the sample surface [95, 103].

Experiments on oligocrystals, (i.e. samples containing quasi-2D layer of coarse grains) have gained significant attention to study the deformation behavior of materials due to their advantage of magnifying the micro-level grain-scale phenomenon [103, 104, 105, 106], sometimes even to the naked eye depending upon the size of grains [107]. The oligocrystal does not contain underlying grains in the thickness direction that can affect the deformation of surface grains. Specific to the HE studies, only one layer of grains across

the thickness will ensure similar exposure to all the available grains and grain boundaries to the H charging medium. Consequently, one can draw a better correlation between deformation and microstructure in oligocrystals than in polycrystals. There is an absence of dedicated work devoted to understanding the hydrogen effect on tensile deformation on oligocrystal samples.

Understanding the need to investigate complex HE phenomenon and knowing the absence of sufficient attempts based on oligocrystal microstructure for HE studies, this work is an attempt to investigate the role of hydrogen on Nickel alloy oligocrystals where only a few grains and grain boundaries of interest are present. Specially developed small-scale oligocrystals with nearly one grain along the thickness direction ensure uniform hydrogen exposure for all grain types and grain boundaries, while also preventing the deformation effects of grains extending through the thickness on the surface grains. Moreover, the micron-level thickness of these oligocrystals will further ensure the minimum H-concentration gradient across the thickness direction, consequently, bulk and surface phenomenon will be nearly the same. Electron backscatter diffraction (EBSD) analysis along with the fractographic investigation are conducted to make a one-to-one correlation between the observed microstructure and HE behavior. Moreover, by employing the novel identical oligocrystal approach, the macroscopic tensile stress-strain response and microscopic fracture pattern of both hydrogen-free and hydrogen-charged samples are compared to provide captivating insights into the H effect on fracture behavior. In this chapter, Section 3.2 details the experimental procedure for developing tensile oligocrystal samples, microstructure characterization, hydrogen charging, mechanical testing, and post-tensile analysis. Section 3.3 presents the experimental results which are discussed in Section 3.4.

3.2   Experimentation

Commercially available pure Nickel (Ni-201 alloy with 0.01%C, 0.12%Mn, 0.010%Fe, 0.02%Si, 0.01%Cu, 0.002%S, balance-Ni) plate with 5 mm thickness received in cold rolled condition was annealed at 1300°C for 24 hrs followed by furnace cooling. The heat treatment resulted in equiaxed grains with sizes ranging from a few microns at some locations to large grains up to $\sim$5 mm at other locations. After heat treatment, the tensile-shaped specimens (with gauge length and width of 5 mm and 1 mm, respectively, as shown in Figure 3.1) were extracted from the heat-treated plates using a wire electron discharge machine (w-EDM). The extracted tensile-shaped specimens were further sliced down to a thickness of 0.40 mm. Thus obtained final tensile specimens with desired thickness were polished on SiC paper from 100 to 4000 grit size, then cloth polishing with 6 μm, 3 μm and 0.25 μm diamond paste followed by polishing with 0.04 μm colloidal silica suspension. Finally, electro-polishing with a solution of 20 % Perchloric acid and 80 % methanol at 15 V for 15 s was used to remove residual stresses generated due to mechanical polishing and to prepare the samples with a surface

finish suitable for EBSD analysis. After mechanical polishing and electro-polishing the final sample thickness was achieved ~ 0.35 mm. EBSD analysis was conducted on Bruker e-Flash-HR mounted on scanning electron microscope; JEOL; JSM-6610. Due to variation in grain size obtained after heat treatment, slicing the dog bone-shaped specimen produced three distinct types of specimens: true-oligocrystal, quasi-oligocrystal, and identical-oligocrystal. True-oligocrystals are the specimens having exactly one grain along the thickness direction while having multiple grains across gauge length and width direction. Quasi-oligocrystals are the specimens containing single-through thickness grains at the majority of gauge section area, meanwhile containing some extra grains on both surfaces. The third category is identical oligocrystals i.e. more than one tensile specimen having nearly the same grains and grain boundaries. Figure 3.1 shows the schematic of the methodology adopted for generating the different types of oligocrystal specimens.
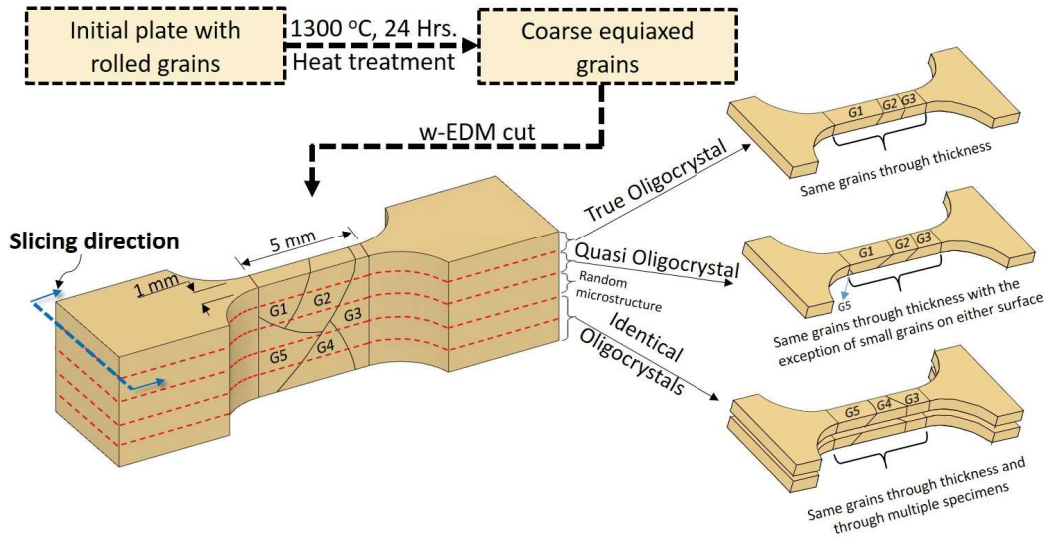
Figure 3.1: Schematic illustration of methodology for obtaining different types of oligocrystal tensile specimens. G followed by a numeric value indicates the grain number

As all types of CSL do not possess the 'special' character against HE, samples containing only one type of CSL i.e. $\Sigma 3$ GBs are investigated in this work. Hence, in the investigated samples the grain boundaries are categorized into LAGBs (low angle grain boundaries with misorientation angle ($2° \leq \theta \leq 15°$), RHAGBs (grain boundaries with misorientation angle $\theta > 15°$ of random character) and special CSL $\Sigma 3$ grain boundaries. Furthermore, to explore the influence of neighboring grains in addition to the GB type on H-induced IG fracture, oligocrystals selected in this study exhibit significant variation in the distribution of the maximum Schmid factor. Table 3.1 presents the microstructural and testing conditions of oligocrystal samples investigated in this chapter. Further details are provided in the relevant sections. For simulating the hydrogen atmosphere, specimens were exposed to an electrolyte containing 1 N H_2SO_4 solution along with 1.4 g/L Thiourea (as charging promoter) under a constant current density of 10 mA/cm^2 for a time period of 12 hrs. Specimen as cathode and platinum mesh as anode were

maintained during hydrogen charging. All the tensile specimens (hydrogen charged and uncharged) were deformed with a strain rate of $5 \times 10^{-4} s^{-1}$ using the tensile-fatigue stage from Kamarath-Weiss. The strain values are measured from the machine cross-head displacement. Post-tensile testing analysis was conducted to investigate the locations of failure and possible HE mechanism by making a one-to-one correlation between the surface in the vicinity of fracture locations and observed fractographic features.

Table 3.1: Details regarding types of oligocrystals and testing conditions

Sample no.	Oligocrystal type	Environment	Strain rate
Sample S1	True-oligocrystal	H-charged	$5 \times 10^{-4}\ s^{-1}$
Sample S2	Quasi-oligocrystal	H-charged	$5 \times 10^{-4}\ s^{-1}$
Sample S3	Identical-oligocrystal	H-charged	$5 \times 10^{-4}\ s^{-1}$
Sample S4	Identical-oligocrystal	Uncharged	$5 \times 10^{-4}\ s^{-1}$

3.3 Results

3.3.1 Hydrogen embrittlement in oligocrystals

Figures 3.2(a-d) display the Inverse Pole Figure (IPF) maps in the loading direction (X), which are obtained from the front and back gauge section areas of tensile oligocrystal samples S1 and S2. These IPF-X maps are derived from the average Euler angle over grains. The capital letter G followed by the integer in Figures 3.2(a-d) represents the grain number (e.g. G3 stands for grain number 3). The presence of an equal number of grains on both faces with nearly the same orientation endorses the existence of a columnar grain structure along the thickness direction for sample S1, which is therefore referred to as a 'True oligocrystal'. In sample S2, there is a dissimilarity in the number of grains on both faces as some small-sized grains appear on each face (see, Figure 3.2b and 3.2d). However, except for these small size extra grains, the majority of the surface area on both faces is covered by single through-thickness grains. Due to these characteristics of sample S2, this sample is classified as a 'Quasi-oligocrystal'. Figures 3.2e and 3.2f display the maximum Schmid factor map calculated for 12 slip-systems (FCC material) of samples S1 and S2, respectively. Note the majority of the grains of sample S1 exhibits a higher maximum Schmid factor value, whereas in sample S2 majority of grains exhibit a lower Schmid factor value (for comparison purpose, the same scale is used to plot the Schmid factor map of sample S1 and S2). In Fig. 3.2(a-f), grain boundaries with red, black, and white color correspond to the LAGBs, RHAGBs and $\Sigma 3$ boundaries, respectively.

For sample S1, tensile deformation after hydrogen charging resulted in the crack initiation (near the bottom edge in the front face) at the GB between the grains G1 and G3. This GB is a RHAGB with a trace nearly perpendicular to the loading direction. After cracking through this GB, the crack further propagated along the GB between the grains G1 and G2 but not along the GB between the grains G2 and G3. The GB between the
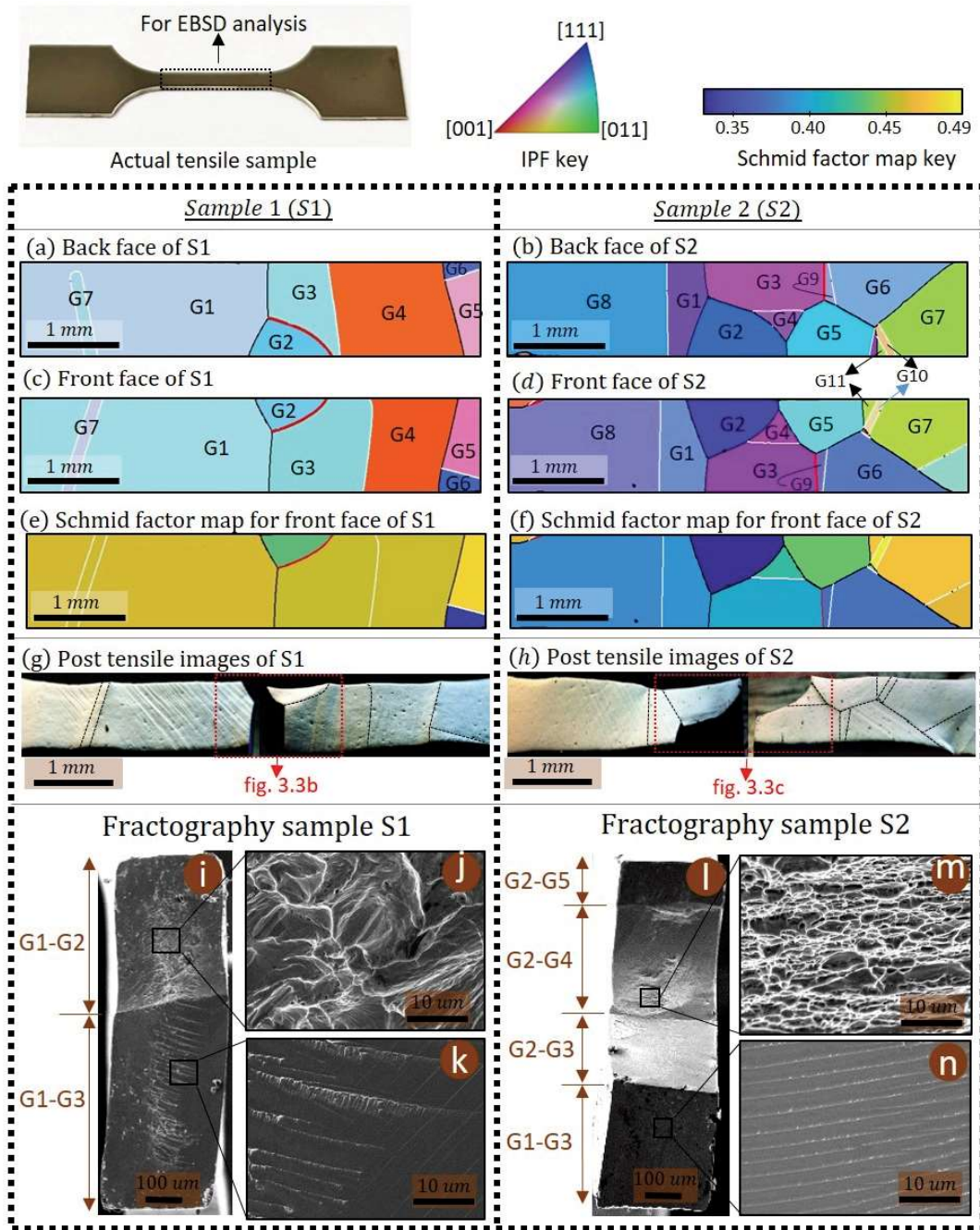
Figure 3.2: Experimental results for sample S1 (left column) and S2 (right column); (a-d) Inverse pole figure in loading direction (e-f) Schmid factor corresponding to front face (g-h) post tensile images where intact GBs are shown with black dotted lines for comparison purpose, and (i-n) fractographic images

grains G1 and G2 is a straight RHAGB, making ~70° angle with the loading direction. In contrast, the GB between the grains G2 and G3 is a curvilinear LAGB and is less inclined to the loading direction. LAGBs are considered more resistant to fracture than RHAGBs [108], whereas the curvilinear geometry and lower inclination angle with the loading direction further contribute toward enhanced fracture resistance [109]. Hence, the propagation of the crack along the GB between grains G1 and G2, rather than the GB between grains G2 and G3, is a consequence of the grain boundary type and its geometric alignment with the loading direction. Comparing the pre-tensile IPF (Fig. 3.2c) with the post-tensile image (Fig. 3.2g) for the front face of sample S1, the complete crack path along the RHAGBs can be evident. Figure 3.2(i-k) show the post-tensile fractographic analysis of sample S1. Figure 3.2i displays a distinct region for intergranular fracture along the GB between the grains G1-G2 and G1-G3. Comparatively more brittle type flat fracture features (with very shallow slip traces) are present near the edges of the specimen, whereas significant plasticity signature can be seen in the mid-thickness of the specimen (see Fig. 3.2(i-k)). Also, some random inclusions were observed on the fractured surfaces. Electrochemical hydrogen charging leads to a concentration gradient across the sample thickness, resulting in a higher concentration near the surface compared to the middle of the specimen [110, 95]. Moreover, the segregated impurities/inclusions at the GBs (near the sample surface) can strongly trap the hydrogen primarily near the surface which further restricts the hydrogen diffusion toward the mid-sample thickness. Subsequently, the flat regions (exhibiting brittle-type fracture) at the edges are primarily due to a high hydrogen concentration, whereas the middle section (displaying plasticity signature) is considered a result of a relatively lower hydrogen concentration. The fracture surface at the mid-thickness regions for the GB between the grains G1 and G2 is accompanied by relatively more plasticity signatures (see Fig. 3.2j) than the fracture surface at the GB between the grains G1 and G3 (see Fig. 3.2k). Considering that both these are RHAGBs, the difference in the fractured surface can be considered due to the relative orientation of the respective GBs with the loading direction. Earlier investigations confirmed that the GBs with trace perpendicular to the loading direction experience higher stress levels [109, 111, 112, 113]. The GB between the grains G1 and G3 is nearly perpendicular to the loading direction whereas this is not exactly the case for GB between grains G1 and G2. For similar H concentration (due to similar GB type and similar H-charging conditions), the higher stresses at the GB between the grains G1 and G3 resulted in the crack to initiate at this site and caused a sudden drop in tensile stress from the UTS value to a stress level of ~50 MPa (see the tensile curve for sample S1 in Fig. 3.3a). In contrast, relatively lower normal stresses at the GB between the grains G1 and G2 resulted in the crack to propagate in a relatively ductile causing a temporary halt in stress drop in the tensile curve from ~50 MPa onward (see two-step tensile curve drop for sample S1 in Fig. 3.3a).

In sample S2, tensile deformation after hydrogen charging resulted in crack initiation at two different locations i.e. first crack along the GB between the grains G1 and G3 followed

by another crack along the GB between the grains G2 and G5. Both these crack initiation sites are RHAGBs with trace nearly perpendicular to the loading direction. The final separation took place by the mating of these two cracks (by crack coalescence) along the GBs between the grains G2-G3 and G2-G4 which are again RHAGBs. Comparing the pre-tensile IPF (Fig. 3.2d) with the post-tensile fracture image (Figure 3.2h) for the front face of sample S2, the complete crack path along the RHAGBs can be validated. Fractographic analysis (Fig. 3.2(l-n)), indicated brittle type flat fracture features on the crack initiation sites (along GBs between grains G1-G3 and G2-G5), whereas signature of ductile fracture (even dimples in mid-sample thickness only) can also be witnessed during crack propagation along the GBs between the grains G2-G4 and also along G2-G3. Similar to the earlier sample, crack initiation resulted in a sharp drop in stress from UTS value which partially recovered around 65 MPa followed by temporary strain hardening before final fracture (see tensile curve for S2 in Fig. 3.3a). Note that the final fracture for this sample took place by crack coalescence along the GBs between grains G2-G3 and G2-G4. The GBs between the grains G2-G3 and G2-G4 are curvilinear and less inclined to the loading direction, these characteristics are responsible for the crack to propagate in a relatively less brittle manner (notice the dimples in Fig. 3.2m). The presence of dimples along the curvilinear crack growth path correlates very well with the significant temporary step two hardening from a stress value of 65 MPa onward. Moreover, the presence of dimples only in the mid-sample thickness and not near the edges is considered due to the H-concentration gradient across the sample thickness as also indicated for sample S1. Under similar charging conditions, both the samples exhibited the H-induced IG crack initiation along the RHAGBs perpendicular to the loading direction, meanwhile, there was no crack along the CSL Σ3 and LAGBs. For sample S2 cracks were initiated at a much lower strain level ∼5 % in contrast to the counterpart sample S1 where the crack was initiated at about ∼13% strain level (see tensile curves in Fig. 3.3a). In addition to the grain boundary structure and grain boundary orientation to the loading direction, the Schmid factor adjacent to the GBs can significantly affect the GB stress level to cause IG fracture [112, 113]. In general, the GB adjacent to the higher Schmid factor grains experience lower normal stresses than the GB adjacent to the lower Schmid factor grains [111, 113]. For sample S1 crack was initiated at a GB located between the grains with a high Schmid factor, whereas for sample S2 cracks were initiated at the GBs located between the grains with a low Schmid factor. This difference in the Schmid factor adjacent to GB alters the stress levels experienced by the GB thus affecting the fracture process. More on the contribution of the Schmid factor across the fractured GBs will be discussed in later sections. Figure 3.3b and 3.3c display the post-fracture grain reference orientation deviation (GROD) maps for selected regions (highlighted in Fig. 3.2g and 3.2h, respectively) in the vicinity of the fracture location for sample S1 and S2, respectively. GROD maps are useful for highlighting localized plasticity in the material structure. In Fig. 3.3b, the GROD value peaks at 18 degrees near the GB between grains G2 and G3 for sample S1. Nevertheless, the GROD value in the vicinity of the fracture location is

relatively lower than this maximum value. It is noteworthy that the fracture in sample S1 occurred along the GB between the grains G1-G3 (initiation site) and G1-G2, rather than at the GB between grains G2 and G3. For sample S2, the observed maximum GROD value is 10 degrees (along GB between the grains G4-G5 and also in grain G4) which is lower than sample S1. As plastic strain increases, the difference in crystallographic orientation between an arbitrary point and the average orientation of each grain (i.e. GROD value), also increases [114]. In sample S1, the fracture occurred at a relatively higher strain level than in S2, hence resulting in a relatively high GROD value in S1 compared to S2. Moreover, similar to sample S1, for sample S2 highest GROD value exists away from the crack initiation sites (i.e. no peaks in GROD value at the GB between the grains G1-G3 and G2-G5 are observed). The absence of maximum GROD value in the vicinity of fracture initiation sites for both samples indicates that the H-induced localized plasticity has a relatively minor influence on the fracture process.
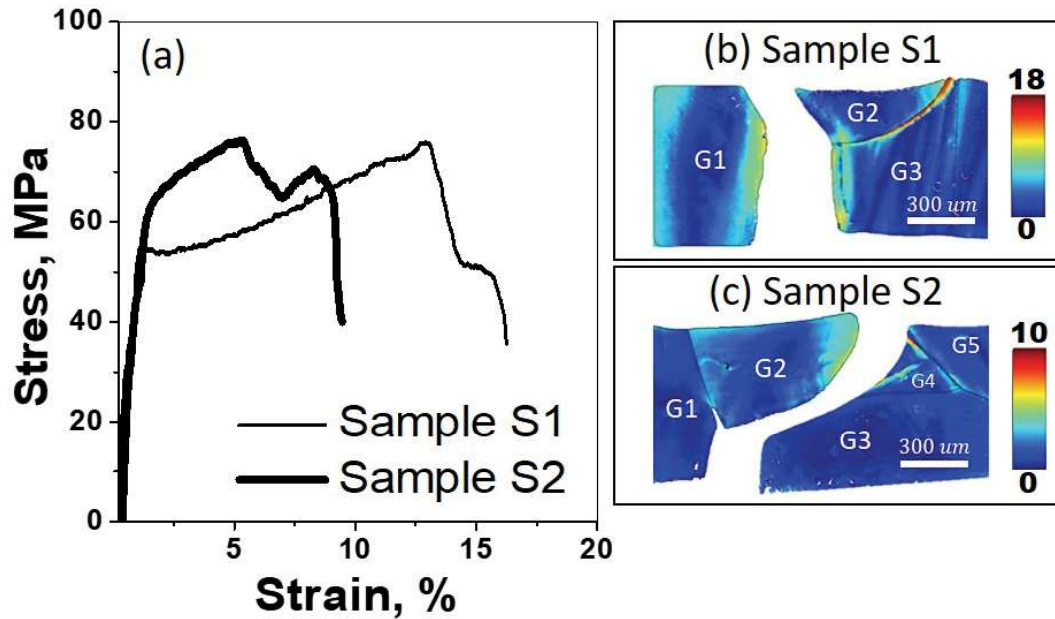
Figure 3.3: (a) Tensile stress-strain curves for samples S1 and S2 (b) GROD map for sample S1 (c) GROD map for sample S2

3.3.2 Effect of hydrogen on identical oligocrystals

Unlike polycrystals, where a large number of randomly oriented grains completely eliminate this effect, oligocrystals with only a few grains exhibit a strong anisotropic effect, leading to variations in mechanical behavior. For instance, when subjected to similar hydrogen charging conditions, the distinct number of randomly oriented grains in samples S1 and S2 resulted in a noteworthy difference in the stress-strain behavior of the two samples. This indicates that while samples S1 and S2 eliminate the effects of through-thickness grains, the overall stress state and deformation response of oligocrystals can be significantly affected by neighboring grains along the gauge length and width

direction. Consequently, the effect of hydrogen charging in terms of macroscopic tensile stress-strain behavior (hardening/softening behavior) cannot be established from the aforementioned samples. Additionally, the heat treatment process employed in this work to generate oligocrystals resulted in the segregation of impurities toward the grain boundaries (some randomly distributed inclusions were observed on the fractured surfaces). Segregation of impurities, other than hydrogen can also cause embrittlement by reducing the cohesive strength along the GBs [24, 95]. Grain boundary types can significantly affect impurity segregation. RHAGBs are considered to be more attractive sites than LAGBs and special Σ3 GBs for the impurities segregation. Consequently, the observed IG fracture in S1 and S2 along the RHAGBs can also be associated with segregated inclusions other than H. In order to differentiate the impact of hydrogen on intergranular (IG) fracture from the influence of segregated impurities and to assess the effects of H-addition on the macroscopic hardening/softening behavior, it is necessary to compare the deformation behavior of oligocrystal samples with nearly the same microstructural features, including grain size, grain boundary types, and neighboring grains in all directions. This comparison should be made between hydrogen-charged and uncharged samples. To accomplish this, one approach would be to examine the deformation behavior of a set of oligocrystal tensile specimens extracted from the same location while ensuring that the microstructure on each face (four faces in total, two on each specimen) is identical. One of the specimens would undergo testing under H-free (uncharged) conditions, while the other would be tested under hydrogen-charged conditions. Conducting tests on samples under H-free conditions will clarify the role of impurities if it is significant enough to cause intergranular fracture in the absence of hydrogen. Meanwhile, testing samples under H-charged conditions will explain the role of hydrogen uptake on the macroscopic deformation response and microscopic fracture pattern. The identical oligocrystal approach used in this work is one such attempt. Details of generating identical oligocrystals are presented in the experimentation section (Section 3.2).

Figures 3.4(a-d) show the IPF in loading direction (for back and front face) for the samples S3 and S4. The slicing method (see schematic as shown in Fig. 3.1) resulted in the replication of nearly similar microstructure on both the samples S3 and S4. Except for a few small extra grains indicated by (#), the presence of the same grains on both the faces of samples S3 and S4 can be seen. For sample S3, except for the one small extra grain (between G1 and G5 on the back face), all the grains (G1 to G10) are present on both faces i.e. G1-G10 are through thickness columnar grains. For sample S4, along with some small size extra grains, grains G1-G10 are present on the back face. However, on the front face of Sample S4, grain G3 is not present. Except for a few anomalies, both the samples display nearly identical microstructure, thus pair of oligocrystal specimens S3 and S4 is termed as identical oligocrystals. Furthermore, in contrast to the earlier samples S1 (featuring the majority of grains with high Schmid factor) and S2 (with grains having a low Schmid factor, particularly around the fractured grain boundaries), there exists a

significant Schmid factor gradient across all the available GBs in both S3 (Fig. 3.4e) and
S4 (Fig. 3.4f). In Fig. 3.4(a-f), grain boundaries with black and white color correspond to
the RHAGBs and Σ3 boundaries, respectively. Note that there were no LAGBs present
in these samples.
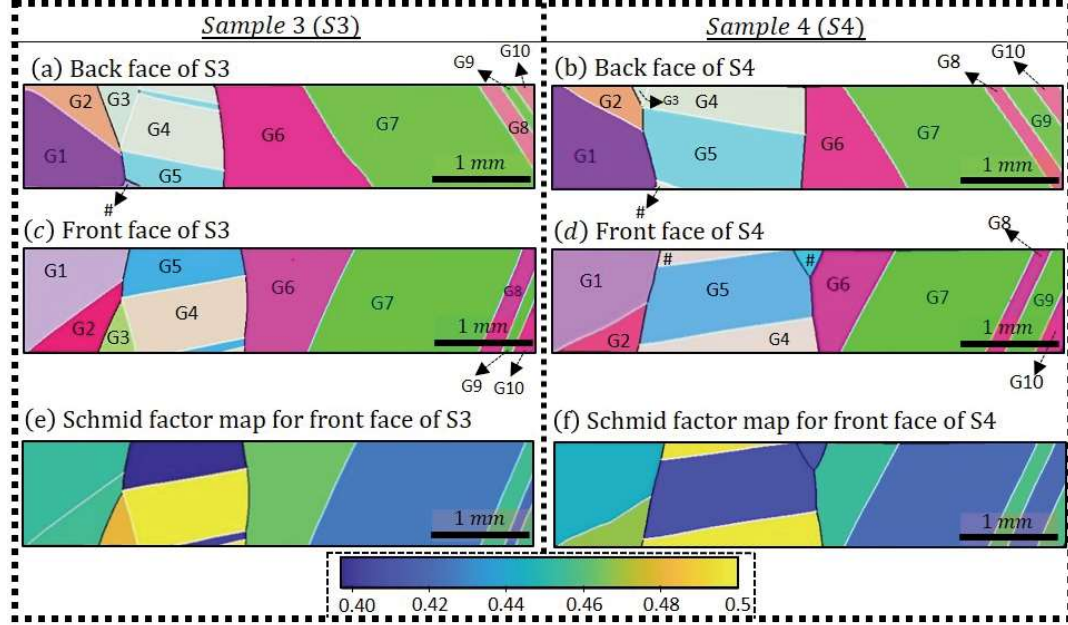
Figure 3.4: Details of microstructure for samples S3 (left column) and S4 (right column),
(a-b) inverse pole figure in loading direction for the back face (c-d) inverse pole figure in
loading direction for the front face (e-f) maximum Schmid factor map corresponding to
the front face. In all the images, RHAGBs and Σ3 GBs are colored as black and white
respectively. IPF color key for (a-d) is the same as in Fig. 3.2

Figures 3.5a and 3.5b show the post-tensile SEM images of samples S3 and S4, respectively.
For H-charged sample S3, the crack initiated along the RHAGB between the grains G1
and G5. The crack further propagated along the connected RHAGBs between the grains
G2 and G5 and then along the RHAGB between the grains G2 and G3 (see Fig. 3.4c for
GB type and 3.5a for fracture location). Similar to the earlier samples there was no crack
associated with any of the special Σ3 GB. For uncharged sample S4, tensile deformation
resulted in the transgranular ductile fracture along the grains/twins G8 and G9 (see Fig.
3.5b). Fractographic analysis shown in Fig. 3.5(c-d) validates the complete IG fracture
for H-charged sample S3 (Fig. 3.5c), whereas ductile transgranular fracture for uncharged
sample S4 (see Fig. 3.5d). It is worth mentioning that even under very high stress and
strain value to failure, uncharged sample S4 failed in a complete transgranular manner.
This indicates that the impurities other than hydrogen did not contribute to IG cracking
and it is solely the uptake of hydrogen causing the transition from TG to IG fracture.
Figure 3.6a shows the tensile stress-strain curve for the H-charged (S3) and H-free (S4)
samples, where a higher yield strength and strain hardening rate for S3 than S4 can be
observed. As the microstructures of both the samples are nearly similar, the increase in
yield strength and hardening rate is considered due to H addition only as also observed
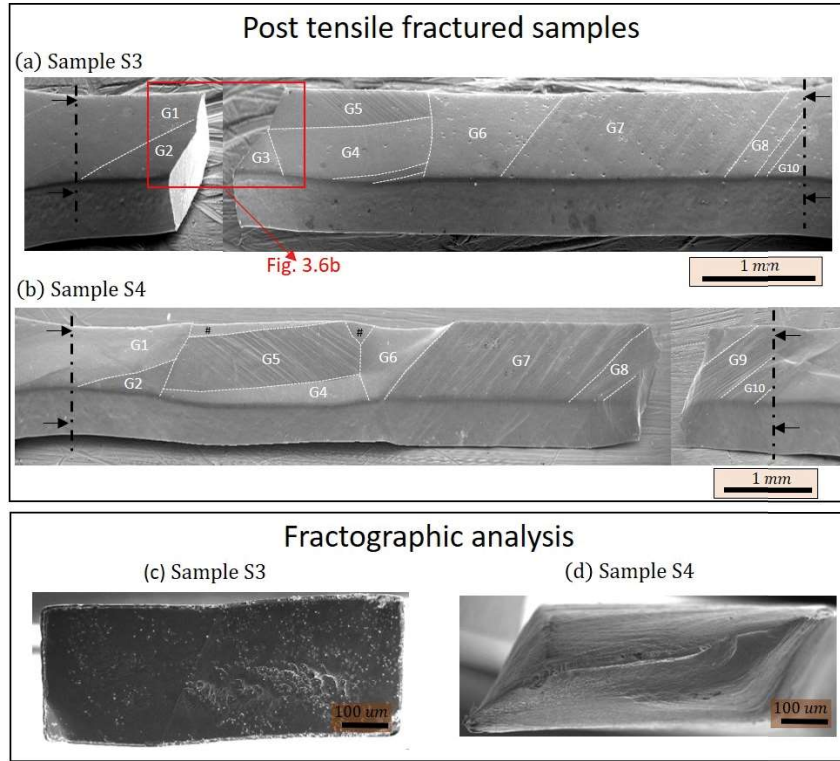
Figure 3.5: Post tensile fracture SEM images for (a) sample S3, (b) sample S4, and (c-d) fractographic analysis of sample S3 and S4. Black lines with arrows are used to mark the gauge section. White dotted lines are used to represent the grain boundaries for comparison purpose

earlier for polycrystals [85]. The H-free sample (S4) displayed a total elongation of ∼52 % while the H-charged sample (S3) fractured with a significantly lower tensile elongation of only ∼9 %. Figure 3.6b shows the post tensile GROD value map obtained from the vicinity of the fractured location (highlighted in Fig. 3.5a) for sample S3. A maximum GROD value of 12 degrees is obtained at a location near the GB between the grains G2 and G3 (see Fig. 3.6b) and not along the crack initiation site along the GB between the grains G1 and G5. Similar to the earlier samples S1 and S2, for S3 there is the absence of a high GROD value at the crack initiation sites suggesting that the H-induced increase in localized deformation in the vicinity of the GB has a negligible contribution to causing the IG fracture initiation. Moreover, once a crack is initiated, the higher stresses at the crack tip of propagating long crack can result in localized plasticity at the adjacent soft regions, which might be a reason of higher GROD value near the GB between the grains G2 and G3.

3.3.3 Effect of hydrogen on tensile deformation of bi-crystals

In the above-discussed H-charged samples S1-S3, RHAGBs are identified crack initiation sites, whereas the CSL Σ3 grains boundaries can be established as a microstructure feature resistance to the fracture. Also, the crack is not observed along the LAGBs (present in
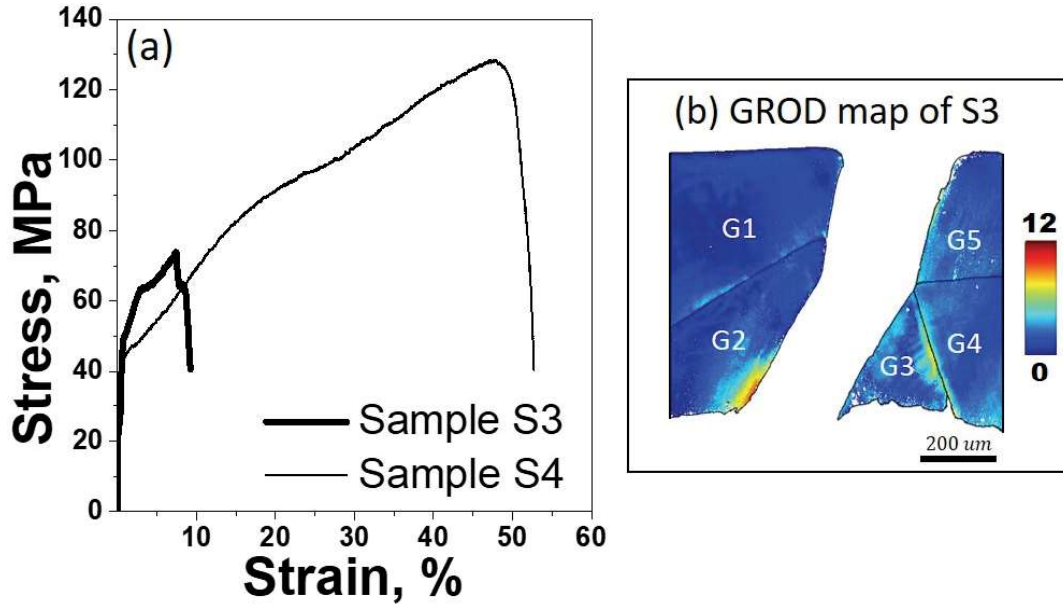
Figure 3.6: (a) Tensile curves for sample S3 and S4 (b) GROD map for sample S3 correspond to the location highlighted in Figure 3.5a

S1 and S2). The lack of cracking along these LAGBs in S1 and S2 can be ascribed to the presence of fewer low-angle grain boundaries (LAGBs) in conjunction with specific microstructural and loading conditions. Moreover, it is highly likely that under the current hydrogen charging conditions, the RHAGBs cracked well before the $\Sigma3$ and LAGBs, thus cracks were absent at these GBs. To understand the role of LAGBs and $\Sigma3$ GBs under the currently simulated hydrogen atmosphere more clearly, two more oligocrystal samples (S5 and S6) in addition to those detailed in Table 3.1 are investigated. Sample S5 contains only one LAGB (within the gauge length) with $\sim 10°$ misorientation angle and S6 contains only one $\Sigma3$ GB. Sample S5 and S6 contain only two grains within the gauge section, thus can also be termed as bi-crystals. Figure 3.7(a-b) shows the IPF-X for one of the faces of the sample S5 and S6. For these samples, both the faces are exactly the same in terms of grains, grain boundaries and the GB plane is nearly perpendicular to the sample surfaces (hence only one face is shown here). Moreover, in Fig. 3.7(a-b) numeric value within the parentheses indicates the maximum Schmid factor for the respective grain. For sample S5, both the grains exhibited a nearly equal maximum Schmid factor value of 0.45. Also, for sample S6 both the grains within the gauge section exhibited a nearly equal maximum Schmid factor value of 0.49. Interestingly, the tensile deformation after hydrogen charging for both samples S5 and S6 resulted in a complete transgranular fracture. Figure 3.7(c and d) displays the post-tensile fracture SEM images for sample S5 and S6 respectively, where the transgranular fracture along the grain G2 (for both the specimens) with no trace of the crack along the GBs can be seen. The fractographic analysis (see Fig. 3.7(e and f)) further acknowledges the complete transgranular ductile fracture for these samples. Figure 3.7g displays the tensile curves obtained for both specimens, in agreement with the observed ductile transgranular fracture with a notably high percentage of elongation.

Observed complete ductile transgranular fracture along with an absence of any crack at the GBs in S5 and S6 establishes the immune nature of LAGBs and Σ3 GBs toward the HE under the current H-charging conditions.
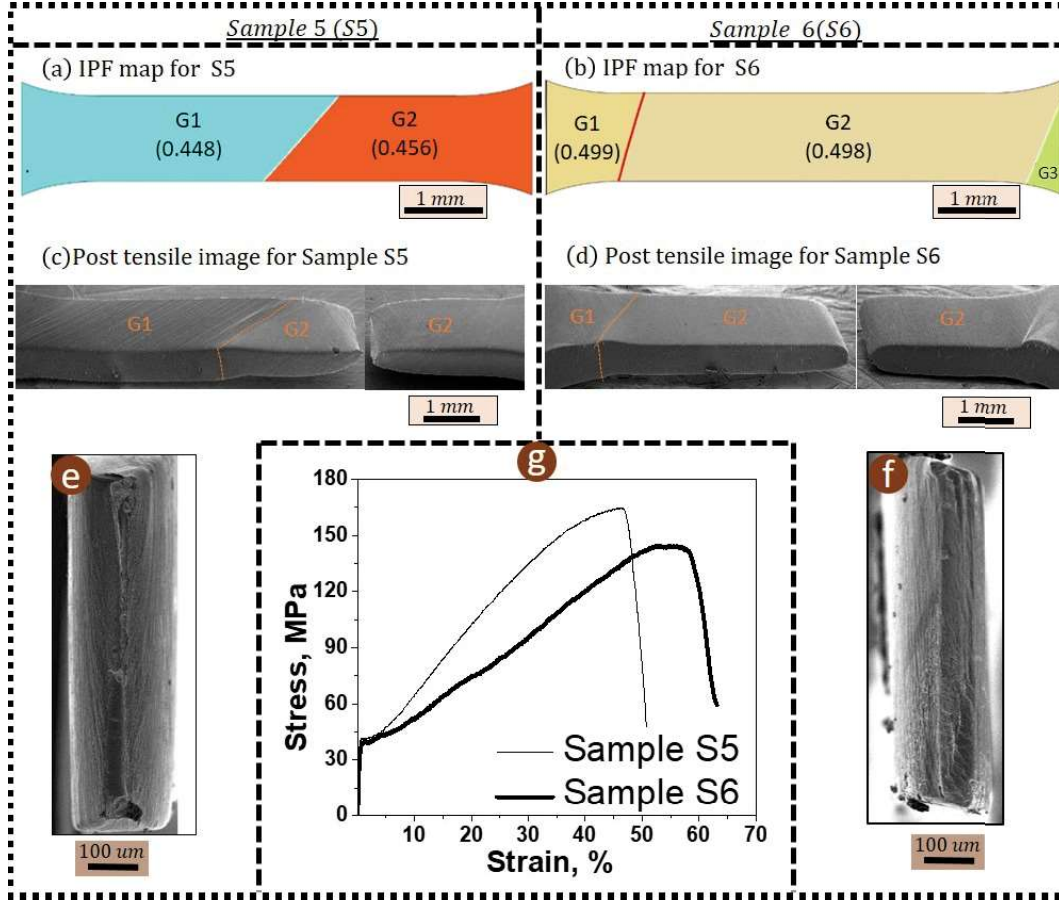
Figure 3.7: (a-b) Inverse pole figure in loading direction, (c-d) post tensile images (e-f) fractographic images, and (g) tensile curves of samples S5 and S6. IPF color key for (a) and (b) is same as in Figure 3.2

3.4   Discussions

Grain boundaries significantly affect the fracture process by serving as preferential sites for crack nucleation and propagation. Not all GBs exhibit the same resistance to fracture; rather, their strength varies based on their type as well as misorientation. RHAGBs have weak resistance to fracture, while LAGBs and symmetric tilt GBs demonstrate greater resistance [94]. The type of GB further influences the segregation of solute content, which can significantly alter the fracture mode by changing the cohesive strength of the respective GB. The solute segregated toward the GB can be characterized from the following relation,

$$C_{GB} \approx C_L \exp\left(\frac{E_b}{kT}\right) \tag{3.1}$$

46

where, C_L is the concentration of solute species in the bulk matrix, C_{GB} is the concentration at the GB, E_b is the binding energy of hydrogen to the boundary, k is the Boltzmann's constant and T is the absolute temperature. CSL $\Sigma 3$ GBs possesses a significantly low trap binding energy of hydrogen [99], which ensures the presence of a significantly low amount of H-concentration at these GBs [99, 115]. Using scanning Kelvin probe force microscopy (SKPFM), Ma et al., [108] characterized that similar to the CSL $\Sigma 3$ GBs, for LAGBs there was hardly any hydrogen segregation. On the other hand, a high trap binding energy leads to a significantly high hydrogen accumulation at RHAGBs, resulting in a pronounced reduction in the cohesion strength of these GBs. Also, the preferential impurities segregation (other than hydrogen) to the RHAGBs can induce IG fracture independently and/or it can modify the hydrogen-grain boundary interaction to promote the IG fracture [24, 95]. The investigated identical oligocrystals resulted in IG cracking in the hydrogen-charged samples only, suggesting that IG fracture is caused by hydrogen uptake rather than any other impurity segregation. Meanwhile, the effect of segregated impurities at the GBs toward altering the hydrogen trapping kinetics cannot be refuted. Earlier studies [115, 116] indicate that the hydrogen concentration segregated at grain boundaries by thermodynamic equilibrium does not reach a level significant enough to cause a notable reduction in cohesive energy required for intergranular fracture. Therefore, it is postulated that hydrogen redistribution during deformation (facilitated by processes such as diffusion due to hydrostatic stress gradients, short circuit diffusion through networked high diffusivity grain boundaries, and/or H-transport through mobile dislocations) is essential to elevate localized hydrogen concentration beyond the critical threshold at fracture sites [15, 18, 96, 117]. Investigated oligocrystals with a discrete number of GBs (thus absence of GB network) are considered to diminish the possibilities of accelerated diffusion by short circuit mechanism across the networked high diffusivity GBs. Additionally, the lower diffusion coefficient value (for FCC Ni) and relatively lower stress levels exhibited by the investigated material make the H-redistribution due to stress gradient also to remain insignificant [117]. Fractographic analysis revealed the slip traces on the flat appearing brittle fractured surfaces (see Figure 3.2k and 3.2n). Earlier investigations associated these slip traces on brittle, hydrogen-induced intergranular (IG) flat fracture surfaces with the phenomenon of hydrogen transport by mobile dislocations [15, 25]. According to this phenomenon, mobile dislocations during the plastic deformation of hydrogen-charged samples can transport a sufficient amount of hydrogen to the grain boundaries. Consequently, the high H-concentration thus achieved can promote the IG fracture via the HEDE mechanism. Nevertheless, it should be noted that the transportation of hydrogen by mobile dislocations is contingent on the strain rate levels, and the strain rate employed in this work is sufficiently higher than the commonly used slow strain rate tensile test (SSRT test with a strain rate of the order $\leq 10^{-5} \ s^{-1}$ or lesser), thus the notable contribution of hydrogen transport through mobile dislocations must be comparatively insignificant [23, 89]. The above discussion indicates the relatively insignificant contribution of hydrogen redistribution during deformation

toward the observed intergranular (IG) fracture in hydrogen-charged samples. This observation is consistent with earlier reports of hydrogen-induced IG fracture occurring even under conditions where hydrogen redistribution by any mechanism remains inactive [23].

The HELP mechanism postulates the acceleration of dislocation activities under a hydrogen atmosphere. The localization of accelerated dislocation activities in the vicinity of GBs can raise localized stresses beyond the critical levels to cause intergranular fracture. GROD maps are useful for identifying the localized changes in material microstructure caused by accelerated dislocation activities [114, 118]. A significantly high GROD value is obtained for the sample S1 only and that too away from the fracture sites. Similar to sample S1, for samples S2 and S3 there was the absence of localized high GROD value at the fracture initiation sites. Moreover, despite the relatively high GROD value in the vicinity of fracture locations, sample S1 showed the highest total elongation to fracture than S2 and S3. These results indicate that the localized plasticity (high GROD value) cannot be accounted as the governing factor for IG fracture in the present work. For samples S1-S3, IG fracture was initiated at the straight RHAGBs with a trace nearly perpendicular to the loading direction. In sample S1, crack initiated after ∼13 % strain along the GB adjacent to the grains making a soft-soft combination (i.e. high Schmid factor grains on either side of GB). For sample S2, the crack initiated at ∼5 % strain along the GBs corresponds to the 'hard-hard' combination (i.e. low Schmid factor grains on either side of GB). Lastly, sample S3 corresponds to the 'hard–soft' combination (i.e. high Schmid factor grain on one side and low Schmid factor on the other side of GB) where fracture initiated after ∼7.5 %. In addition to the GB structure, the Schmid factors in the adjacent grains and the GB inclination to the tensile axis play a significant role in environmental-assisted IG fracture [111, 112, 113, 119]. McMurthy et al., [111] reported that RHAGBs making high surface trace angles with loading direction and adjacent to the low Schmid factor grains are most susceptible to environment-assisted IG cracking. Stratulat et al., [119] reported the preferential IG fracture at the GBs with a hard-hard combination, whereas the hard–soft combination was observed to fail more easily than a soft–soft combination. Pouillier et al., [112] observed the H-assisted IG cracking preferentially at the GBs perpendicular to the loading direction and adjacent to the grains undergoing very limited plastic deformation. Recently, Sun et al., [109] reported that for H-charged Ni, increasing grain boundary curviness requires higher critical stress for cracking than straight GBs. Considering the Schmid factor and the inclination of GBs with respect to the loading direction as crucial factors, West and Was [113] provided 'Schmid-Modified Grain Boundary Stress (SMGBS)' model to predict the effective grain boundary normal stress as:

$$\sigma_N = \sigma_f \frac{m_{avg}}{2} \left(\frac{1}{m_{g1}} + \frac{1}{m_{g2}} \right) (\cos \omega)^2 \tag{3.2}$$

where, σ_N is the normal stress acting on the GB, σ_f is the flow stress, m_{g1} and m_{g2} are the

Schmid factor of grains adjacent to the GB, m_{avg} is the average Schmid factor of sample and ω is the angle between the grain boundary plane normal and the tensile axis (more description in [113, 119]). Table 3.2 shows the GB normal stress value calculated (for the GBs at the crack initiation site) using equation SMGBS model for the samples S1-S3 (for these samples crack initiated at the GBs nearly perpendicular to the loading direction, so the $\cos\omega \sim 1$ is assumed for calculations).

Interestingly, the SMGBS model predicted a similar GB normal stress (i.e. σ_N) for samples S1-S3. Note that even though, there is a significant difference in the strain for crack initiation for S1-S3, however, these strain levels correspond to the nearly same fracture initiation stress of ~ 75 MPa (see tensile curves of samples S1-S3). Using the $\sigma_f = 75$ MPa in Table 3.2, all the samples S1-S3 will exhibit nearly the same GB normal stress. This indicates that the observed IG fracture initiation at the GBs perpendicular to the loading direction in the H-charged samples S1-S3 stems from exceeding critical normal stress at these GBs. These results suggest that the initiation of intergranular fracture observed at the grain boundaries perpendicular to the loading direction in the H-charged samples S1-S3 is a result of surpassing a critical normal stress threshold at these grain boundaries. However, it is important to highlight that the predictive SMGBS model is only qualitative, as it does not take care of the GB structure which however is an important factor for IG fracture. Nevertheless, the similarity in normal stress values predicted by the SMGBS model and the exclusive occurrence of fracture initiation along the RHAGBs in the H-charged samples S1-S3 indicate that the joint interplay of high H-concentration induced reduction in cohesion strength and the presence of critical stress values at RHAGBs is governing H-induced intergranular fracture.

Table 3.2: Predicted σ_N value using SMGBS model (grains adjacent to crack initiation site are considered)

	m_{avg}	Adjacent grains	m_{g1}	m_{g2}	σ_N
Sample S1	0.465	G1 and G3	0.4564 (G1)	0.4529 (G3)	1.023 σ_f
Sample S2	0.407	G1 and G3	0.3885 (G1)	0.4023 (G3)	1.0296 σ_f
Sample S3	0.437	G1 and G5	0.4510 (G1)	0.3974 (G5)	1.034 σ_f

Based on the preceding discussions, it can be summarized that the high trap binding energy of RHAGBs accumulates a high amount of H-concentration (primarily by thermodynamic equilibrium during the H-charging process), which lowers the cohesion strength of these types of GBs thus making it the weakest link of the microstructure susceptible for fracture in H-charged samples. However, a lower concentration of hydrogen at the LAGBs just like CSL $\Sigma 3$ boundaries did not prompt the fracture at these locations. This work indicates that in addition to the crystallographic character of GBs, the Schmid factor adjacent to the GBs and the geometric inclination of the GBs with loading direction contribute significantly to the H-induced IG fracture. The microstructure containing a high fraction of CSL $\Sigma 3$ and LAGBs adjacent to the high Schmid factor grains (as studied in this work) must reveal the high resistance to HE. Furthermore, the presence of geometrically curvilinear grain boundaries that align closely with the loading direction should contribute

to enhanced resistance against hydrogen embrittlement.

3.5 Conclusions

The present work investigated the hydrogen embrittlement behavior in Nickel-201 oligocrystals. Nearly columnar grain structure (through thickness single layer of grains) ensures the uniform exposure of hydrogen to all the available grains and GBs during H-charging. The following are the main highlights of the current work:

- Novel identical oligocrystal approach confirmed the IG fracture due to the hydrogen uptake and not due to any other segregated impurities.

- Bi-crystal type oligocrystals confirmed the immune nature of CSL $\Sigma 3$ and LAGBs under the current hydrogen charging conditions.

- The oligocrystal approach used in this work confirmed that the high hydrogen concentration trapped at the RHAGBs reduces their cohesive strength, thus making it the weakest link in the microstructure prone to intergranular fracture under hydrogen environment.

- Among all the RHAGBs, those with traces perpendicular to the loading direction and located adjacent to low Schmid factor grains experiencing the highest normal stress are observed as the most favorable sites for fracture initiation in hydrogen-charged samples.

Beyond these observations, this study postulated that the interplay of the strain rate used in this work, the lower diffusion coefficient (inherent to the FCC structure), and the lack of an interconnected network of RHAGBs (which can typically facilitate rapid hydrogen diffusion through a short-circuit mechanism) in the examined large-grain-sized oligocrystals, would collectively ensure minimal hydrogen redistribution, both through diffusion and by hydrogen transport by dislocations during the deformation process. In consequence, the observed intergranular fracture at the RHAGBs can be attributed to hydrogen segregation through thermodynamic equilibrium during hydrogen charging prior to deformation. However, since all the samples in this chapter are tested at the same loading conditions (strain rate and temperature), the postulation of insignificant contribution from hydrogen redistribution during deformation is revisited in the next Chapter.

Chapter 4

Hydrogen Embrittlement in Nickel Oligocrystals - Effect of Strain Rate

4.1 Introduction

In Chapter 3, the hydrogen embrittlement behavior of oligocrystal tensile samples made from Nickel-201 alloy is investigated. Heat treatment followed by slicing using the wire-EDM was performed to obtain various types of oligocrystals, including true-oligocrystals, quasi-oligocrystals, identical-oligocrystals, and bicrystal-type oligocrystals. The main goal of the previous chapter was to examine how microstructural factors, including the type of grain boundaries, the orientation of grain boundaries in relation to the loading direction, and the microstructural features near susceptible grain boundaries, contribute to hydrogen-induced intergranular fracture. It is well acknowledged that the hydrogen embrittlement behavior of materials depends on not only microstructure but also on deformation conditions [23, 24, 102]. Previous studies [120, 121] reported that the material's susceptibility to hydrogen embrittlement increases with decreasing the strain rate and vice-versa.

In addition to the previous chapter where all the samples are tested at a fixed strain rate of $5 \times 10^{-4} s^{-1}$, this chapter investigates the effect of hydrogen in the oligocrystal specimens at variable strain rates ranging from 4×10^{-4} to $4 \times 10^{-3} s^{-1}$. These variable strain rates are chosen to provide a clearer insight into the role that deformation plays in inducing the intergranular fracture in H-charged oligocrystals. More specifically, the contribution of deformation-induced hydrogen redistribution (either by stress gradient-induced diffusion and/or due to H-transport by mobile dislocations) in the context of observed intergranular fracture in H-charged oligocrystals is revisited.

4.2 Experimentation

The experimental details regarding the development, hydrogen charging, micro-structural characterization, and post-deformation analysis of oligocrystal samples are provided in Section 3.2. To comprehend the strain rate dependence of the hydrogen embrittlement phenomenon, two true-oligocrystals (sample S1 and sample S2) and a pair of identical oligocrystals (sample S3 and sample S4) are investigated in this chapter. Detailed micro-structural descriptions of investigated samples are given in the relevant sections. All the samples are deformed with variable strain rates ranging from 4×10^{-4} to $4 \times 10^{-3} s^{-1}$

using a miniaturized tensile-fatigue module from Kammrath and Weiss. Tensile testing was performed on H-charged samples S1 to S3 until fracture occurred. Additionally, to examine the H-effect on micro-structural changes at identical strain levels, the tensile test on uncharged oligocrystal sample S4 was halted after reaching a strain level equivalent to the fracture strain observed in H-charged identical oligocrystal sample S3. Subsequently, the microstructure of S4 was examined before proceeding with the tensile test of sample S4 until fracture. Table 4.1 presents the micro-structural and testing conditions of oligocrystal samples investigated in this chapter.

Table 4.1: Details regarding type of oligocrystals and testing conditions

Sample	Oligocrystal type	Environment	Strain rate	Tensile test
Sample S1	True-oligocrystal	H-charged	$4 \times 10^{-4} \ s^{-1}$	Continuous
Sample S2	True-oligocrystal	H-charged	$4 \times 10^{-3} \ s^{-1}$	Continuous
Sample S3	Identical-oligocrystal	H-charged	$1 \times 10^{-3} \ s^{-1}$	Continuous
Sample S4	Identical-oligocrystal	Uncharged	$1 \times 10^{-3} \ s^{-1}$	Interrupted

4.3 Results

4.3.1 Effect of strain rate on HE of oligocrystals

Figures 4.1(a-d) display the inverse pole figure (IPF) map in the loading direction of the front and back face for the gauge section of tensile oligocrystal samples S1 and S2. In these figures, the capital letter G followed by the integer represents the grain number (i.e. G1 implies grain number 1). For sample S1, the presence of an equal number of grains on both faces (see Fig. 4.1a and 4.1c for the back and front face, respectively) with the same orientation validates the existence of a true columnar grain structure along the thickness direction. For sample S2, with the exception of an additional small-sized grain G^* on the front face only, Fig. 4.1b and 4.1d validate the presence of columnar through thickness grains G1 to G10. Figure 4.1e and 4.1f show the maximum Schmid factor map calculated for slip systems of FCC material system of samples S1 and S2, respectively. In Fig. 4.1(a-f), grain boundaries with black and white colour correspond to the RHAGBs and CSL $\Sigma 3$ type grain boundaries, respectively. In samples S1 and S2, no other types of grain boundaries are present.

Figure 4.2 displays the post-tensile fracture analysis for H-charged samples S1 and S2. After H-charging, sample S1 is deformed with a strain rate of $4 \times 10^{-4} s^{-1}$. Figure 4.2a shows the post-tensile fracture image for S1. In this sample, the fracture initiated at once for two different locations, i.e. at the GBs between the grains G3 and G4 as well as between grains G2 and G5. Thereafter the coalescence of these two cracks along the GB between the grains G1 and G4 (visible from the front face only) as well as between the grains G2 and G4 formed a single long crack. Finally, the single long crack thus developed propagated along the GB between the grains G2 and G6, causing complete separation. Figure 4.2e shows the fractographic image confirming the IG fracture for sample S1. Note
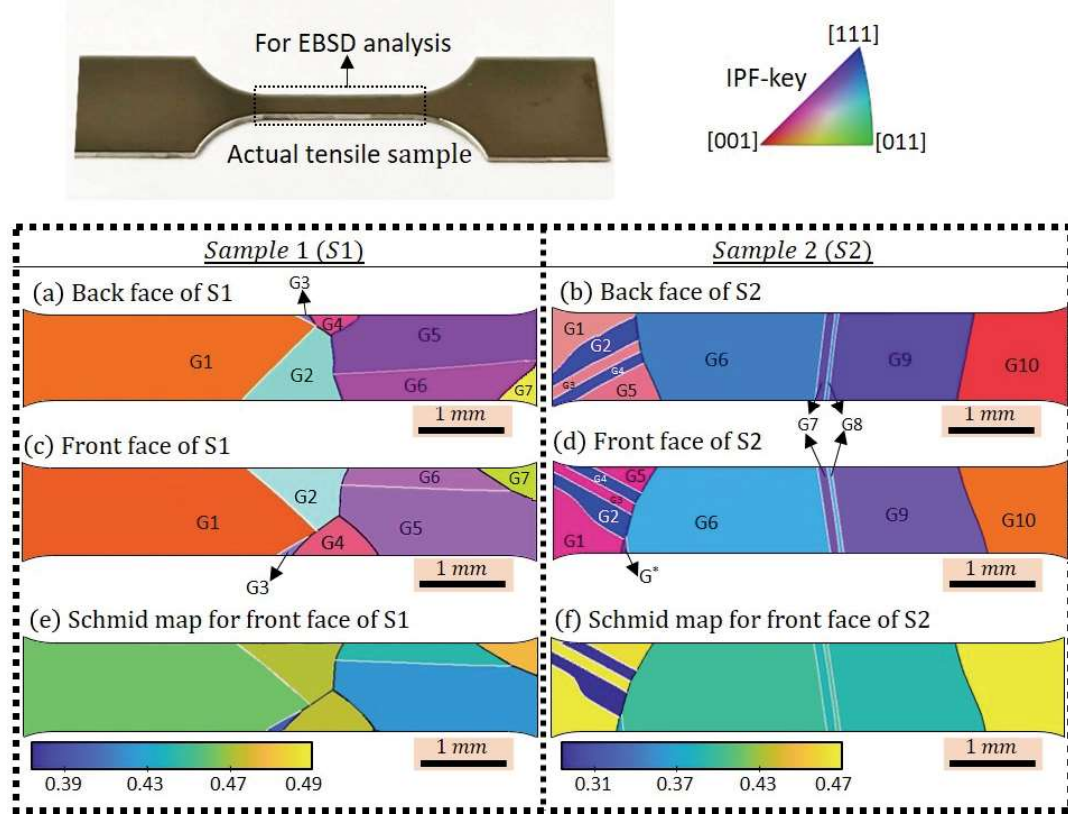
Figure 4.1: Details of microstructure for samples S1 (left column) and S2 (right column), (a-b) Inverse pole figure in loading direction for the back face (c-d) inverse pole figure in loading direction for the front face (e-f) maximum Schmid factor map corresponding to the front face. In all the images, the RHAGBs and $\Sigma 3$ GBs are colored as black and white respectively

that the fractured surface along the crack initiation sites i.e. along the GB between the grains G2 and G5 as well as G3 and G4 is flat, meanwhile, there is a significant signature of plasticity across the fracture region for the GBs between the grains G2 and G4 as well as G2 and G6. Figure 4.2c shows the post-tensile GROD map in the vicinity of the fractured zone for sample S1. Comparing Fig. 4.1c with the post tensile image in Fig. 4.2c, the complete IG fracture path along the RHAGBs only can be validated for sample S1. Note that there was no crack observed at any other location within the gauge section of this sample (see Fig. 4.2a).

Sample S2, after hydrogen charging was deformed at a strain rate of $4 \times 10^{-3} s^{-1}$ (one order higher than S1). Figure 4.2b shows the post-tensile fracture image for S2. Despite a higher strain rate than sample S1, under the same hydrogen charging condition, similar to sample S1, sample S2 exhibited the complete intergranular (IG) fracture. For S2, the crack initiated at one of the RHAGB between the grains G9 and G10 from the upper edge of the front face and then propagated downward along this GB. Figure 4.2f shows the fractographic image confirming the complete IG fracture for sample S2. Similar to sample S1, there was no crack at any other location within the whole gauge section for sample S2.
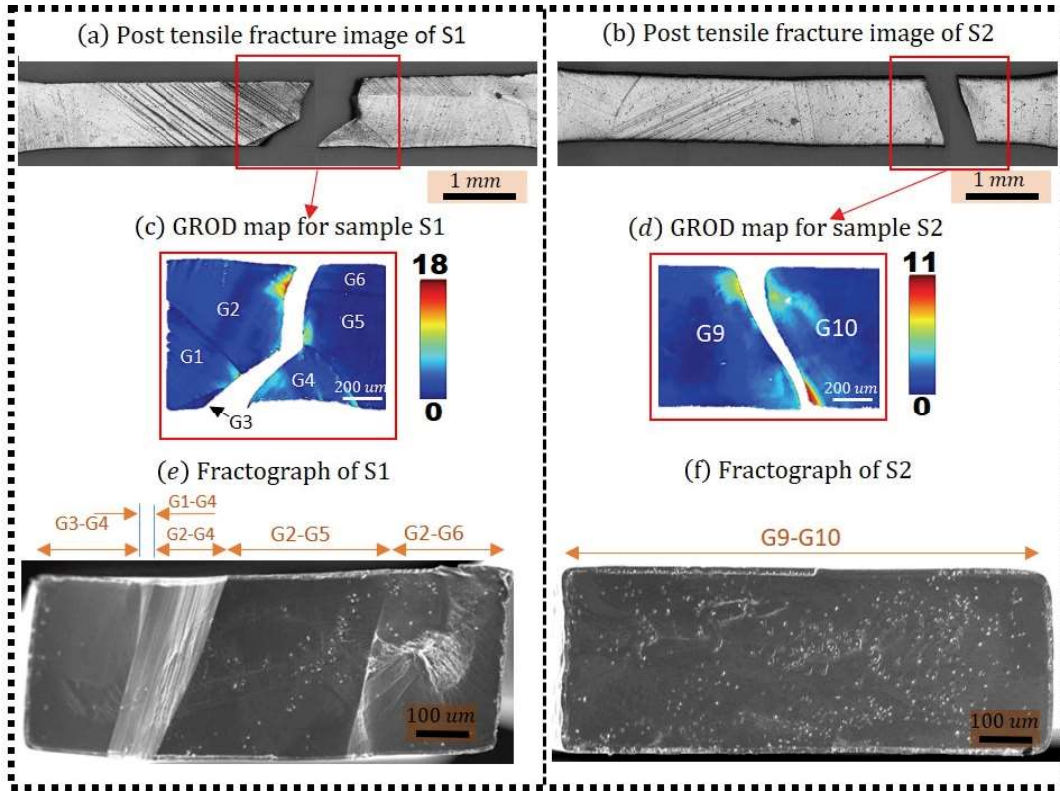
Figure 4.2: Post tensile fracture analysis for sample S1 (left column) and S2 (right column)

Figure 4.2d shows the post-tensile GROD map in the vicinity of the fractured location for sample S2.
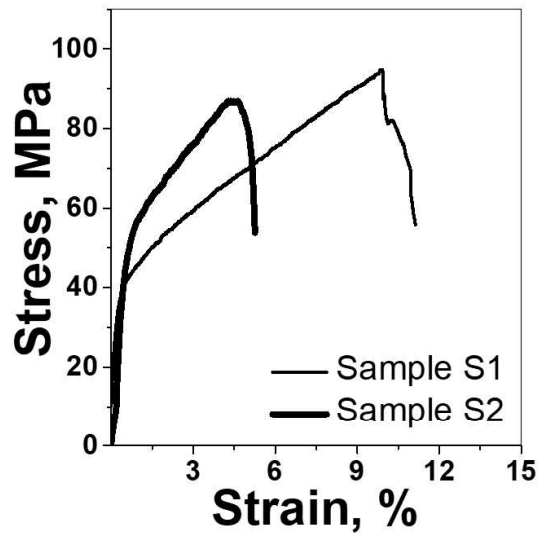
Figure 4.3: Tensile stress-strain curves for H-charged sample S1 and S2

Tensile stress-strain curves for H-charged samples S1 and S2 are shown in Fig. 4.3. Sample S2 (tested at a higher strain rate) exhibited a higher yield stress and hardening rate

while demonstrating a significantly lower strain to failure than sample S1 (tested at a lower strain rate). For H-charged conditions, a high strain rate decreases the dynamic H-redistribution (by restricting the H-transport by dislocations and by limiting the process of H-diffusion) toward the fracture zones (here, GBs). Consequently, the H-charged samples tested at a higher strain rate should exhibit lower H-concentration at the fracture location and thus experience lower HE susceptibility and vice-versa. Considering the slow diffusion coefficient for FCC material and the absence of interconnected GB network (needed for hydrogen diffusion by short-circuit phenomenon) in the investigated large grain-sized oligocrystals, the redistribution of hydrogen by the diffusion can be assumed to remain insignificant [91, 117]. Moreover, the high strain rates used in sample S2 can be considered to further restrict the hydrogen diffusion as well as H-transportation by the mobile dislocations. However, as can be seen from the tensile curves, despite the high strain rate of the sample S2 than S1, S2 exhibited a lower total elongation than S1. Also, both the samples exhibited the complete IG fracture (even S2 revealed a more flat IG fracture surface than S1). These results suggest that hydrogen transportation (by diffusion and by mobile dislocations) is a relatively insignificant phenomenon in the context of hydrogen embrittlement sensitivity in the present work. With the currently investigated level of strain rates, the coarse-grained FCC nickel is expected to demonstrate minimal sensitivity to changes in strain rates regarding mechanical properties [122]. Accordingly, the observed difference in the mechanical properties of samples S1 and S2 is considered purely due to the explicit combination of microstructure and site-specific hydrogen concentration present prior to the onset of deformation only.

GROD map in the vicinity of fracture location for sample S1 (Fig. 4.2c) and S2 (Fig. 4.2d) exhibited the absence of significantly high GROD values at the fracture initiation sites. Moreover, for both the samples the highest GROD value is present at a location where the crack is about to leave the specimen and is long enough to generate high-stress levels at the crack tip which can further result in localized plasticity [114]. Moreover, with an increase in strain level, the difference in crystallographic orientation between an arbitrary point and the average orientation of each grain (i.e. GROD value) also increases. In S1, the fracture took place at a notably high macroscopic strain level ($\sim 11\%$) compared to S2 ($\sim 5\%$). This difference in strain levels can be associated with the relatively higher GROD value observed in S1 than in S2.

4.3.2 Effect of hydrogen on identical oligocrystals

As also observed in the previous chapter, unlike in polycrystals, where a large number of randomly oriented grains completely eliminate this effect, oligocrystals with only a few grains exhibit a strong anisotropic effect, leading to variations in mechanical behavior. Indeed the investigated oligocrystal samples S1 and S2 eliminate the effects of through-thickness grains, nevertheless (in addition to the strain rate effect) the different stress-strain response of S1 than S2 is due to the specific combination of neighboring grains along the gauge length and width direction. Consequently, the effect of hydrogen charging

in terms of macroscopic tensile stress-strain behavior (hardening/softening behavior) cannot be established from the aforementioned samples. Moreover, the different initial grain orientations in the vicinity of the fracture zone can result in different amounts of localized plasticity levels (e.g. in S1 and S2, high GROD values exist in grains with high Schmid factor), thus can affect the observations drawn in terms of activated HE mechanism. Samples S1 and S2 exhibited the H-induced IG cracking along the RHAGBs only, however, a wide range of misorientation angles for RHAGBs can significantly affect the H-segregation behavior and fracture toughness, which otherwise are essential for H-induced IG fracture. Preferential segregation of impurities other than hydrogen at the RHAGBs can also cause embrittlement by reducing the cohesive strength along these GBs or by attracting more hydrogen content toward the GBs [95, 102]. Therefore, it is necessary to distinguish the effect of hydrogen on the IG fracture in addition to the parent material composition. To distinguish the effect of hydrogen on the IG fracture from the base material composition and to address the effect of H-addition on the macroscopic hardening/softening (along with microscopic phenomenon) in contrast to the uncharged conditions, it is recommended to compare the deformation behavior of oligocrystal samples with nearly same microstructural features including grain size, grain boundary types (misorientation angle-axis combination), and neighboring grains in all directions, between hydrogen-charged and uncharged samples. Identical oligocrystals is one of the approaches wherein a set of tensile specimens are extracted from the same location while ensuring that the microstructure on each face (four faces in total, two on each specimen) is nearly identical (in terms of GB type, adjacent grains). One specimen from the identical set of oligocrystals would undergo testing under hydrogen-free conditions, while the other would be tested under hydrogen-charged conditions. Conducting tests on samples under hydrogen-free conditions would help to isolate the role of chemical composition (or impurities other than H) if it is significant enough to cause IG fracture. Meanwhile, testing samples under H-charged conditions will elucidate the role of H-addition on the macroscopic deformation and microscopic fracture response. A schematic of generating identical oligocrystals (sample S3 and S4) by using the slicing method is shown in Fig. 4.4 (refer to Chapter 3 for more details on generating identical oligocrystals).

Figure 4.5(a-d) shows the IPF in loading direction (for front and back face) for the samples S3 tested in H-charged condition and S4 tested for H-free (uncharged) condition. Samples S3 and S4 are generated by the slicing method (see Schematic in Fig. 4.4) and sufficiently large grain size resulted in the presence of the same through thickness grains (G1-G3) in both the specimens. For S4, through-thickness grains G1-G3 covered all the gauge sections on both sides. However, for S3, there is an extra grain G4 present on both sides in addition to grains G1-G3. As per the classification described in Chapter 3, S3 and S4 individually are true-oligocrystals. For both the samples S3 and S4, the GB between grains G2 and G3 is a special CSL Σ3 boundary, while the boundary between grains G1 and G2 is a RHAGB (with angle of misorientation $\sim 36 \pm 1$ degrees). For sample S3, the grain boundary between the grains G2 and G4 is an RHAGB with ~ 36 degree misorientation
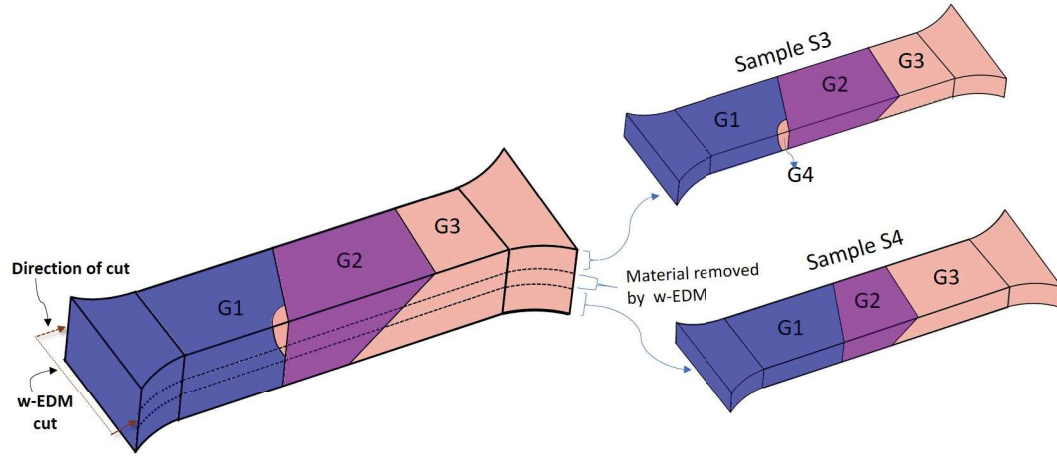
Figure 4.4: Schematic of generating a set of identical oligocrystals S3 and S4

angle, whereas the GB between the grains G1 and G4 is a CSL $\Sigma3$ boundary. Since both the samples S3 and S4 have a similar microstructure (except for an additional small size grain G4 in S3) with the same grains G1 to G3 (and obviously the same type of GB between them) occupying most of the surface area, the pair of specimens (S3 and S4) is termed as Identical-oligocrystals. Similar to the earlier samples S1 and S2, a significant Schmid factor gradient across all the available GBs for S3 (Fig. 4.5e) and S4 (Fig.4.5f) is present. The set of identical oligocrystal samples (S3 and S4) is tested at a strain rate $1 \times 10^{-3}s^{-1}$, which is higher than sample S1 and lower than sample S2.

Figure 4.6 shows the tensile stress-strain curve for the H-charged (S3) and uncharged (S4) samples, where a higher yield strength for S3 than S4 can be observed. Moreover, except for the initial stage, there is not a significant difference in the strain-hardening behavior of both samples. The uncharged sample S4 exhibited complete transgranular fracture with total elongation of $\sim 48\%$. In contrast, the H-charged sample S3 exhibited complete IG fracture and a significantly lower total strain value of only $\sim 9\%$. For H-charged sample S3, the fracture initiated along the GB between the grains G1 and G2 followed by propagation along the GB between the grains G2 and G4 (see Fig. 4.7a for fractured image). For uncharged sample S4, the transgranular ductile fracture occurred along the grain G3 (see Fig. 4.7b). Fractographic analysis in Fig. 4.7c confirms the complete IG fracture for H-charged sample S3, whereas the complete TG fracture for sample S4 can be seen in Fig. 4.7f. It is worth mentioning that even under very high stress and strain value at failure, sample S4 failed in the transgranular manner (fracture occurred in the middle of grain G3, absence of any crack at any location/GB can be validated from Fig. 4.7b). These results indicate that the base material composition and heat treatment process used in this work did not contribute to IG cracking and it is solely the H-uptake causing the transition from TG to IG fracture. In H-charged sample S3, a crack was initiated at GB between the grains G1 and G2. This crack then propagated along this GB and ultimately extended between the connecting GB between the grains G2 and G4. Due to the similar misorientation angle of the GB between the grains G1 and G2 as well as the GB between
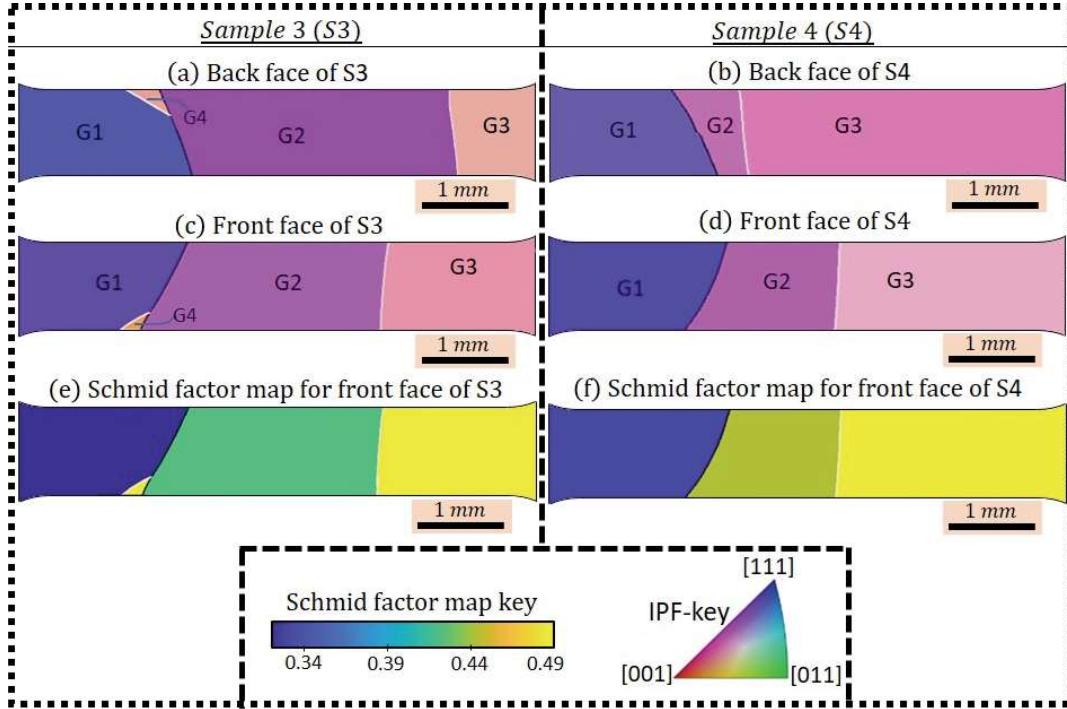
Figure 4.5: Details of microstructure for samples S3 (left column) and S4 (right column), (a-b) Inverse pole figure in loading direction for the back face (c-d) inverse pole figure in loading direction for the front face (e-f) maximum Schmid factor map corresponding to the front face. In all the images, the RHAGBs and Σ3 GBs are colored as black and white respectively

the grains G2 and G4, and their straight-line connection, the fractographic analysis (refer to Fig. 4.7c) reveals the absence of a clearly defined transition zone for cracking along these GBs. High magnification images of sample S3 (Fig. 4.7d and 4.7e) reveal a brittle fracture surface accompanied by very shallow slip traces near the specimen's edges, whereas the increasing intensity of plasticity can be evident toward the mid sample thickness. This difference is considered due to the H-concentration gradient across the sample thickness, resulting in a higher concentration near the surface compared to the middle of the specimen as also described in the previous chapter.

Figure 4.8(a and c) display the GROD map for sample S3 along the fractured path (marked with big red colored box in Fig. 4.7a). A high GROD value of 17 degrees can be seen only in the vicinity of the GB between the grains G2 and G4 (see Fig. 4.8a and 4.8c) but not along the crack initiation site along the GB between the grains G1 and G2. This result is similar to the samples S1 and S2, where the highest GROD value is present at a location where the crack is about to leave the specimen and is long enough to generate high-stress levels at the crack tip to cause local deformation. Figure 4.8b shows the GROD map for the sample S3 at the location in the vicinity of the GB between the grains G2 and G3 (marked by the small red colored box in Fig. 4.7a). To compare with the uncharged counterparts, the GROD map after a strain level of 9%, extracted from the location at the GBs between grains G1 and G2 (Fig. 4.8d), as well as from the grain boundary between
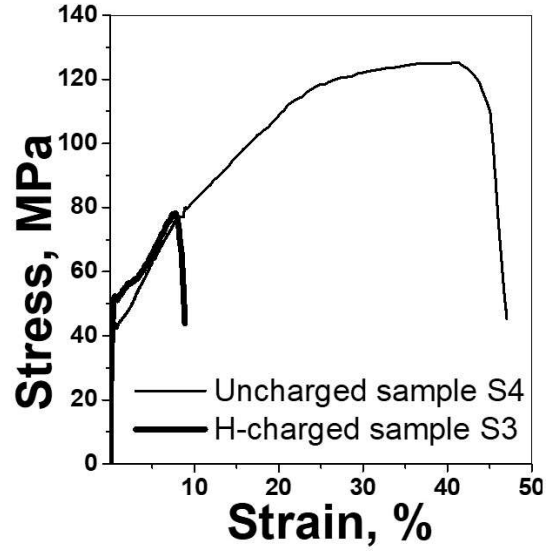
Figure 4.6: Tensile curves for H-charged sample S3 and uncharged sample S4
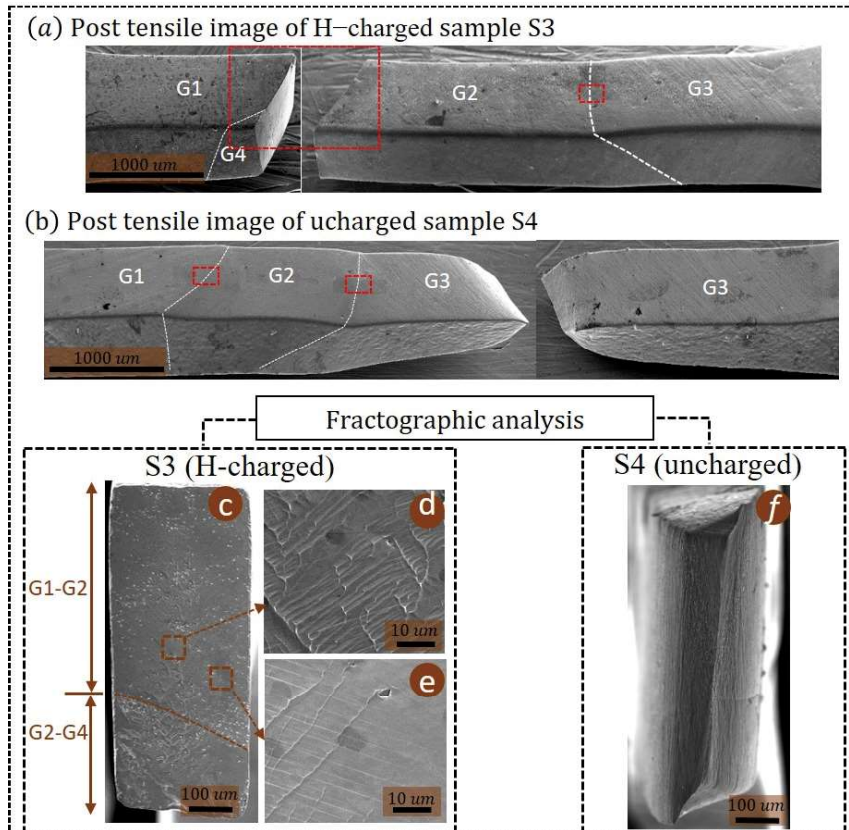
Figure 4.7: (a) Post tensile fracture image for S3, (b) post tensile fracture image for sample S4 (c-e) fractographic analysis of sample S3 and (f) fractographic image of sample S4. White dotted lines are showing the intact grain boundaries. Red color boxes mark the various locations for GROD maps shown in Fig 4.8

grains G2 and G3 (Fig. 4.8e), is presented for sample S4. Comparison of Fig. 4.8b and 4.8e (taken from similar locations for sample S3 and S4, respectively) indicates a higher value of localized plasticity (GROD value) for the H-charged sample S3. Meanwhile Fig. 4.8d shows the absence of any localized plasticity around the GB between the grain G1 and G2 for S4, which is also the case even for the H-charged sample S3.
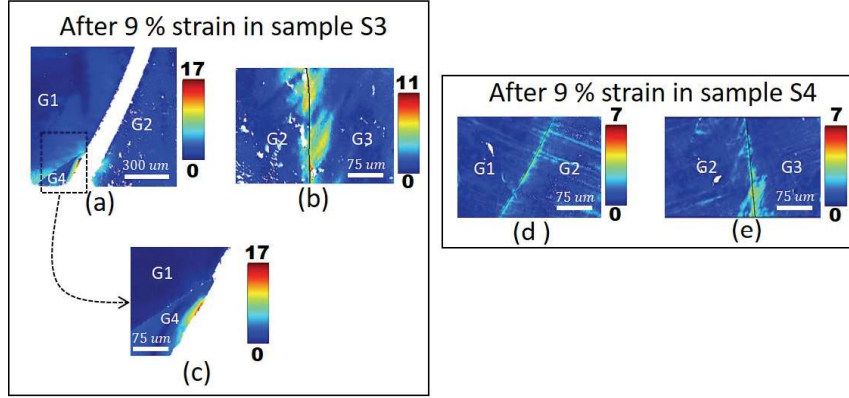
Figure 4.8: GROD maps after 9 % strain for (a-c) sample S3, and (d-e) sample S4

4.4 Discussion

Investigated oligocrystals revealed H-induced IG fracture as a key process for decreasing the macroscopic ductility in H-charged samples compared to the uncharged ones. The transition from transgranular (in the uncharged state) to intergranular (in the hydrogen-charged state) fracture is believed to be determined by a critical combination of hydrogen concentration and stress state developed at the GBs [15, 41, 102]. The type of GBs, inter-connectivity of GBs network, microstructure adjacent to the GBs, and loading conditions can significantly influence the concentration of hydrogen as well as the stress state development at the grain boundary. Pertinent to the investigated oligocrystal microstructure, all types of available GBs experience uniform direct exposure to the H-charging media. Due to the low trap binding energy and low diffusion coefficient, the CSL $\Sigma 3$ GBs is considered to result in an insignificant H-concentration segregation and through-thickness penetration along these GBs [99, 115]. On the contrary, high trap binding energy associated with the RHAGBs results in a high thermodynamically segregated H-concentration, whereas their high diffusion coefficient enables the through-thickness distribution of high H-concentration [91, 99]. The first proposition would be that the dissolved high H-concentration penetrated through thickness along the already weak RHAGBs can reduce the cohesion strength (via classical HEDE mechanism) dramatically. Thus RHAGBs are the weakest link in the H-charged samples responding to the applied remote stress and the local microstructure level stresses. Previous numerical investigations reported that the H-concentration segregation by thermodynamic equilibrium along GBs is not sufficient to cause IG fracture, thus

suggesting the requirement of additional mechanisms responsible for establishing the required threshold of critical H-concentration at the GBs [115, 116]. Deformation preceding the IG fracture is considered to play a significant role toward generating desired high H-concentration as well as developing critical stress levels at the GBs to cause decohesion at the GBs [15, 37]. During deformation, H-redistribution via diffusion, prompted by hydrostatic stress variations and amplified by the rapid H-diffusion along interconnected high diffusivity RHAGBs, essentially creating a short-circuit diffusion pathway, is one of the effective means to transport excess hydrogen toward the fracturing GBs [91].

In Chapter 2, an analysis of hydrogen redistribution was conducted on small size (overall domain size and grain size) polycrystalline configuration using the coupled crystal plasticity-hydrogen transport model. This analysis specifically considered hydrogen diffusion driven solely by the stress gradient. The polycrystalline configuration was subjected to deformation at a strain rate of $9 \times 10^{-5} s^{-1}$. Within the polycrystalline microstructure, the presence of elastic and plastic anisotropy at the grain level resulted in varying stress (hence, hydrostatic stress driving diffusion process) distributed throughout the microstructure. Those simulation results regarding hydrogen diffusion in nickel polycrystals indicated that there was less than 10 % spatial variation in total hydrogen concentration (dominated by diffusible lattice hydrogen concentration). In the current work, the oligocrystals samples are subjected to deformation at a higher strain rate (especially S2). Additionally, a few large-grain regions are considered to result in relatively lesser stress heterogeneity sites. These sites are relatively isolated enough (due to large grain size) to hinder significant hydrogen diffusion during the high strain rate testing. Moreover, the lower stress levels (evidenced by the observed low YS and UTS values) are further expected to cause an insignificant H-redistribution by stress gradient [20]. Furthermore, the investigated oligocrystal microstructure with large grain size and the absence of an interconnected network of high diffusivity RHAGBs is considered to restrict the accelerated diffusion by short-circuit mechanism also.

In the absence of high H-segregation through thermodynamic equilibrium and diffusion-enhanced H-segregation, H-transport by mobile dislocations during plastic deformation is considered to play an important role in raising the H-concentration at the GBs [15]. Nevertheless, it should be noted that similar to the diffusion drive H-redistribution, the transportation of hydrogen by mobile dislocations is contingent on the strain rate levels. During high-strain-rate deformation of materials with a low H-diffusion coefficient, it becomes challenging for hydrogen atoms to continuously move along with mobile dislocations. The insignificance of the dynamic H-redistribution by either mechanism (stress-assisted diffusion and H-transport by mobile dislocations) during the deformation can be validated by comparing the results of H-charged oligocrystal samples S1-S3. Sample S2 is tested at the highest strain rate than S1 and S3 but still exhibits the highest reduction in total strain level, i.e. higher HE susceptibility. The above discussion points toward the insignificance of dynamic H-redistribution toward the

observed IG fracture and is in line with the earlier observed H-induced IG fracture even at relatively high strain rates and also at low-temperature conditions where H-redistribution by any of above discussed mechanisms remains dormant [23, 24]. The insignificance of dynamic H-segregation (by stress-induced hydrogen diffusion and H-transport by mobile dislocations) indicates that H-concentration accumulated by thermodynamic equilibrium during H-charging prior to the onset of straining essentially governs the transition of fracture mode from transgranular (TG) to intergranular (IG) fracture in current work.

The HELP mechanism postulates the acceleration of dislocation activities under the H-atmosphere. The localization of accelerated dislocation activities in the vicinity of GBs can raise stresses beyond the critical level to cause IG fracture [41], as also described in Chapter 2. GROD maps are useful for identifying changes in material structure caused by localized dislocation activities [114, 123]. H-charged oligocrystal samples S1-S3 failed in an IG manner, but there is an absence of significantly high GROD value near the crack initiation sites. Nevertheless, when comparing the GROD value in the vicinity of identical oligocrystal set S3 and S4 samples deformed to the same strain level, H-charged sample S3 revealed a slightly higher GROD value than the uncharged counterpart sample S4. This suggests that the presence of hydrogen has some effect on enhancing localized acceleration of dislocation activities. However, the absence of a high GROD value in the crack initiation site validates that this effect of H-induced increased dislocation activity has a negligible effect on the IG fracture under the current testing conditions. During charging, hydrogen enters from the surface and then diffuses to the mid-sample thickness. The direct exposure of sample surfaces with the H-charging media results in high H-concentration at the surface whereas a relatively lower concentration toward the mid-sample thickness is expected. The presence of a concentration gradient can be evident from the fractographic analysis revealing a flat fracture surface with shallow slip traces near the edges, with relatively intense slip traces at the mid-sample thickness as shown in sample S3. Earlier investigations confirmed the dominance of pure decohesion mechanism under high H-concentration whereas HELP type mechanism plays a significant role toward IG fracture under lower H-concentration [7, 15]. Shallow slip traces near the surface confirm the limited role of H-induced plasticity toward the IG fracture near the edges and the dominance of the HEDE-type mechanism there. Moreover, relatively intense slip traces in the mid-sample thickness can at first be associated with the H-induced accelerated plasticity [15]. However, it is to be noted that for hydrogen to continue influencing dislocation interaction behavior and consequently develop localized microstructural changes, it is essential that the hydrogen atmosphere moves with the dislocations. During high-strain-rate deformation of materials with a low H-diffusion coefficient, it becomes challenging for hydrogen atoms to continuously move along with mobile dislocations, thereby hindering their ongoing impact on dislocation interactions with other dislocations and obstacles, thus resulting in the limited effect of hydrogen in accelerating localized deformation. Currently investigated Nickel-201 alloys (with very low diffusion coefficient) revealed the IG fracture even at a high strain rate for samples

S2 and S3. Insensitivity of the observed H-induced IG fracture to the strain rate and absence of GROD value at the fracture initiation site thus indicates that just like dynamic H-redistribution, the contribution of H-enhanced plasticity must be considered to be secondary or insignificant. The intense slip traces in the mid-sample thickness can be due to the absence of high H-concentration allowing some plasticity before fracture and not necessarily due to the H-accelerated dislocation activities by the HELP mechanism leading to IG fracture.

Based on the preceding discussions, it can be summarized that the high trap binding energy of RHAGBs accumulates a sufficient amount of H-concentration by thermodynamic equilibrium during the H-charging process lower the cohesion strength of these types of GBs thus making it the weakest link of the microstructure susceptible for IG fracture. These weak microstructure features fail under the application of external loadings during which the essential role of plasticity is to increase the stress state by work hardening (not necessarily localized as per the HELP mechanism) ultimately leading to an increase in the critical stored energy at the grain boundaries in excess to the fracture energy.

4.5   Conclusion

In this chapter, the effect of hydrogen in the oligocrystal specimens is investigated at variable strain rates ranging from 4×10^{-4} to $4 \times 10^{-3} s^{-1}$. Conducting tensile tests at varying strain rates on the oligocrystal samples helped in improving the comprehension of the exact contribution of deformation in hydrogen-induced intergranular fracture. Following are the highlights of the work:

- Regardless of the strain rate levels, all the H-charged oligocrystal samples displayed complete intergranular (IG) fracture. This observation suggests that dynamic H-redistribution (prompted by stress variations and amplified by short-circuit mechanism and H-transport by mobile dislocations) is not a necessary factor causing IG fracture.

- All the H-charged samples exhibited the intergranular fracture only at the RHAGBs whereas no crack is observed along the CSL Σ3 GBs.

- Identical oligocrystal samples investigated in this chapter exhibited no significant effect, while in Chapter 3, the identical oligocrystal set displayed an increase in hardening for the H-charged sample. However, despite this difference in the effect of hydrogen on the hardening behavior, identical H-charged samples in both chapters experienced complete IG fracture. This indicates that there is no consecutive relationship between the H-induced hardening and the propensity for IG fracture, however, it may still be considered a minor secondary factor.

- From the present work, the relative insignificance of HELP (Hydrogen Enhanced Localized Plasticity) mechanism-driven accelerated dislocation activities toward intergranular (IG) fracture has been observed.

Based on the above results and observations, it can be concluded that, in the context of the oligocrystal samples, direct exposure of the RHAGBs with high H-trap binding energy to the H-charging media leads to the accumulation of a substantial concentration of hydrogen at these sites through thermodynamic equilibrium during the H-charging process. This elevated hydrogen concentration reduces the cohesion strength of these particular types of grain boundaries, rendering them the weakest links in the microstructure and, consequently, more susceptible to intergranular (IG) fracture. In the H-charged samples, these weakened RHAGBs fail when subjected to external loads where plasticity plays an essential function in generating critical stress levels at the susceptible RHAGBs through work hardening.

To corroborate the experimental observations presented in this chapter, the next chapter employs a coupled crystal plasticity-phase field fracture model to simulate the experimentally observed behaviors, including ductile transgranular fractures in uncharged conditions and brittle intergranular fractures in conditions where hydrogen is charged in oligocrystal samples.

Chapter 5

Crystal Plasticity- Phase Field Fracture Model for Nickel Oligocrystals

5.1 Introduction

Understanding the fracture evolution behavior of metallic materials holds great scientific significance owing to their extensive usage in numerous structural applications. The intricate interplay of microstructural features such as grain orientation, grain boundary characteristics, and defect concentration prompts a diverse range of mechanical properties, culminating in the final fracture mode in transgranular and/or intergranular. Over the past few years, numerical modeling has emerged as a powerful tool for designing materials with improved mechanical properties and enhanced performance under different loading and environmental conditions. Crystal plasticity finite element method has been widely used to investigate the deformation behavior of crystalline materials ranging from single crystal to single/multi-phase polycrystalline materials [124, 125, 126, 127, 128]. Although computational models based on crystal plasticity for simulating deformation in crystalline materials have advanced significantly over the past few years, the prediction transgranular and/or intergranular crack propagation in crystalline materials is still in its early stages of development [128, 129].

Several alternative approaches have been employed for simulating crack propagation in continuum materials. Many of these methods employ linear elastic fracture mechanics (LEFM) to describe material cracking at the macroscopic level. These include the extended finite element method (XFEM) [130], generalized finite element methods [131], the discontinuous Galerkin approach [132, 133], and cohesive zone models (CZM) [134, 135]. The XFEM and CZM modeling approaches are mostly used in conjunction with the crystal plasticity model to simulate the failure behavior in crystalline materials [136, 137, 138, 139]. XFEM has the advantage of avoiding the need for adaptive remeshing as the mesh remains generally independent of the crack geometry. However, obtaining augmentation functions for 3D crack tip fields can be challenging when dealing with plastic slip on crystalline lattices. Additionally, representing crack surface topology using 3D level-set functions can be particularly problematic in the presence of inherent grain-scale variations in multigrain microstructures [140, 141, 142]. On the other hand, CZM requires

cohesive elements embedded between adjacent finite elements along the projected crack path with special traction–separation constitutive relations. A major shortcoming with CZMs in the polycrystalline plasticity framework is that they require a-priori knowledge of crack paths for inserting the traction–separation laws in the computational model. These methods often require modification to the FE formulation, mesh adaptation, element deletion, or explicit mesh separation, which are computationally inefficient when dealing with cracks with non-planar 3D surfaces [143].

The phase field method for fracture [144, 145, 146, 147, 148, 149, 150] has emerged as a promising variational approach to overcome the limitations associated with the discontinuity-based methods. This approach is based on the regularization of a sharp crack surface through an auxiliary scalar field variable or order parameter $\phi \in [0, 1]$ to represent the crack topology. The original sharp crack discontinuity is approximated by a smooth transition between the uncracked ($\phi = 0$) and fully-cracked ($\phi = 1$) material phases. The evolution of the phase field parameter ϕ with deformation and loading inherently represents the crack growth process. Appealing characteristics of the phase-field model are its robustness, flexibility, easy incorporation into a conventional Finite Element Method (FEM) framework, and its capability to model the crack initiation, propagation, and coalescence in arbitrary geometries and dimensions without the need for remeshing [145, 151, 152]. Since the initial work by Francfort and Marigo [153] substantial efforts have been dedicated to improving solution methods [145, 154], refining discretization strategies [155], and addressing implementation aspects [151, 152, 156, 157, 158, 159, 160]. Over the past few years, phase field fracture modeling has proven to be successful in various applications, including simulating brittle fracture [152, 161, 162], ductile fracture [157, 163, 164, 165], ductile-brittle transition [160, 166], and stress corrosion cracking [167, 168], among others. Recently, phase-field fracture model is applied to simulate the hydrogen embrittlement in elastoplastic materials [152, 168, 169, 170, 171, 172, 173]. The phenomenal plasticity model are widely coupled with the phase filed fracture model without clearly considering the corresponding physical mechanisms. Lorezis et al., [174] combined a kinematically linear crystal plasticity model with phase field model for simulating ductile fracture in a single crystal material. Shanthraj et al., [175] integrated the phase field fracture model with a phenomenological crystal plasticity model to simulate brittle fracture in polycrystalline configuration. Cheng et al., [143] and Tu et al., [176] developed a wavelet-enriched adaptive finite element model for solving coupled crystal plasticity-phase field model to simulate crack propagation in polycrystalline microstructures, effectively reducing the computational time required for solving this coupled model while demonstrating exceptional convergence properties. Based upon the observations and recommendations by Borden et al. [157], regarding modeling ductile damage using phase field fracture, Vakili et al. [177] and Maloth and Ghosh [178] have introduced improvements in coupling strategies for crystal plasticity and phase field fracture models. These improvements are intended to produce a ductile damage response that corresponds more closely with experimental results, while also avoiding non-physical

elastic deformations. Despite the numerous attempts to model the fracture phenomenon using coupled crystal plasticity-phase filed fracture models, not a single attempt is made to analyze the fracture in experimentally developed real microstructures. Applications of the coupled framework of CP-PFM on the real experimentally developed oligocrystal will be useful to bridge the gaps between the experimental observations and numerical findings. The use of real experimentally developed oligocrystal samples (containing nearly a single layer of a discrete number of grains) minimizes the need for additional assumptions related to microstructural aspects such as number of grains, grain orientation, grain boundary types, relative grain arrangements (in all directions), grain boundary network and boundary conditions among others.

Chapters 3 and 4 involve experimental investigations focused on understanding the role of microstructural aspects and loading conditions toward the transition from ductile transgranular to H-induced intergranular fracture in oligocrystal samples. In this chapter, a coupled crystal plasticity-phase field fracture model is developed to simulate experimentally observed ductile transgranular (in uncharged) and brittle intergranular (in H-charged) fractures in oligocrystal samples. Building upon the observations from previous chapters, the subsequent sections of this chapter outline the key assumptions that form the basis of the current simulation framework. Following this, the formulation of the coupled deformation-damage framework, numerical implementation, the obtained results, and ultimately, the emergence of important findings are discussed.

5.1.1 Summary of experimental observations and key assumptions for coupled framework

While investigating the intricate phenomenon of hydrogen-induced intergranular (IG) fracture in polycrystalline structures poses significant challenges, employing simplified oligocrystal microstructured tensile samples with a discrete number of grains and grain boundaries offers distinct advantages as detailed in previous chapters. In Chapter 3 different types of oligocrystal samples (true, quasi, identical, and bi-crystal type oligocrystals) with distinct microstructure (in terms of GB types and Schmid factor distribution) are investigated. In Chapter 4, the effect of strain rate is investigated on nearly true-oligocrystals. Important observations from the experimental work (Chapter 3 and Chapter 4) are:-

- All the uncharged oligocrystal samples exhibited ductile transgranular fracture. This indicates that the material composition and heat treatment process is not responsible for IG fracture.

- In the H-charged samples, IG fracture occurred exclusively at the RHAGBs, while LAGBs, similar to CSL Σ3 GBs, remained intact. This implies the resistance of LAGBs and CSL Σ3 GBs to hydrogen embrittlement under the presently employed testing conditions.

- H-charged bi-crystal type sample containing only CSL $\Sigma 3$ and/or LAGBs (i.e., samples S5 and S6 in Chapter 3) exhibited transgranular fracture at significantly high stress-strain levels, similar to the uncharged samples (i.e., sample S4 in Chapter 3 and Chapter 4). These results suggest that the reduction in total elongation is primarily due to IG fracture along the RHAGBs, while the intragranular regions and non-RHAGBs do not significantly contribute to the decrease in total elongation under the current testing conditions.

- Regardless of the strain rate levels in Chapter 4, all the H-charged samples displayed complete IG fracture. This observation suggests that dynamic hydrogen redistribution (driven by stress and mobile dislocations) is not a necessary factor in causing IG fracture. It appears to be an insignificant contributor to the IG fracture.

- Absence of peak GROD value in the vicinity of fracture initiation sites of H-charged samples indicates the insignificance of HELP-driven accelerated activities toward the GB decohesion.

- In Chapter 3, H-charged samples S1-S3 exhibited the IG fracture initiation at nearly similar flow stress (and nearly similar GB normal stress) but at significantly different total/plastic strain levels. This indicates that the fracture is stress dominated and the role of plasticity other than raising the stresses at the GBs by work hardening (not necessarily H-induced localized work hardening as suggested earlier by Martin et al., [15]) should be minimum and insignificant.

- In Chapter 4, the identical oligocrystal samples exhibited no significant effect, while in Chapter 3, the identical oligocrystal set displayed an increase in hardening for the H-charged sample. However, despite this difference in the effect of hydrogen on hardening between the two chapters, H-charged identical samples in both chapters ultimately experienced IG fracture. This indicates that there is no consecutive relationship between the H-induced increased hardening and the propensity for IG fracture. However, it may still be considered a minor secondary factor.

Pertinent to the oligocrystal microstructure, all type of available GBs experiences uniform direct exposure to the H-charging media. Due to the low trap binding energy and low diffusion coefficient, the special $\Sigma 3$ GBs is considered to result in an insignificant H-concentration segregation and through-thickness penetration along these GBs [96, 99, 115]. Using scanning Kelvin probe force microscopy (SKPFM), Ma et al., [108] characterized that similar to the special $\Sigma 3$ GB, for LAGBs there was hardly any hydrogen segregation. On the contrary, high trap binding energy associated with the RHAGBs can result in a high H-concentration segregation by thermodynamic equilibrium during H-charging. Moreover, the high diffusion coefficient of RHAGBs enables the through-thickness distribution of high H-concentration [99]. Furthermore, the RHAGBs offer a weak resistance to fracture than the special $\Sigma 3$ and LAGBs [94, 95]. Considering the above discussion, which highlights the ineffective role of deformation-induced dynamic

H-redistribution, the HELP mechanism, and the potential segregation of hydrogen at weak RHAGBs, it can be concluded that the high concentration of hydrogen segregated by thermodynamic equilibrium during H-charging itself reduces the fracture energy of RHAGBs significantly. This reduction in fracture energy ultimately results in intergranular (IG) fracture in H-charged samples. In this context, the primary role of deformation is to induce work hardening, effectively elevating stresses and stored energy levels to a critical threshold at the H-susceptible RHAGBs.

In Chapter 4, all the investigated samples are true oligocrystals (i.e. consist of nearly a single layer of grains in thickness direction) with relatively simple microstructure and do not exhibit any specific texture in terms of the Schmid factor. Therefore, this chapter studies the fracture evolution behavior on oligocrystal samples from Chapter 4. Guided by the experimental observations, the presented numerical framework adopts a three-step approach. In the first step, the coupled crystal plasticity and phase-field fracture model is applied to replicate the macroscopic tensile response and microscopic ductile fracture of uncharged identical sample S4. During modeling the ductile fracture of uncharged samples, all the grains and all types of GBs are assumed to have similar fracture energy values. In the second step, the coupled model is used to replicate the macroscopic decrease in elongation for H-charged identical counterpart sample S3, with an additional assumption of a decreased fracture energy exclusively along the RHAGBs. Step 1 and Step 2 are basically used to calibrate the phase field fracture energy (w_c, more detail in following sections) difference at the RHAGBs for H-charged and uncharged conditions. These calibrated values of H-induced reduction in RHAGBs fracture energy are then applied for simulating the fracture behavior in two more samples i.e. S1 and S2. Subsequently, the resulting fracture evolution pattern within the investigated samples is examined. Please note that hydrogen as a degree of freedom is not explicitly solved; instead, its impact is addressed as an ad hoc assumption, as explained in step 2. The rationale behind it is thoroughly justified by the insignificance of dynamic H-redistribution i.e. H-effect is constant throughout the deformation as discussed above. The section below outlines the formulation and numerical implementation of the coupled crystal plasticity and phase-field fracture model used to simulate ductile fracture in S4 and its adaptation for simulating IG fracture in samples S1-S3.

5.2 Crystal plasticity-phase field fracture model

5.2.1 Kinematics of crystal plasticity

In the currently used dislocation density-based crystal plasticity model, the total deformation gradient, $\mathbf{F}$ is multiplicatively decomposed into elastic ($\mathbf{F}_e$) and plastic parts ($\mathbf{F}_p$) as,

$$\mathbf{F} = \mathbf{F}_e \mathbf{F}_p \tag{5.1}$$

The velocity gradient, $\mathbf{L}$ can be written as,

$$\mathbf{L} = \mathbf{L}_e + \mathbf{F}_e \mathbf{L}_p \mathbf{F}_e^{-1} \tag{5.2}$$

where, $\mathbf{L}_e = \dot{\mathbf{F}}_e \mathbf{F}_e^{-1}$ is the elastic distortion-rate tensor and $\mathbf{L}_p = \dot{\mathbf{F}}_p \mathbf{F}_p^{-1}$ is plastic distortion-rate tensor. In the used crystal plasticity framework, the plastic velocity gradient $\mathbf{L}_p$ is composed of slip rates $\dot{\gamma}^\alpha$ on each slip systems as,

$$\mathbf{L}_p = \dot{\mathbf{F}}_p \mathbf{F}_p^{-1} = \sum_{\alpha=1}^{N} \dot{\gamma}^\alpha \, \boldsymbol{s}^\alpha \otimes \boldsymbol{m}^\alpha \tag{5.3}$$

where, $\boldsymbol{s}^\alpha$ and $\boldsymbol{m}^\alpha$ are the orthonormal vectors in the direction of slip and normal to slip plane respectively, for α slip system. $'\otimes'$, symbolizes the tensorial product.

5.2.2 Coupling of crystal plasticity and phase-field fracture model for ductile fracture

Following the earlier work [107, 143, 177, 178], the crystal plasticity and phase field fracture models are coupled by defining the free energy for a damaged material as the sum of elastic, plastic and fracture energy contribution as,

$$\psi = \psi^e(\mathbf{E}^e, \phi) + \psi^p(\eta, \phi) + \psi^\phi(\phi, \boldsymbol{\nabla_0}\phi) \tag{5.4}$$

where, elastic contribution (ψ^e) to the free energy as a function of elastic Green–Lagrange strain tensor, $\mathbf{E}^e = \frac{\mathbf{F}_e^T \mathbf{F}_e - \mathbf{I}}{2}$ and phase field parameter (ϕ) is given by,

$$\psi^e = g(\phi)\hat{\psi}^e = g(\phi)\frac{1}{2}\mathbf{E}^e : \mathcal{C}^e : \mathbf{E}^e \tag{5.5}$$

where, $\hat{\psi}^e = (\mathbf{E}^e : \mathcal{C}^e : \mathbf{E}^e)/2$ is the elastic strain energy of the intact material, $\mathcal{C}^e$ is fourth order elastic stiffness tensor. The function $g(\phi) = [(1-\phi)^2 + xk]$ governs the degradation of elastic energy contribution from undamaged state $(\phi = 0)$ to fully damaged state $(\phi = 1)$, with xk (=0.0001) is a small number added to avoid numerical singularity at $\phi = 1$. The above form of ψ^e will yield the constitutive relations for elastic second Piola stress as [143],

$$\mathbf{S} = \left(\frac{\partial \psi^e}{\partial \mathbf{E}^e}\right) = g(\phi)\mathcal{C}^e : \mathbf{E}^e \tag{5.6}$$

The Cauchy stress, $\boldsymbol{\sigma}$ can further be obtained using push forward approach as,

$$\boldsymbol{\sigma} = det(\mathbf{F}_e)^{-1}\mathbf{F}_e \mathbf{S} \mathbf{F}_e^{T} \tag{5.7}$$

The plastic contribution to the free energy is defined as,

$$\psi^p = g(\phi)\hat{\psi}^p(\eta) \tag{5.8}$$

where $\hat{\psi}^p$ is non-degraded stored energy due to defect formation during plastic deformation. Following the earlier developments [107, 143] the internal state variable η can be parameterized in terms of accumulated slip ($\gamma_{acc} = \gamma$) on each of the crystallographic slip system α i.e. $\eta^\alpha = \gamma^\alpha$. Accordingly, the degrading stored plastic energy is given as [177]:

$$\psi^p = g(\phi)\hat{\psi}^p(\gamma) = g(\phi)\sum_\alpha^{N_s} \int \tau_c^\alpha d\gamma^\alpha \tag{5.9}$$

The thermodynamic driving force conjugate to the internal variable γ^α is given by $\frac{\partial \psi}{\partial \gamma^\alpha} = g(\phi)\tau_c^\alpha$, which represents the slip resistance on the α slip system. Given a set of current slip resistances, in the currently used dislocation density-based crystal plasticity model, the slip system shears with a rate as,

$$\dot{\gamma^\alpha} = \rho^\alpha b v_0 \left| \frac{\tau^\alpha}{g(\phi)\tau_c^\alpha} \right|^n sign(\tau^\alpha) \tag{5.10}$$

where, n is strain-rate sensitivity, b is the Burgers vector length, v_0 is the intial reference velocity, ρ^α is the dislocation density and $\tau^\alpha(= \mathbf{S} : \mathbf{s}^\alpha \otimes \mathbf{m}^\alpha)$ is the resolved shear stress along slip system α. Multiplication of $g(\phi)$ with τ_c results in a ductile damage response, while avoiding nonphysical elastic deformations. Following Mecking and Kocks [68], the dislocation density on slip system α is considered to emerge from the balance between the dislocation multiplication and annihilation along that slip system, as:

$$\dot{\rho}^\alpha = (k_{multi} \sqrt{\rho^\alpha} - k_{annih} \rho^\alpha)|\dot{\gamma^\alpha}| \tag{5.11}$$

where, k_{multi} and k_{annih} are the parameters that govern the dislocation multiplication and annihilation behavior, respectively. For current work, the critical resolved shear stress is considered as [67],

$$\tau_c^\alpha = c_3 \mu b \sqrt{\rho^\alpha} \tag{5.12}$$

where c_3 is a fitting constant to account for interaction among dislocations on different slip systems in an average sense and μ is the shear modulus.

The classical version of fracture energy contribution for small strain analysis is defined as,

$$\psi_{classical}^\phi = \frac{G_c}{2l_\phi} \left(\phi^2 + l_\phi^2 \boldsymbol{\nabla}\phi.\boldsymbol{\nabla}\phi \right) \tag{5.13}$$

where, G_c is the Griffith type fracture energy release per unit area, and l_ϕ is the length scale. A slightly modified version of the fracture energy density is proposed by Miehe et al., [179, 180] as

$$\psi_{threshold}^\phi = 2w_c \left(\phi + \frac{l_\phi^2}{2} \boldsymbol{\nabla}\phi.\boldsymbol{\nabla}\phi \right) \tag{5.14}$$

where w_c is a constant representing specific fracture energy per unit volume. Note, in contrast to the classical version of fracture energy, the phase field parameter ϕ in the

modified version with threshold enters in the linear term. This modified formulation declares a threshold on the initiation of fracture and the order parameter (ϕ) starts to evolve only after a specific amount of energy is stored in the material. After some simple algebraic manipulation along with taking $w_c = G_c/2l_\phi$, both the equations can be cast to the same form [181] such as,

$$\psi^\phi_{threshold} = T(\phi) + \psi^\phi_{classical} \tag{5.15}$$

where, $T(\phi) = [1 - (1 - \phi)^2]w_c$ is the threshold energy. Also, the classical version can be written as,

$$\psi^\phi_{classical} = 2l_\phi w_c \left(\frac{\phi^2}{2l_\phi} + \frac{l_\phi}{2} \boldsymbol{\nabla}\phi.\boldsymbol{\nabla}\phi \right) \tag{5.16}$$

In this work a further modification as suggested by Haveroth et al., [182] is made and the form of used fracture energy in reference configuration is,

$$\psi^\phi = 2w_c \left(\phi + \frac{l_\phi^2}{2} \boldsymbol{\nabla}_0\phi.\mathbf{C}^{-1}.\boldsymbol{\nabla}_0\phi \right) \tag{5.17}$$

$\mathbf{C} = \mathbf{F}^T\mathbf{F}$ represents the right Cauchy Green deformation tensor and $\boldsymbol{\nabla}_0$ is the gradient operator for reference configuration. The specific choice of free energy as in eqn. (5.5), (5.9) and (5.17), will result in a governing equation for phase field variable in the spatial format as [143, 183, 184],

$$2w_c l_\phi^2 \boldsymbol{\nabla}.[\boldsymbol{\nabla}\phi] - 2w_c - \left(\frac{\partial\psi^e}{\partial\phi} + \frac{\partial\psi^p}{\partial\phi} \right) = 0 \tag{5.18}$$

In order to start fracture once a certain amount of energy density is stored in the material, one should require the mechanical driving force to exceed the threshold force. Hence, to have more control on damage evolution behavior, eqn. (5.18) is modified to the form as [185],

$$\left\langle \left(-\frac{\partial\psi^e}{\partial\phi} - \frac{\partial\psi^p}{\partial\phi} \right) - 2w_c(1 - \phi) \right\rangle_+ - 2w_c\phi + 2w_c l_\phi^2 \boldsymbol{\nabla}.[\boldsymbol{\nabla}\phi] = 0 \tag{5.19}$$

The necessary damage irreversibly constraint $\dot{\phi} \geq 0$ is ensured by replacing $(\frac{\partial\psi^e}{\partial\phi})$ and $(\frac{\partial\psi^p}{\partial\phi})$ with $(\frac{\partial g(\phi)}{\partial\phi}H^e)$ and $(\frac{\partial g(\phi)}{\partial\phi}H^p)$, where $(H^e = max_{[0,t+\Delta t]}\hat{\psi}^e)$ and $(H^p = max_{[0,t+\Delta t]}\hat{\psi}^p)$.

5.2.3 Numerical implementation and parameter calibration

A summary of governing equations and boundary conditions for the coupled displacement-phase field fracture problem is provided in Appendix-IV. The current modeling framework is implemented in commercial finite element solver Abaqus using the two-layer scheme similar to [158, 186]. Layer one solves for dislocation density-based crystal plasticity model in the UMAT (User defined Material) subroutine, whereas the phase-field degree of freedom is solved in the UEL (User defined Element) subroutine. Common blocks are used to transfer the data between the subroutines. More details on the

implementation of a two-layer staggered algorithm for phase-field fracture can be obtained in [145, 152, 158, 186]. Figure 5.1 displays the geometric models for samples S1-S4, with the dimensions of length and height the same as used in the experiments (in Chapter 4). However, since all the samples consist of only one layer of grains along the thickness, a fixed thickness of only 100 μm is applied (which is smaller than the original thickness of approximately 350 μm). While this approximation in thickness is expected to yield no significant difference in the results, it will significantly reduce the overall computational cost. For samples S3 and S4, the GB plane normal (for GB between the Grains G2 and G3 of both samples) is not perpendicular to the sample surface normal, thus the geometries for the samples S4 and S3 as shown in Fig. 5.1a and 5.1b are used. However, for samples S1 and S2, the GB plane normal of all the GBs is nearly perpendicular to the sample surface normal (see the front and back face for S1 and S2 in chapter 4), thus the geometric models of these samples are created by simply extruding the 2D face in Z-direction (see Fig. 5.1c and 5.1d). Different colors of grains in Fig. 5.1(a-d) correspond to the average crystallographic orientation in Euler angles (see Table 5.1 for Euler angles of all the samples).
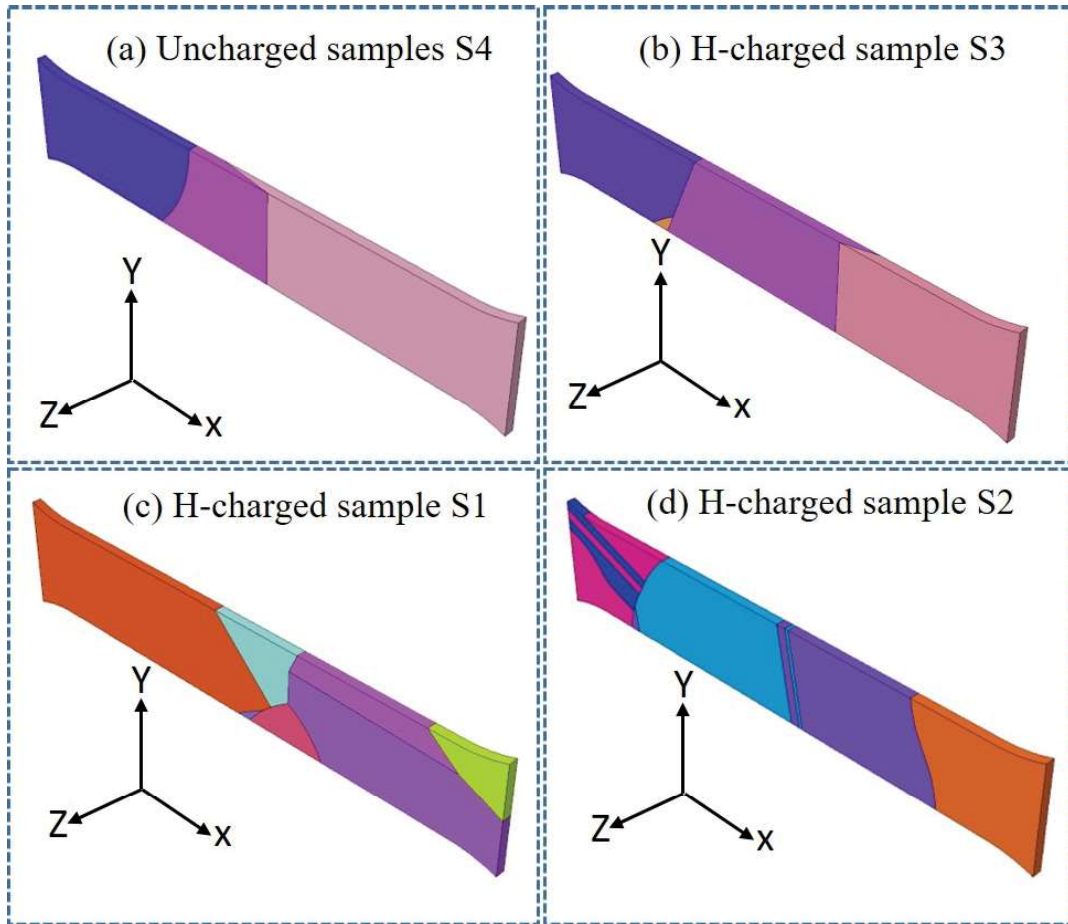
Figure 5.1: Geometry for samples S1-S4 where the color of grains corresponds to the crystallographic orientation obtained from average Euler angles as shown in Table 5.1

Table 5.1: Average Euler angles for the grains in each of the modeled samples. Refer to Chapter 4 for grain number.

Sample	Grain ID	$\Phi 1$ (°)	Φ (°)	$\Phi 2$ (°)
Sample S1	G1	359.0	144.90	352.6
	G2	90.4	144.50	107.6
	G3	129.40	135.70	106.0
	G4	161.70	140.90	167.5
	G5	45.0	142.50	13.0
	G6	321.6	144.70	351.90
	G7	299.90	149.80	305.6
Sample S2	G1	19.9	137.0	9.3
	G2	301.20	140.36	267.7
	G3	19.8	137.70	8.0
	G4	302.8	141.2	267.8
	G5	19.9	137.70	7.0
	G6	246.9	138.30	275.5
	G7	129.2	136.8	174.9
	G8	247.9	137.4	274.6
	G9	131.6	137.70	175.8
	G10	184.8	140.9	177.4
	G^*	129.2	136.40	174.25
Sample S3	G1	39.3	129.5	65.8
	G2	309.7	146.0	341.0
	G3	212.6	146.20	200.50
	G4	166.70	152.40	184.8
Sample S4	G1	43.0	135.5	67.3
	G2	310.9	145.7	344.4
	G3	219.4	147.0	203.1

To simulate the tensile deformation behavior, all the samples are subjected to the same type of boundary conditions i.e. on the left face (at $X = 0$) $u_{x,y,z} = 0$ and on right face (at $X = L$), $u_x = u, u_y = 0$ and $u_z = 0$ is applied. Furthermore, taking into account the requirements of mesh for phase-field fracture model [145] and the crystal plasticity models [187], while considering computational cost and result accuracy (to effectively resolve the fracture process zone and stress-strain values), the developed models are meshed using linear hexahedral elements with an average size of 0.0125 mm. Identical oligocrystal set of samples S3 and S4 (from Chapter 4) is used to calibrate the model parameters (specifically phase-field fracture energy value). At first, the crystal plasticity parameters and phase field energy value are calibrated against the macroscopic stress-strain curve for uncharged sample S4. During this calibration procedure on uncharged sample S4, a uniform value of phase-field fracture energy w_c throughout the microstructure (i.e. all the grains and all types of GBs) is considered. Inspired by the experimentally observed HE-induced IG fracture at RHAGBs responsible for the reduction of overall fracture strain, a reduced value of w_c exclusively at RHAGBs is calibrated for simulating total stress-strain curve for H-charged oligocrystal sample S3. This fracture energy calibrated for RHAGBs under H-charged condition is subsequently used to simulate the fracture behavior of samples S1 and S2. All the samples are deformed with the strain rate exactly the same as used for

the experiments (see details in Chapter 4).

5.2.4 Diffused GB and equivalent fracture energy for H-charged samples

As discussed earlier, the transition from transgranular to intergranular fracture in the investigated oligocrystals occurred primarily due to the H-induced reduction in RHAGBs fracture energy. Accordingly, the transition in fracture modes can be predicted by using a different (here, reduced) fracture energy at RHAGBs than the grain interiors and special GBs (i.e. LAGBs, CSL Σ3 GBs). In this work, an additional auxiliary phase field ϕ_{rgb} is introduced to regularize the material properties at the RHAGBs (for H-charged samples only), forming a new material domain with continuous material properties [188, 189, 190]. Following [189], over a solid arbitrary domain Ω with boundary $\partial\Omega$, the governing equation and boundary conditions of the interface (RHAGB) phase field ϕ_{rgb} can be specified as,

$$\begin{cases} \phi_{rgb} - l_{rgb}^2 \boldsymbol{\nabla}^2 \phi_{rgb} = 0 & in & \Omega \\ \phi_{rgb} = 1 & on & \Gamma_{\phi_{rgb}}, \\ \boldsymbol{\nabla}\phi_{rgb}.\boldsymbol{n} = 0 & in & \partial\Omega \end{cases} \tag{5.20}$$

where l_{rgb} is a regularization parameter that describes the width of the RHAGBs and $\phi_{rgb} = 1$ represents a RHAGBs, $\boldsymbol{n}$ is the outward normal to $\partial\Omega$, and $\Gamma_{\phi_{rgb}}$ describes the surface of the RHAGBs. Diffusive representation of RHAGBs i.e. ϕ_{rgb} can be obtained after determining their spatial locations and material properties. This parameter is also solved in UEL and will not be updated after solving it for the initial step of the simulation. The parameter ϕ_{rgb} is essentially different from the phase field for fracture ϕ, which will be updated to reflect topology changes due to crack propagation. In order to describe the transition of fracture energy between the grains and RHAGBs, the fracture energy for the H-charged samples is assumed as,

$$w_c = w_{rgb}[1 - h(\phi_{rgb})] + w_m h(\phi_{rgb}) \tag{5.21}$$

where w_c represents the equivalent critical energy release rate. w_{rgb} and w_m indicate the representative properties of RHAGBs and matrix (i.e. grains and CSL Σ3 GBs), respectively. Considering the requirement of a monotonous transition between interface and matrix, a form of $h(\phi_{rgb}) = (1 - \phi_{rgb})^3$ is adopted in the present study.

5.3 Results

5.3.1 Phase field fracture simulation of identical oligocrystal samples S3 and S4

Table 5.2 shows the crystal plasticity parameters used for simulating the tensile deformation behavior of all the investigated Nickel alloy oligocrystal. In addition to these parameters, other crystal plasticity parameters $\rho_0 = 7.0 \times 10^6 \ mm^{-2}$, $k_{multi} = 250000 \ mm^{-1}$, $k_{annih} = 7.5$ and phase field related parameters, l_ϕ=0.030 mm, and w_c=75 MPa are

used throughout the model microstructure of sample S4 to simulate ductile transgranular fracture. A comparison of experimental and simulated stress-strain curves for S4 is shown in Fig. 5.2. Figure 5.3a shows the fracture pattern evolution (phase field parameter) for sample S4, wherein similar to the experiments (as in Section 4.3.2) transgranular fracture along the grain G3 can be observed. Moreover, just like experiments, there is no crack at any other location. Good agreement between experimental and simulated macroscopic stress-strain behaviors, alongside the microscopically observed fracture for sample S4 evident in the current framework's adeptness for simulating ductile fractures in real crystalline microstructures.
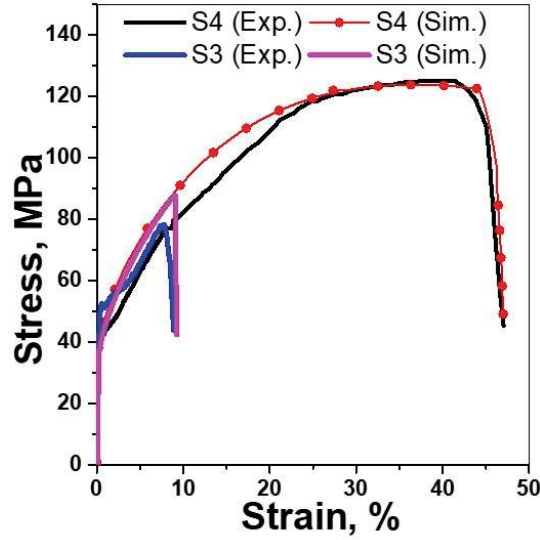
Figure 5.2: Comparison of simulated and experimental stress-strain curves for identical oligocrystal set samples S4 and S3

Table 5.2: The crystal plasticity related parameters used in model

Parameter	Symbol	Magnitude	Units	Reference
	C_{11}	246	GPa	
Elastic constant	C_{12}	147	GPa	[75]
	C_{44}	124	GPa	
Inverse strain-rate sensitivity	n	20	-	[18]
Burgers vector length	b	2.5×10^{-7}	mm	[18]
Slip systems	N_s	12	-	
Reference dislocation velocity	v_0	5	mm$\cdot s^{-1}$	[18]
Scaling constant	c_3	0.5	-	[18]

Because samples S3 and S4 are sourced from the same heat and location, and exhibit identical microstructures while being tested at the same strain rate, the CP-related parameters calibrated for sample S4 are directly utilized to simulate the tensile deformation-induced fracture evolution behavior of sample S3. However, unlike the uncharged sample S4, which employs a uniform fracture energy per unit volume ($w_c = 75$ MPa) throughout the sample, to replicate the experimentally observed H-induced decrease

in macroscopic strain due to IG fracture, for H-charged sample S3, a different (reduced) value of fracture energy along all available RHAGBs is considered. The diffused GB parameter (ϕ_{rgb}) is used to define the transition of fracture energies between the grains (w_m) and RHAGBs (w_{rgb}) as per the eqn. (5.21). To evaluate the diffuse RHAGBs (ϕ_{rbs}), the length scale parameter $l_{rgb} = l_\phi$ is adopted. Note that the special $\Sigma 3$ GBs available in sample S3 are assigned the same fracture toughness values as those used for the grains. Accordingly, the fracture energy per unit volume for the RHAGB region i.e. w_{rgb}=1.52 MPa while for other locations (grains and special $\Sigma 3$ GBs) w_m=75 MPa are selected for sample S3 simulations. Note that the same fracture energy value is applied to both RHAGBs of sample S3 due to their similar misorientation angle ($\sim 36°$) and exposure to the same H-charging condition. This choice successfully replicates the macroscopic strain levels for H-charged sample S3, matching the experimental results. The comparison of macroscopic stress-strain curves obtained from simulation and experimentation for sample S3 is shown in Fig. 5.2. Figure 5.3b displays the fracture evolution pattern of sample S3, mirroring the experimental observations (as shown in Section 4.3.2). Initially, a crack forms at the RHAGB between grains G1 and G2, followed by its propagation towards the connecting RHAGB between grains G2 and G4. It is noteworthy that the reduced fracture toughness along all the RHAGBs makes it equally likely for crack initiation at both these RHAGBs. However, similar to the experiments, the crack first occurs along the grain boundary between grains G1 and G2 before propagating to the grain boundary between grains G2 and G4. This alignment of simulated tensile behavior and fracture evolution with the experimental results provides further validation for the effectiveness of the current model in predicting intergranular (IG) fracture.
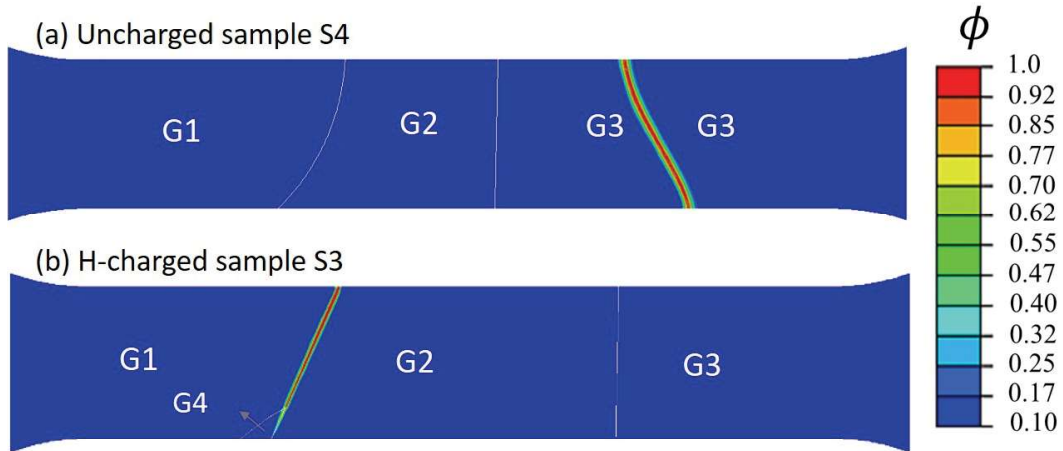
Figure 5.3: Phase field fracture parameter evolution for (a) uncharged sample S4, and (b) H-charged sample S3

5.3.2 Intergranular fracture in H-charged samples S1 and S2

Oligocrystals with few randomly oriented grains display anisotropic mechanical response. Consequently, even after the same H-charging, the experimental stress-strain behavior

(yield strength, hardening rate, and fracture strain) obtained for H-charged samples S1 and S2 is different from H-charged sample S3. In Chapter 2, it was observed that the crystal plasticity parameters ρ_0, k_{multi}, and k_{annih} are most important to replicate macroscopic stress-strain behavior. Accordingly, in addition to the crystal plasticity-related parameters in Table 5.2, for samples S1, $\rho_0 = 9.0 \times 10^6 mm^{-2}$, $k_{multi} = 380000 mm^{-1}$ and $k_{annih} = 7.5$ while for samples S2, $\rho_0 = 1.0 \times 10^7 mm^{-2}$, $k_{multi} = 340000 mm^{-1}$ and $k_{annih} = 7.5$ are used to replicate the macroscopic tensile behavior. Note that these different crystal plasticity-related parameters of samples S1 and S2 from the one used for S3 and S4 is not due to a different effect of hydrogen on the mechanical behavior, rather it indicates the effect of the different number of grains with different size and orientation in all these samples. Moreover, since oligocrystal samples S1-S3 are subjected to identical H-charging conditions, it is presumed that the initial H-concentration and, consequently, the effect of hydrogen on fracture energy along all RHAGBs in samples S1-S3, regardless of their misorientation angle, is similar. Consequently, the fracture energy (for RHAGBs and non-RHAGB regions) value from sample S3 is directly applied to samples S1 and S2. Figure 5.4a and 5.4b display the fracture evolution behavior obtained for samples S1 and S2, respectively. Interestingly for S1 and S2, simulation results displayed fracture along the exact same RHAGBs that fractured in the experiments, while showing no cracks along any other RHAGBs available in S1 and S2.
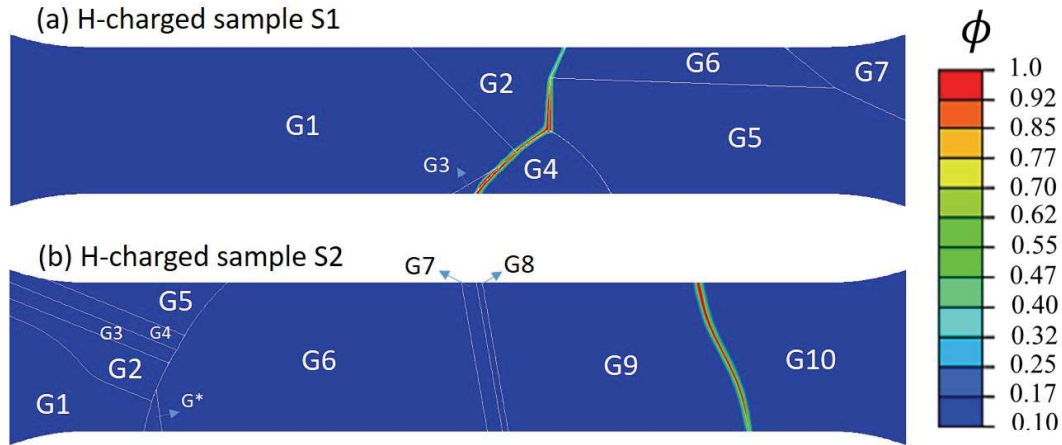
Figure 5.4: Phase field fracture parameter evolution for sample S1 and S2

From the comparison of simulated and experimental tensile curves for samples S1 and S2 in Fig. 5.5, it becomes evident that the simulations under-predicted the impact of hydrogen on macroscopic ductility for sample S2, while accurately predicting the effect of hydrogen on the macroscopic tensile curve of sample S1. The discrepancy between the simulated and experimental macroscopic tensile curve for sample S2 can be attributed to an underlying assumption in the present work. In particular, it is assumed that the reduction in fracture energy caused by hydrogen would be uniform across the RHAGBs in H-charged samples (S1-S3), regardless of their misorientation angles. Sample S2 exhibited a fracture at a RHAGB with a misorientation angle of ∼52°, whereas the angle of misorientation for the

RHAGBs along the fractured path of sample S1 is ~42° (between grains G3 and G4), ~25° (between grains G1 and G4), ~41° (between grains G2 and G4), ~41° (between grains G2 and G5) and ~55° (between grains G2 and G6). The calibration of H-induced reduction in fracture energy is done on sample, S3, which has a misorientation angle along the fractured RHAGBs of ~36°. The fracture initiated for sample S1 along the RHAGBs (at two locations i.e. between the grains G3 and G4, and between the grains G2 and G5) with a misorientation angle of ~41°, which is a situation more close to the sample S3. The significantly high misorientation angle of the fractured RHAGB in sample S2 might potentially have resulted in not only comparatively higher segregation of hydrogen but also other impurities. This, in turn, might have caused a greater reduction in cohesion along the fractured RHAGB for sample S2 than the other two samples. However, the exact dependence of hydrogen-induced reduction in cohesion energy on grain boundary misorientation angle is still open for research.
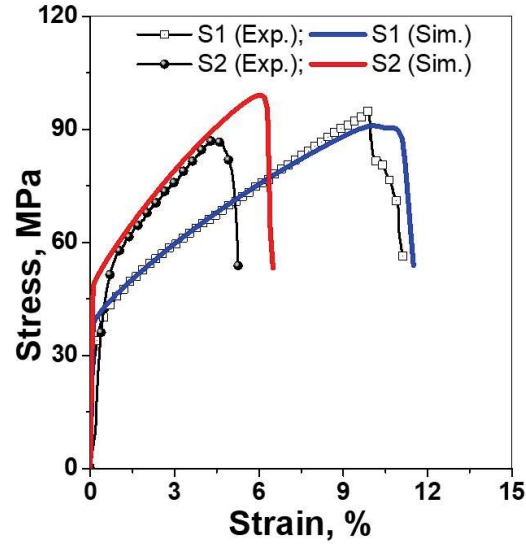
Figure 5.5: Comparison of simulated and experimental stress-strain curves for H-charged samples S1 and S2

5.4   Discussion

The crystal plasticity phase-field fracture model effectively reproduced both ductile transgranular fracture and hydrogen-induced intergranular fracture, aligning with the experimental results. In line with experimental observations, all the simulations of H-charged samples are conducted without any specific treatments aimed at enhancing localized plastic work hardening (via the HELP mechanism) at the GBs. Moreover, as a representative of thermodynamically trapped (during the charging process) hydrogen causing IG fracture along the RHAGBs, a constant (throughout the deformation, as H is not redistributed) reduction in fracture energy along the RHAGBs predetermined prior to the onset of straining is assumed. Applying the same reduced fracture energy along

all the RHAGBs in samples S1-S3 closely mimicked the macroscopic tensile behavior and provided accurate predictions of the microscopic fracture evolution behavior. It is intriguing that, in the case of samples S1 and S2, the identical reduction in fracture energy was applied to all the available RHAGBs, yet fracture initiation and propagation were observed exclusively along specific RHAGBs, while others remained intact without any fracture. This phenomenon can be attributed to the fact that the total stored energy driving the fracture is strongly influenced by the deformation of grains adjacent to the GBs. The crack evolution in the used crystal plasticity phase-field fracture model is driven by the stored elastic and plastic energy. Since, fracture occurred after a certain amount of plastic strain, the plastic energy's contribution significantly outweighs that of elastic energy in driving the fracture process [177]. Consequently, fracture is primarily triggered by stored plastic energy, with elastic energy playing a negligible role in comparison. The primary role of plasticity in the implemented coupled framework is to induce work hardening, effectively elevating stored energy to be released during fracture. Given that the simulation results successfully reproduced the fracture at specific RHAGBs in a manner similar to the experiments and also nearly replicated the macroscopic strain levels for H-charged samples, the primary function of plasticity in generating critical stress levels at the grain boundaries through work hardening (influenced by adjacent grains) is duly confirmed. This process ultimately results in an escalation of the critical stored energy at the grain boundaries, which is subsequently released during the fracture process.

The simulated H-induced reduction in macroscopic strain levels is obtained after significantly reducing the fracture energy along the RHAGBs from 75 MPa in the uncharged case to 1.52 MPa in the H-charged case. It is still debatable if sufficient hydrogen at the GBs can reach by thermodynamic equilibrium to cause this much amount of reduction in the GB fracture energy promoting IG fracture. However, it is to be reminded that pertinent to the oligocrystal microstructure, all the fracturing GBs were in direct contact with the electrochemical charging medium containing recombination poison, a combination that can lead to a high H-concentration diffusion into materials [95]. Moreover, the RHAGBs are also potential sites for the impurities segregation other than H such as Oxygen, Phosphorus, and Sulfur [94, 95, 191]. These impurities segregated (other than hydrogen) to the RHAGBs can induce IG fracture independently and/or can modify the hydrogen-grain boundary interaction to promote the IG fracture [95, 102, 191]. The experimental investigations in previous chapters (Chapter 3 and Chapter 4) on identical oligocrystals showed IG cracking exclusively in the hydrogen-charged samples, indicating that IG fracture was primarily induced by hydrogen uptake rather than any other impurity segregation. However, it is important to acknowledge that the potential impact of these segregated impurities, even in trace amounts, on the kinetics of hydrogen trapping at the grain boundaries favorable for decohesion cannot be refuted.

Using positron annihilation, Lawrence et al. [85] presented evidence of the preferential formation of vacancies and their clusters, especially around the GBs. Moreover, authors reported that the plastic deformation of hydrogen-charged Ni-alloy resulted in the

generation of additional free volume and this mechanism was active even at the conditions when hydrogen is essentially immobile. The increasing density of such vacancy-type defects can gradually break the GB structural integrity, possibly making the final GB separation easier via the HEDE mechanism [100]. Therefore, the significant decrease in fracture energy noted at the RHAGBs in the hydrogen-charged samples can be ascribed to a confluence of factors, encompassing the thermodynamic segregation of H-concentrations, the presence of impurities other than H, and the accumulation of vacancies. However, the specific contributions of each of these mechanisms to the net decohesion effect in H-charged materials is a subject for future investigation.

5.5   Conclusions

This chapter involves the development and application of a coupled crystal plasticity-phase field fracture finite element model to comprehend the observed phenomena of ductile transgranular fracture and H-induced brittle intergranular fracture in the oligocrystal samples studied experimentally in Chapter 4. The developed framework is implemented in the commercial finite element package Abaqus using UMAT and UEL subroutines. With the aid of these simulation results, it is duly confirmed that the primary role of deformation during hydrogen-induced IG fracture in the investigated oligocrystals is to induce work hardening, effectively raising stress and stored energy levels to a critical threshold at the hydrogen-susceptible RHAGBs.

Chapter 6

Hydrogen Induced Blister Cracking and Mechanical Failure in Pipeline Steels

6.1 Introduction

American Petroleum Institute (API) 5L graded pipeline steels have been an efficient means for long-distance bulk transportation of hydrocarbons and natural gases [192]. The electrochemical evolution of hydrogen atoms; a byproduct of cathodic over-protection and other corrosion processes, make these pipeline steels prone to hydrogen-assisted degradation [27, 193]. Afterward the initial findings of Johnson [8], extensive research has been conducted to elucidate hydrogen-based degradation in steels. Similar to the other metallic materials, atomic hydrogen dissolved into pipeline steels leads to the deterioration of their overall mechanical properties (ductility, fracture toughness, fatigue life) by promoting a transition from ductile to brittle fracture [26, 194, 195, 196]. As also defined in the earlier chapters, this phenomenon of H-induced ductile to brittle failure transition is referred to as hydrogen embrittlement (HE) [197, 198, 199]. Hardie et al. [26] reported the HE in terms of a decrease in ductility and cross-sectional area of three different API pipeline steel grades. A linear decrease in fracture toughness with an increase in pre-recharged hydrogen concentration was observed by the Wang [194]. Chatzidouros et al. [200] also confirmed the reduction of fracture toughness under a hydrogen atmosphere. Moreover, a decrease in fatigue life and an increase in fatigue crack propagation rate in pipeline steels under hydrogen atmosphere have also been reported [195, 201, 202, 203]. Similarly to other materials, the impact of hydrogen on the mechanical properties of pipeline steels is typically explained by the HELP and/or HEDE mechanisms of hydrogen embrittlement.

However, one of the uncertainties associated with measuring and evaluating the hydrogen embrittlement (HE) sensitivity of pipeline steels is their high susceptibility to hydrogen-induced cracking (HIC) [27, 29, 30]. For pipeline steel materials, the ingress of hydrogen through either cathodic charging or exposure to a high-pressure hydrogen atmosphere can lead to the formation of cracks/blisters/bubbles on the surface of the sample, even in the absence of external mechanical loads [17, 204, 205, 206, 207, 208, 209, 210, 211]. The cracks and blisters that develop on the sample surface solely due

to hydrogen exposure, without the influence of external mechanical loads, are commonly referred to as hydrogen-induced cracks/blisters (HIC). As per the definition given by the National Association of Corrosion Engineers (NACE), the term hydrogen-induced (HIC) cracking covers the now obsolete terms of step-wise cracking, hydrogen-induced step-wise cracking, blister cracking, and hydrogen pressure cracking [17]. In pipeline steels, interfaces like grain boundaries, phase boundaries, and non-metallic inclusions-matrix interfaces act as strong traps for hydrogen [212]. At these interfaces, dissolved atomic hydrogen accumulates, recombines, and precipitates the gaseous hydrogen molecules when the hydrogen solubility limit of the material is reached. This precipitation creates an incipient crack/blister, and the growth of this crack/blister is propelled by the pressure of hydrogen gas trapped within it [17, 213, 206]. Blisters formation can be perceived if hydrogen pressure in the voids induces stress in excess to yield strength of material, and cracks can be perceived as a result of stress in excess to the force of atomic bonding [206, 207, 208, 209, 210, 211, 214]. Mohtadi-Bonab et al. [27] reported the MnS inclusions as the primary sites to crack initiation in pipeline steels. Xu et al. [28] supported the threatening role of mixed Al-Si-Mg-O inclusions to promote the HIC. Ren et al. [207, 208, 214] proposed a model of blistering due to superabundant vacancies that combine with hydrogen to generate hydrogen-vacancy clusters. These clusters expand further by diffusion of vacancies into them and become small pores. The recombination of hydrogen atoms in such cavities increases the gas pressure. Griesche et al. [215] strengthened these findings related to the blistering phenomenon in pure iron by 3D neutron tomography. The authors concluded that the existence of the second phase is not essential for blister formation as blisters were forming in the pure iron also. Moreover, multiple micron-sized pores situated at grain boundaries after hydrogen charging were concluded to be responsible for the blistering phenomenon. Grain boundaries are also considered potential sites for hydrogen-induced crack nucleation in pipeline steels. Grain boundaries play a dual role under the hydrogen atmosphere i.e. acts as faster hydrogen diffusion pathways as well as hydrogen traps. Hence, the microstructures with intermediate grain size are considered optimum against the hydrogen-induced cracking [212]. Refined equiaxed microstructures with minimum stored energy also offer potential resistance against HIC in pipeline steels [216]. Other than the grain boundary area fraction, the presence of different phases in the pipeline steels plays a more significant role in HIC behavior. Hydrogen-induced crack initiation and propagation along polygonal ferrite grains instead of acicular ferrite was observed by Dong et al. [30]. Dunne et al. [204] observed that hydrogen trapping in pipeline steels decreases in the order of banded ferrite-pearlite, equiaxed ferrite-pearlite, ferrite-granular bainite, and bainite-ferrite, which indicates the varying degree of cracking tendency among different microstructures. Martensite/Austenite (M/A) islands are reported to be the most threatening for HIC nucleation [29].

6.1.1 Difference between the HIC and HE

HIC and HE are fundamentally different forms by which hydrogen can cause degradation of materials, but their potential confusion arises from the ambiguous naming conventions frequently employed in the literature [17, 193]. The process of HE, in general, requires an applied force and does not generally have hydrogen gas precipitation within the material. Moreover, HE affects various classes of metals, whereas hydrogen-induced cracking (HIC) is primarily a concern in non-austenitic steels [5, 17]. Other metals/alloys typically do not exhibit HIC unless they are exposed to extremely aggressive electrochemical hydrogen charging. Unlike the HE effect, where materials may still perform in a ductile manner once hydrogen is removed, hydrogen-induced cracking (HIC) is irreversible. In HIC, cracks or blisters, once formed, will remain there even after the removal of hydrogen from the material.

6.1.2 Integration of HIC and HE

As discussed above there is numerous work conducted so far to study the phenomenon of HIC and HE in literature. In the controlled laboratory environment, when conducting studies primarily focused on hydrogen embrittlement (HE), researchers typically design hydrogen charging conditions to avoid the development of hydrogen-induced cracking (HIC). However, it's essential to highlight that real service conditions for pipeline steels can give rise to both of these phenomena. Moreover, it is often the synergistic interaction of hydrogen-induced cracking (HIC) and hydrogen embrittlement (HE) that must prevail to govern the overall structural integrity of the materials. It is important to acknowledge, that HE likely plays a crucial role in the HIC process. Conversely, gaseous hydrogen-induced cracks and blisters (HIC) are likely to impact the material's response in the surrounding area during mechanical loading.

For economical transportation through these pipelines, it is essential for the pipelines to have large diameters and work under high internal pressures to avoid the use of thick wall pipelines to decrease the overall project expenditure. As a result, these pipelines are subjected to both tensile and fatigue loading. Fatigue cracks usually initiate at the specimen surface by stress concentration that gives rise to localized irreversible plastic deformation even at a stress level much lower than macroscopic uniaxial yield strength. Local stress concentration on the surface can be caused due to variety of microstructural in-homogeneities (such as different phases, nonmetallic inclusions, precipitates, grain or phase boundaries, and triple junctions) as well as non-microstructural in-homogeneities (such as surface roughness, notches, persistent slip bands during fatigue loading) [217, 218, 219, 220]. A critical combination of stress concentration and hydrogen content in the hydrogen atmosphere further intensifies this localized micro-plastic fatigue damage by activating hydrogen concentration-dependent different HE mechanisms. Total fatigue life can be divided into crack initiation and growth stages. The crack initiation stage is linked with crack nucleation and short crack propagation until the crack length reaches a limit

detectable by non-destructive testing (NDT) methods [221]. Pearson [222] observed that short fatigue cracks initiated either from the microstructural inhomogeneity or from the external notches show enormously fast propagation even at lower threshold stress intensity factor than customarily scrutinized LEFM (linear elastic fracture mechanics) based long fatigue cracks. Typical significance of studying the short fatigue crack over LEFM-based long fatigue crack is well established [221, 222, 223, 224]. Recent investigations reported a significant effect of hydrogen to intensify the propagation rate of short fatigue cracks due to the coexistence of more than one HE mechanism; primarily HELP and/or HEDE [225, 226].

It is important to note that, much like short fatigue cracks, HIC is also a phenomenon that predominantly occurs near the surface of the material. Besides the extensive research on the hydrogen effect during mechanical loading, the role of hydrogen-induced near-surface defects formed during H-charging prior to the mechanical loading (i.e. HIC) on mechanical properties with special emphasis on short fatigue crack behavior has not been considered significantly. The present work aims to highlight the critical nature of these hydrogen-induced blister cracking on the mechanical property degradation of API 5L X65 steel. In this chapter, firstly, the role of microstructural constituents in hydrogen-induced cracking and blister (HIC) formation is discussed. Subsequently, H-charged tensile specimens containing the blisters and cracks (formed during H-charging) are subjected to the slow strain rate tensile (SSRT) tests. Finally, a short fatigue crack growth framework is used to highlight the critical influence of hydrogen-induced blisters on the fatigue crack growth rate.

6.2 Experimental procedure

6.2.1 Material and microstructure

High strength low alloy API X65 steel plates (with chemical composition as shown in Table 6.1) processed via thin slab casting and rolling facility was used in this study. To examine the microstructural details, specimens were polished sequentially to 2000 grit size SiC abrasive papers followed by cloth polishing with diamond paste of size 1 μm. To reveal the microstructural constituents present in the material, an etchant containing 2 % Nital solution was used. In order to confirm the presence of M/A constituents, two-stage tint etching i.e. etching with LePera reagent (for 25 seconds) followed by electro-polishing (at 5 V for 120 seconds) in a solution of distilled water (100 ml), NaOH (25 g), and picric acid (5 g) was employed. After this tint etching, optical microscopy reveals M/A as white, carbides as black, and ferrite matrix appears lighter than the carbides but darker than the M/A constituents [200].

Table 6.1: Chemical composition of investigated API 5L X65 steel.

Element	C	S	P	Mn	Si	Mo	Al	V	Nb	Fe
X65	0.054	0.001	0.012	1.498	0.230	0.086	0.029	0.0355	0.0572	Balance

6.2.2   Hydrogen charging

The hydrogen atmosphere was simulated by exposing the specimens electrochemically to an electrolyte containing 1N H_2SO_4 solution along with 1.4 g/L Thiourea (as recombination poison) under a constant current density of 20 mA/cm^2 for a period of 4 hours. Before hydrogen charging, samples were polished similarly as explained in the previous section. Specimen as cathode and platinum mesh as anode were maintained during hydrogen charging. Post hydrogen charging, samples were re-polished with diamond paste for two minutes and then were investigated in the optical microscope and SEM (scanning electron microscope; JEOL; JSM-6610) to check specimen status against hydrogen-induced cracks/blisters formation due to hydrogen charging. Japanese Industrial Standard (JIS) Z 3113 test procedure was used to quantify the content of diffusible hydrogen after hydrogen pre-charging [227]. An average hydrogen content of 5.4 wppm was quantified with this method.

6.2.3   Tensile and fatigue experimentation

To evaluate the HE susceptibility of the investigated material, a room temperature SSRT test at a strain rate of $5 \times 10^{-5} s^{-1}$ was conducted on the tensile specimen with 4 mm thickness and 25 mm gauge length (see Fig. 6.1a). SSRT was conducted in both uncharged and hydrogen-charged conditions. For hydrogen-charged conditions, a tensile specimen undergoes the SSRT test immediately after the hydrogen charging. The Hydrogen embrittlement index (HEI) i.e. a quantitative measure of HE susceptibility was computed as:-

$$HEI(\%) = \frac{(R_A - R_H)}{R_A} \times 100\% \tag{6.1}$$

Here, R_A and R_H are the reductions in the cross-sectional area after the fracture of uncharged and hydrogen-charged specimens respectively.

To reveal the hydrogen influence on fatigue crack, in-situ investigations of short fatigue crack growth on single edge notch tension (SENT) specimen (see Fig. 6.1b) with an initial notch size of ~ 50 μm were conducted using digital microscope (Dino-lite; AM73915MZT). For hydrogen-charged condition, the SENT specimen was subjected to fatigue loading immediately after hydrogen charging. Fatigue experiments were performed with stress range ($\Delta\sigma$), R-ratio, and frequency of 315 MPa, 0.1 and 35 Hz respectively in both hydrogen-charged and uncharged conditions. The fatigue tests were interrupted at regular intervals (in terms of the number of cycles) to take images so as to track the crack path ahead of the notch after each interval. The process of image capturing led to a break of 15 seconds after regular intervals to otherwise continuous fatigue loading experiment. The post-processing of these images provided the data regarding crack length (a) corresponding to a particular number of cycles (N). Secant method as per ASTM standard E647-11 was used to calculate crack growth rate (da/dN) as:
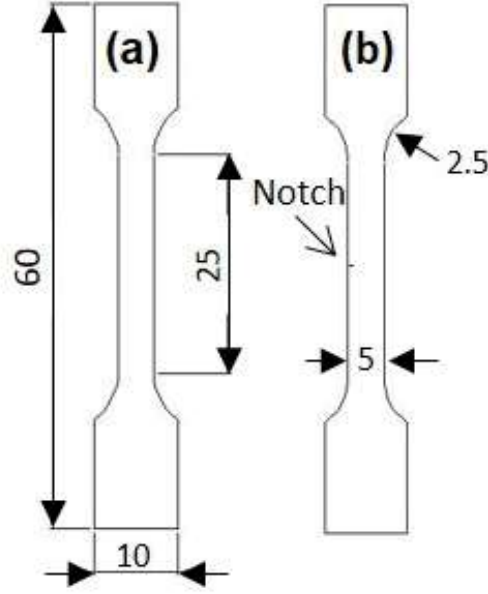
Figure 6.1: (a) Specimen configurations used for tensile testing and (b) specimen to track short fatigue crack propagation ahead of notch (all dimensions are in mm)

$$\frac{da}{dN} = \frac{a_{i+1} - a_i}{N_{i+1} - N_i} \tag{6.2}$$

where, $(a_{i+1}a_i)$ is the increment in crack length after $(N_{i+1}N_i)$ increment in loading cycles. Once the crack grows up to a predefined crack length i.e. ~ 500 µm, the test is stopped. Thereafter the fatigue-tested specimens were etched and were further investigated in SEM and EDS (energy dispersive X-ray spectroscopy) to extract the microstructural sensitive convoluted details.

6.3 Results and discussion

6.3.1 Starting microstructure

Figure 6.2 presents the optical and SEM images of X65 steel microstructure composed of ferrite (white in Fig. 6.2a) and heterogeneously distributed pearlite (see Fig. 6.2c and 6.2d). Islands/stringers situated at the grain boundaries were confirmed using tint etching as M/A phase (white color in Fig. 6.2b). Random distributions of incoherent inclusions enriched in oxides of Al and/or Si were also observed in the parent matrix. The average grain size of ~ 10 μm was recorded by using the linear intercept method.

6.3.2 Effect of electrochemical hydrogen charging

Electrochemical hydrogen charging resulted in multiple surface cracks and blisters formation as shown in Fig. 6.3. Blisters of nearly circular/oval shape with a maximum longitudinal dimension of ~ 500 μm were found mixed in a dome shape and plateau-like
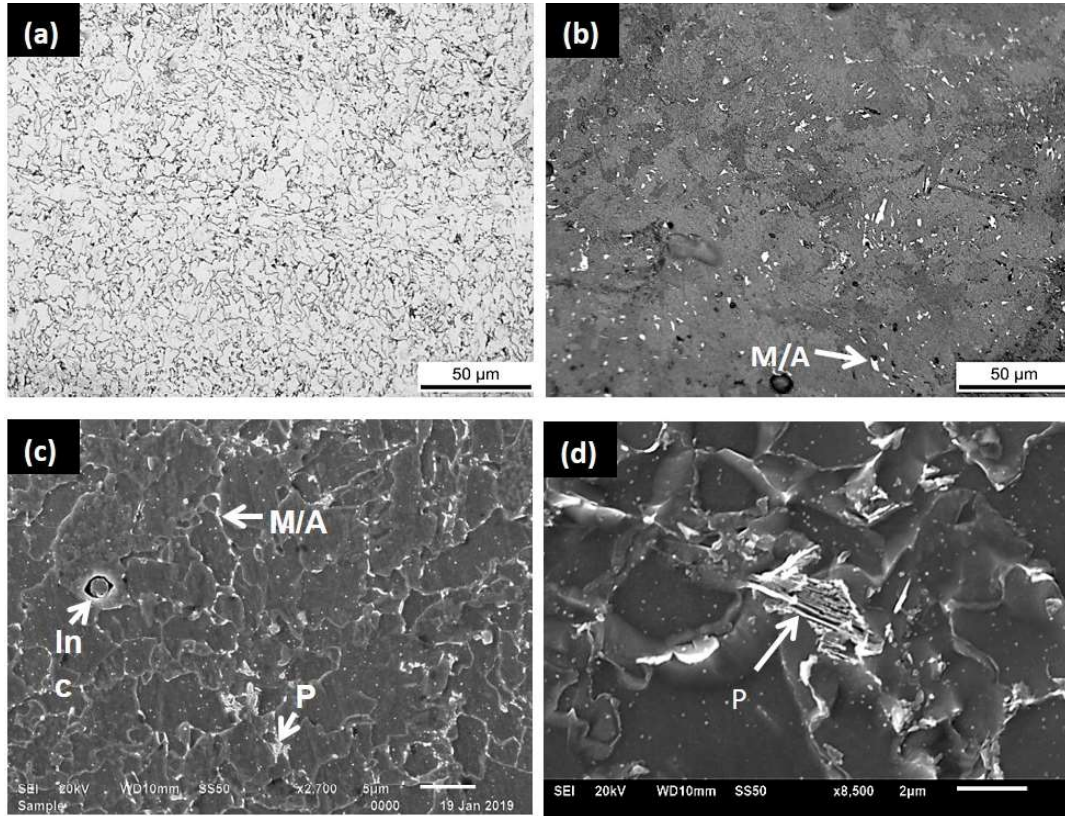
Figure 6.2: Starting microstructure of investigated X65 steel, (a) optical image after Nital etching; (b) optical image after tint etching; (c) and (d) are low and high magnification SEM images after Nital etching. P: Pearlite, M/A: Martensite/Austenite, Inc: Inclusion

elevations emerging from the surface. A large variation in the blister size can be observed in Fig. 6.3a. Nearly all the blisters were accompanied by the cracks on their wall i.e. blister wall cracks (BWC) as shown in Fig. 6.3b. Cracking along the blister wall i.e. BWC is facilitated primarily by the inclusions. EDS analysis confirmed these inclusions enriched with oxides of Al and Si (Fig. 6.4a). Besides the blister wall cracking, these inclusions also promoted the formation of the cracks (see Fig. 6.4b). Hard, brittle, and incoherent Al-Si-O inclusion interfaces act as irreversible hydrogen trapping sites. The recombination of hydrogen atoms forms hydrogen molecules at these trapping sites and leads to pressure rise. This pressure rises when exceeds a critical value, and cracking initiates [212, 28]. Observations regarding the role of mixed inclusions of Al-Si-O on hydrogen-induced cracking are consistent with previously reported results [28, 228].

Mohtadi-Bonab et al. [27] reported oxides inclusions as insignificant to HIC; whereas MnS inclusions were reported to be the most threatening to HIC. It is important to discuss here, that no traces of MnS type of inclusions are observed in the present work. The absence of MnS type inclusions is due to the sufficiently low content of Sulfur i.e. 0.001 % in the investigated material [28]. Ghosh et al. [212] summarized the control of Sulfur content ($\sim$ 0.001 %) as a necessary condition but not the sufficient one to control HIC in pipeline steels, as HIC can be caused by other than MnS type of inclusions also. The threatening role of
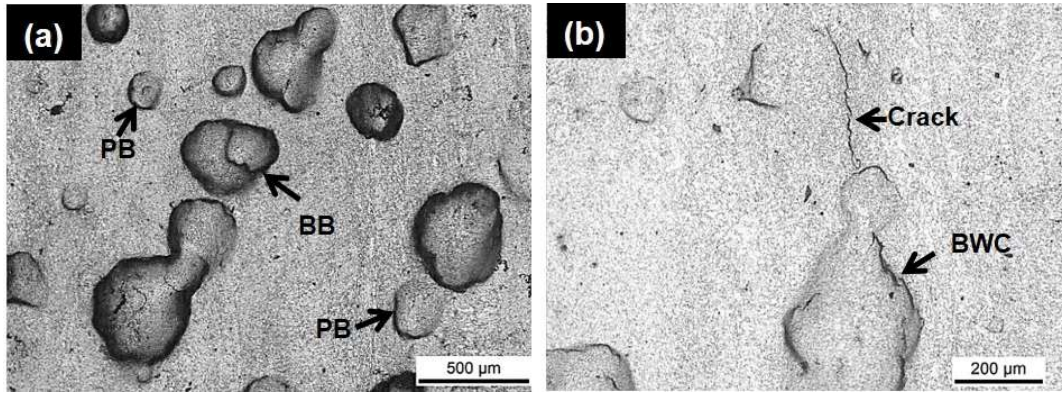
Figure 6.3: (a) Blister formation after hydrogen charging and (b) hydrogen induced surface cracks and blister wall cracking. BB: Blister on blister, PB: Plateau-like blisters, BWC: Blister wall cracking

mixed Al-Si-O inclusions in the absence of MnS inclusions observed in the present work confirms that other than control of sulfur content, proper thermo-mechanical processing routes and alloying addition to avoid the oxide inclusions are also mandatory to improve the resistance of pipeline steels against HIC.
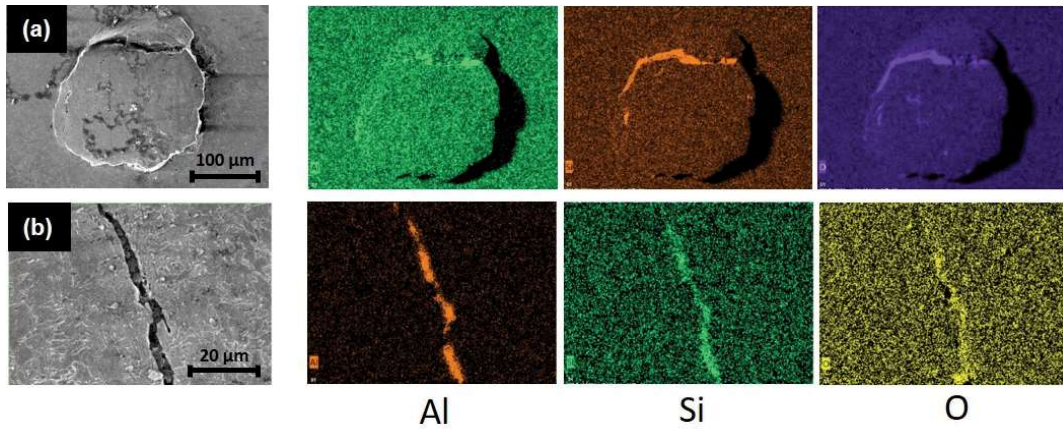
Figure 6.4: (a) Blister wall cracking and (b) hydrogen-induced surface crack along the Al-Si-O inclusions

M/A stringers situated at the grain boundaries also promoted hydrogen-induced cracking. Figure 6.5 clearly demonstrates hydrogen-induced cracking along M/A stringer and following grain boundaries on both sides. A relatively high concentration of hydrogen trapped at the M/A interfaces is the prime reason to promote HIC. A similar observation regarding the role of M/A stringers on HIC is reported by Park et al. [29]. Interestingly, no relevance of the pearlite/pearlite-ferrite interface is found to facilitate HIC and blister wall cracking in this work. This was suspected as a consequence of the lesser amount of pearlite and that too nearly equiaxed in shape, available in the microstructure.
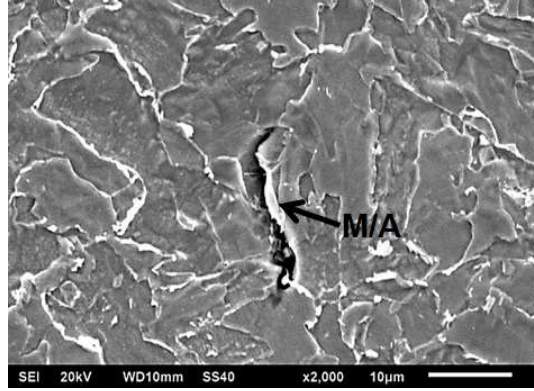
Figure 6.5: Hydrogen induced cracking along M/A stringer

6.3.3 Slow strain rate tensile (SSRT) test

Figure 6.6 shows SSRT curves obtained at room temperature for uncharged and hydrogen-charged X65 steels. Hydrogen-induced macroscopic hardening i.e. an increase in yield strength after hydrogen charging is observed. This is attributed to the pinning effect of hydrogen atmosphere to the dislocations and/or impediment of moving dislocations to cross slip as reported by Oriani and Josephic [229] and also by Wu and Kim [230] in similar low alloy steels. Relatively insignificant difference in ultimate tensile strength is observed in both conditions. However, hydrogen charging caused 16 % loss in fracture elongation (decrease in total elongation from 25 % in uncharged condition to 21 % in hydrogen charged conditions, see Fig. 6.6). HEI calculated by using equation (1) for the current material was 39 %. Kong et al. [231] indicated that the value of HEI more than 35 % is an indication of high HE susceptibility of material with brittle fracture. However, Zhang et al., [232] reported that the HE susceptibility in pipeline steels must be determined based on the fracture surface behavior rather than the empirical value of HEI alone. Hence to investigate the HE susceptibility, fractographic analysis of SSRT fractured specimens (see Fig. 6.7) is conducted. High magnification revealed deep dimple-like fracture morphology occurred by microvoids coalescence (MVC) throughout the cross-section of the uncharged specimen (Fig. 6.7b). However, the hydrogen-charged specimen is accompanied by the quasi-cleavage type fracture near the surface (Fig. 6.7e) but dimple dimple-dominated fracture at the center (Fig. 6.7d). This difference in fracture behavior of hydrogen charged specimen at the center and near to surface is due to the inhomogeneous hydrogen distribution throughout the cross-section. A combination of hydrogen charging parameters and specimen thickness employed in the present work resulted in high hydrogen concentration near the surface, however, hydrogen might have not diffused in sufficiently high amounts to the middle of the specimen. Careful investigation of the middle part of both uncharged (Fig. 6.7b) and charged specimens (Fig. 6.7d) reveals that other than conventional ductile dimples caused by microvoid coalescence, additional very fine microvoids with relatively poor defined dimples (marked with white arrows in Fig. 6.7d) are present in hydrogen charged specimen. This locally ductile fine microvoid fracture

feature is consistent with the HELP mechanism of HE as reported by Robertson et al. [5]. Moreover, Djukic et al. [16] reported a similar fracture feature (as in Fig. 6.4d) and supported that at low hydrogen concentration HELP mechanism was dominant, which was manifested by an increase in locally ductile fine microvoids fracture features as observed in the present work in the middle of the hydrogen charged specimen.
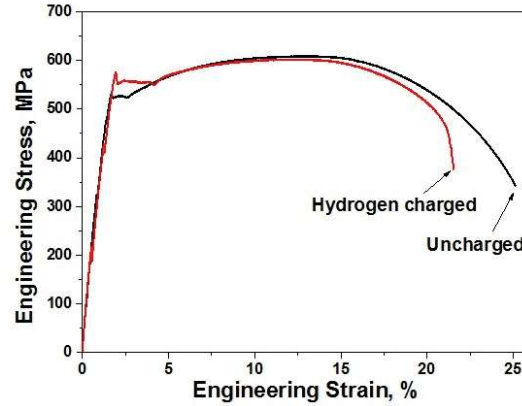
Figure 6.6: Tensile curves obtained from SSRT for uncharged and hydrogen charged samples

The edges of the specimen were under a high concentration of hydrogen; here HELP HELP-promoted microvoids are followed by a high concentration of hydrogen diffusion into these microvoids. Due to this high hydrogen concentration in these microvoids, the cohesive strength of the material gets reduced and thus assists in easy decohesion via the HEDE mechanism. Quasi cleavages with nearly flat dimples (see Fig. 6.7e) support this synergy of HELP and HEDE mechanism under high hydrogen concentration at the edges. Locations marked with arrows in Fig. 6.7c show the blister's decohesion from the material matrix during tensile loading. One such location (marked as 'f' in Fig. 6.7c) is magnified in Fig. 6.7f. Blister crack growth is a discontinuous process i.e. critical pressure buildup at the trapping site leads blister crack to grow; growth halts every time the pressure decreases below the critical value until diffusion allows enough accumulation of molecular hydrogen to continue crack growth [233]. The same can be perceived from the fracture morphology shown in Fig. 6.7f, containing quasi-cleavage dominated regions consistent with discontinued advancement of blister crack front due to cyclic pressure build-up. Hydrogen-induced cracks and blisters (formed due to hydrogen charging and without any external loading) are near-surface phenomena and their effect is generally been ignored during the tensile testing. Easy decohesion of hydrogen blister walls from the matrix and multiple cracks as a result of hydrogen charging (without any external load) can result in a reduction of effective area sustaining the load during tensile testing. This reduction in the effective area will lead to the localization of strain due to stress concentration in these areas. Koyama et al. [234] conducted the 2D digital image correlation (DIC) of dual-phase steels and reported that the local plastic strain for both the charged and uncharged specimen was almost identical except for the necking region. From this, the authors concluded that

hydrogen does not affect in the uniform elongation regime but causes the ductility to deteriorate mainly in the post-necking regime. A similar observation can be made from Fig. 6.6 showing uniform elongation but a reduction in fracture elongation after hydrogen charging in comparison to the uncharged specimen. This means that HE mechanisms get intensified due to local straining during necking. Hence, it can be concluded that the localization of strain promoted by blister decohesion can also significantly affect the tensile properties of the investigated steel. While a direct quantitative measure of the potential loss in tensile properties caused by blisters cannot be presented here, one cannot disregard the role that these H-charging-induced blisters and cracks play in affecting mechanical properties.

6.3.4   Short fatigue crack propagation

In both, hydrogen-charged and uncharged specimen cracks initiated from the notch. Hydrogen charging resulted in early initiation of crack from the notch i.e. only 77000 cycles were consumed for the crack initiation after hydrogen charging in comparison to 109500 cycles in the uncharged specimen. Hydrostatic stresses ahead of the crack tip due to external loading resulted in nearby hydrogen ions diffusing towards the crack tip and increasing the local hydrogen concentration ahead of the crack tip. This synergetic action of stresses and high concentration of hydrogen ahead of the notch decreased the notch strength and caused easy crack initiation during cyclic loading of hydrogen-charged specimen [196]. Figure 6.8 presents in-situ optical images of short fatigue crack propagation ahead of the notch in uncharged and hydrogen-charged specimens. In comparison to the uncharged specimen (Fig. 6.8(a-c)), dramatically different behavior of crack propagation ahead of the notch after hydrogen charging can be observed in Fig. 6.8(d-f). Other than the microstructure based hydrogen influenced short fatigue crack propagation (that will be described later in this section), the coalescence of the fatigue crack with one already existing on the blister wall (see Fig. 6.8(d-f)) is found to alter the propagation path and rate significantly.

To quantify the influence of the hydrogen atmosphere on the fatigue crack propagation rate, the number of cycles (N) and corresponding equivalent crack length (a) for the charged and uncharged specimens were recorded at regular intervals during in-situ fatigue testing. Here, the term "equivalent crack length" signifies the largest crack in the area i.e. longest crack made after the coalescence [235]. Figure 6.9a shows the variation of equivalent crack length 'a' with the corresponding number of cycles 'N' for both uncharged and charged specimens. An abruptly unstable crack propagation (between marked arrows in Fig. 6.9a and marked as BWC in Fig. 6.9b) in hydrogen-charged specimen corresponds to the rapid increase in crack length due to the coalescence of fatigue crack with hydrogen-induced blister wall crack.

Moreover, other than the coalescence, the short fatigue crack is found to propagate faster in hydrogen-charged specimens in comparison to the uncharged specimen. Increased propagation rate of short fatigue cracks under hydrogen atmosphere without any blister
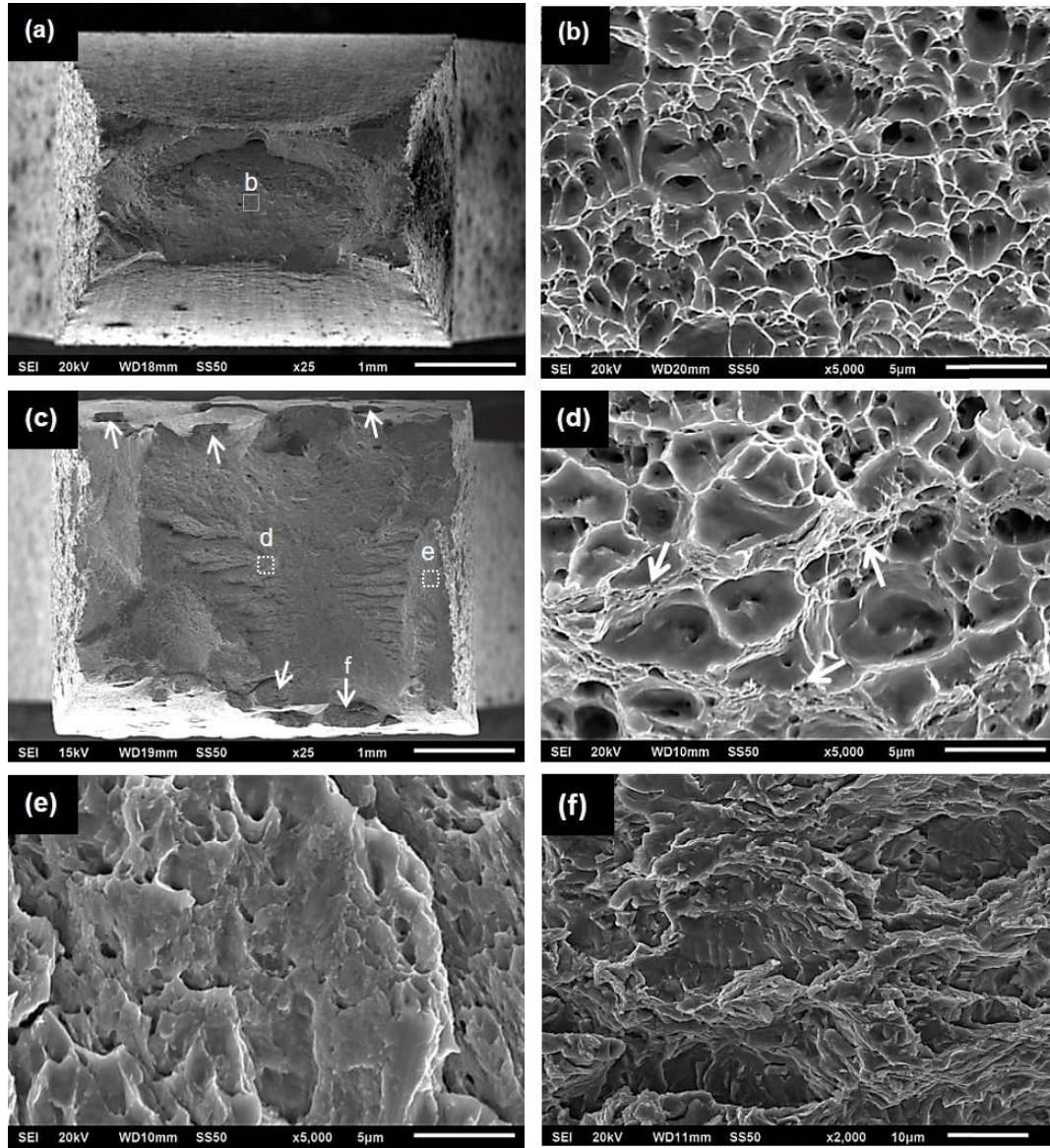
Figure 6.7: Fracture surface of (a) uncharged sample; (b) magnified image of marked location 'b' in fig. (a); (c) fracture surface of hydrogen charged specimen; (d), (e) magnified images of marked location 'd and e' in fig. (c); and (f) fracture analysis at one of the blister i.e. location 'f' in fig. c

or hydrogen-induced surface defect can also be inferred from our previously published work [236]. This fast propagation of fatigue crack in hydrogen charged specimen than in uncharged specimen (Fig. 6.9a) confirms lesser hindrances by microstructural features under hydrogen atmosphere [225, 226, 236]. The same can be observed from the lesser dips/decelerations after hydrogen charging from Fig. 6.9b in comparison to the uncharged specimen. SEM analysis revealed predominantly slip-mediated transgranular crack propagation (Fig. 6.10a) in the uncharged specimen. Arrows marked in Fig. 6.10a show the role of pearlite interface and directional M/A stringers in easy crack propagation in the uncharged specimen. Crack propagation in hydrogen charged specimen is mixed
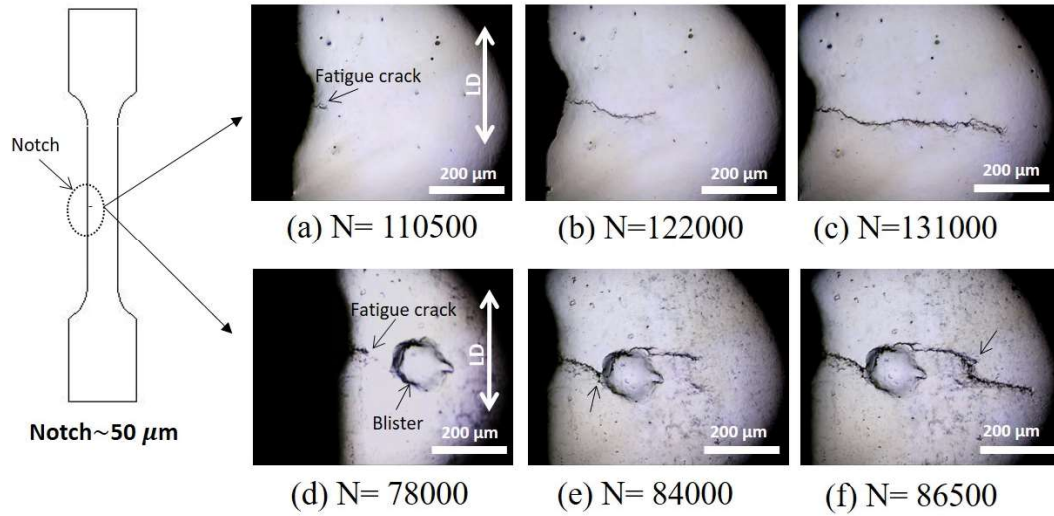
Figure 6.8: Digital microscopic images of intermediate stages of crack propagation in (a-c) uncharged and (d-f) hydrogen charged specimen. LD: loading direction
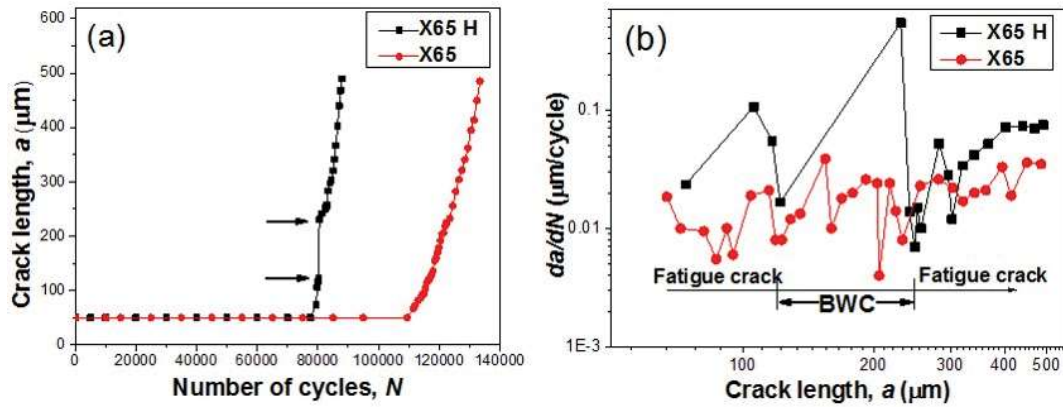
Figure 6.9: Variation of (a) short fatigue crack length 'a' with numbers of cycles 'N' and (b) crack growth rate 'da/dN' with crack length 'a'. H: Hydrogen charged

in inter and transgranular. Figure 6.10(b-d) presents the SEM images of the crack path in hydrogen charged specimen corresponding to the marked locations in Fig. 6.8e and f. Figure 6.10b is the SEM image of hydrogen charged fatigue tested specimen near to the location marked by the arrow in Fig. 6.8e. Dotted black arrow in Fig. 6.10b presents the point of coalescence between the propagating fatigue crack and an already existing crack on the blister wall.

An important role of M/A islands and inclusions to alter the fatigue crack propagation path and hence to promote intergranular propagation under the hydrogen atmosphere can be observed in Fig. 6.10c. Figure 6.10d is the SEM image that corresponds to the location marked with an arrow in Fig. 6.8f and shows the easy decohesion along the interface of inclusions (marked with arrows) that altered the propagation path significantly and accelerated the fatigue crack propagation rate. EDS mapping confirmed the inclusions mixed in Al-Si-O. From the above observations, it is concluded that the cracking along
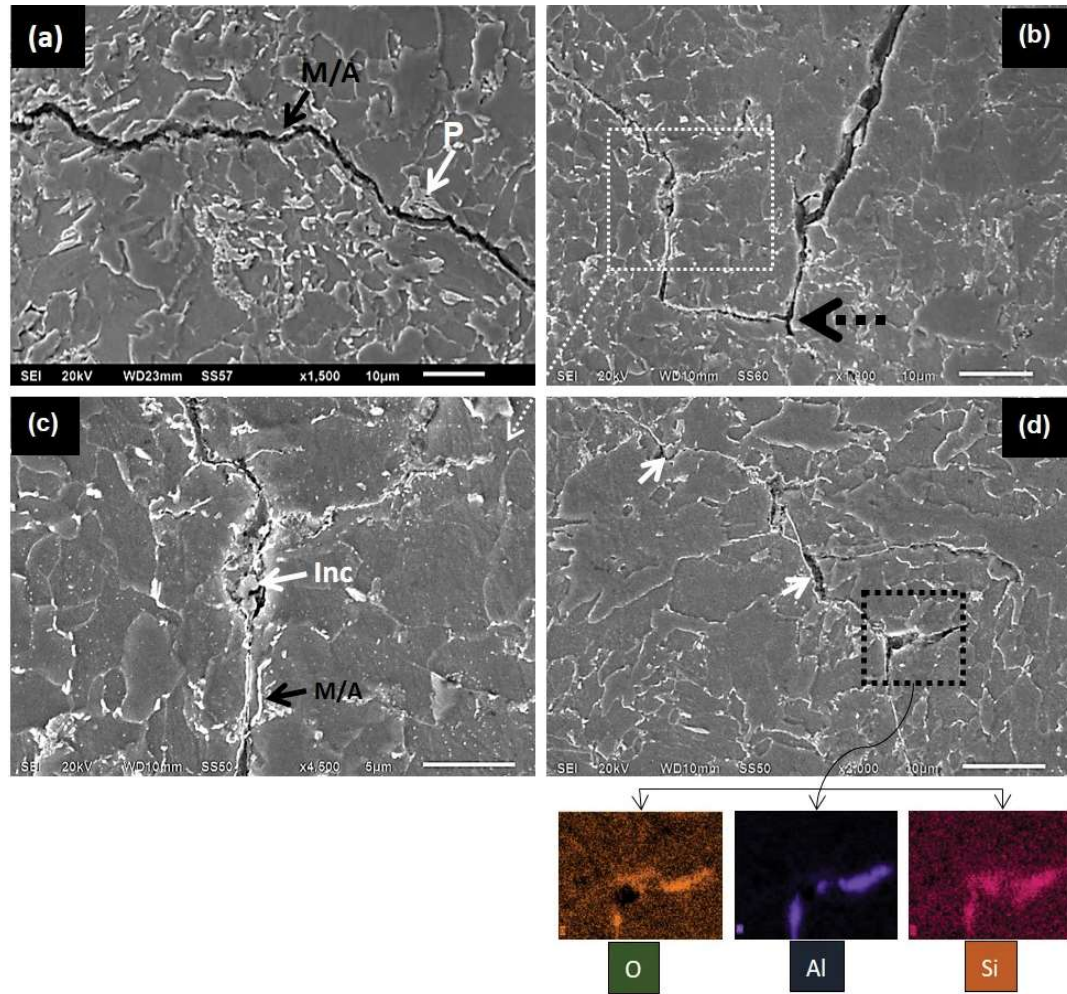
Figure 6.10: SEM image of fatigue crack path ahead of the notch in (a) uncharged specimen; (b)–(d) hydrogen charged specimen. P: Pearlite, M/A: Martensite/Austenite, Inc: Inclusion

the inclusion interface is more sensitive to the hydrogen while the crack in the M/A interface also contributes significantly to the fast propagation rate. Figure 6.11 presents the fracture surfaces observed after fatigue testing of uncharged and hydrogen-charged specimens. In the case of the uncharged specimen, the fracture surface is characterized with typical fatigue ductile striations (indicated by arrows in Fig. 6.11a). The fractographic analysis is consistent with the observed plasticity-driven slip-mediated transgranular crack propagation in the uncharged specimen. In the case of hydrogen charged specimen, the fatigue-fracture surface exhibited a dominated flat quasi-cleavage type fracture. At a few locations, these flat fracture surfaces are covered by some wider brittle-like striations (indicated by arrows in Fig. 6.11b); a typical signature of hydrogen-enhanced crack propagation in such steels [201].

Rios et al., [237] reported reduced frictional stresses along the active slip plane and weakening of microstructural barriers under hydrogen atmosphere as two major factors to promote short fatigue crack propagation. Schippl et al. [226] while investigating the
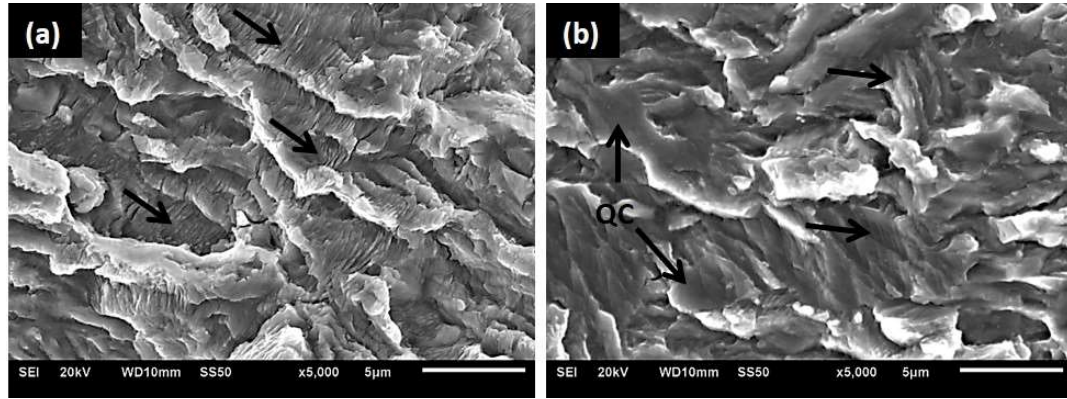
Figure 6.11: Fatigue fracture surfaces of (a) uncharged and (b) hydrogen charged X65 steel. QC: Quasi cleavage

short fatigue crack growth in metastable austenitic stainless steel reported that hydrogen pre-charging enhances localized irreversible plastic deformations at the crack tip which is consistent with the hydrogen-enhanced localized plasticity (HELP) mechanism. Other than the hydrogen-enhanced localized irreversible deformation, authors also supported the hydrogen-promoted easy grain boundary cracking which can be easily explained by the HEDE mechanism. Singh et al. [225] also reported the combined HELP and HEDE mechanism as a driving force to accelerate the short fatigue crack propagation under the hydrogen atmosphere. Authors also confirmed the weak resistance offered by the grain boundaries and microstructural features under hydrogen atmosphere in comparison to uncharged specimens similar to the Rios et al. [237] and Schippl et al. [226]. Similarly in the present work, the weakening of microstructural barriers against short fatigue crack propagation under hydrogen atmosphere was confirmed by lesser decelerations or dips in comparison to the uncharged specimen (see Fig. 6.9b). Moreover, easy decohesion at the interfaces of M/A stringers and inclusions due to the trapped hydrogen promoted intergranular fast fatigue crack propagation. Additionally, the coalescence of propagating fatigue crack with the hydrogen-induced blister cracking is shown to be an important feature to assist in easy crack propagation to the equivalent length and hence to promote overall crack propagation rate significantly.

6.4 Conclusions

This study evaluated the integration of HE and HIC phenomenon toward the mechanical properties degradation of X65 grade pipeline steel. Electrochemical hydrogen charging resulted in multiple surface cracks and blister formations. Inclusions mixed in Al-Si-O appear to be the most potential sites for the formation of hydrogen-induced cracks and blisters during H-charging (before any external loading). SSRT test accompanied by fractographic investigations confirmed HELP and HEDE dominated HE mechanisms at low and high concentrations of hydrogen respectively. Moreover, it is found that the easy decohesion of blisters during tensile testing can cause localized stress concentration

to promote HE during SSRT. Through short fatigue crack propagation, it is found that the presence of hydrogen reduced the number of cycles for initiation of the crack and accelerated the crack growth rate. Easy decohesion along the inclusions and M/A stringers facilitated the faster short fatigue crack propagation under the hydrogen atmosphere. Furthermore, the coalescence of short fatigue crack with the BWC resulted in a rapid increase in the crack length and significantly reduced the number of cycles for propagation to the equivalent crack length.

Chapter 7

Summary and Future Scope

7.1 Summary

The complex interplay between small hydrogen atoms and the intricate microstructural features of metallic materials presents formidable challenges in accurately characterizing the site-specific presence of hydrogen. Consequently, comprehending the activated micro-mechanisms contributing to the overall loss of structural integrity in metals and alloys under a hydrogen atmosphere becomes an exceptionally intricate endeavor. The presented work seeks to advance the understanding of hydrogen-assisted material degradation, which has wide-ranging implications for various engineering applications and material design. In the current work, the micro-mechanical aspects responsible for hydrogen-assisted damage in metallic materials are investigated by the utilization of novel numerical modeling and experimental strategies.

In the first objective of the present work (Chapter 2), a numerical framework to investigate the hydrogen-assisted deformation and failure scenarios emanating from the hydrogen-dislocation interaction under the proposition of the HELP mechanism of HE is developed. In this numerical framework, the dislocation density-based crystal plasticity model is coupled with a slip rate-based hydrogen diffusion/trapping model to simulate the two-way effect. In the two-way effect, while hydrostatic stresses and dislocation density affect the hydrogen redistribution; hydrogen trapped at the dislocations affects the associated critical stresses, interaction strength of dislocations on various slip systems, and multiplication/annihilation behavior of dislocations. The developed modeling framework is implemented using UMAT and UMATHT subroutines in commercial finite element solver Abaqus. The simulation results reveal that for nickel material containing weak dislocation-type traps, as investigated in this work, hydrogen distribution primarily depends on the distribution of hydrostatic stress. Additionally, the early-stage deformations simulated here validate the hydrogen-induced modifications in dislocation structures observed experimentally in single crystal and polycrystalline nickel. Furthermore, the simulation results demonstrate that the HELP mechanism can induce macroscopic softening and/or hardening due to a trade-off between the hydrogen-induced weakening of dislocation interactions and the increase in dislocation density caused by hydrogen. This chapter highlights the role of the HELP mechanism and suggests the possibility of additional mechanisms, such as HEDE, being required to explain early failures of Nickel material under a hydrogen atmosphere.

In the second objective, an oligocrystal approach is employed for the first time

to investigate the impact of hydrogen on the transition in fracture mode, shifting from ductile transgranular to brittle intergranular. In this objective, experimentation (Chapter 3 and Chapter 4) and numerical modeling (Chapter 5) are employed to investigate the HE-induced IG fracture of commercially available pure nickel (Nickel-201). In experimentation, different types of oligocrystals (i.e. True-oligocrystals, Quasi-oligocrystals, Identical-oligocrystals, and Bi-crystals) encompassing different types of microstructures (in terms of grains and grain boundaries) are developed by the combination of heat treatment and slicing method. These oligocrystal tensile samples in uncharged and H-charged conditions are then deformed at variable strain rates. In the second part of this objective, a finite element framework comprising a Crystal Plasticity-Phase Field Fracture model is used to simulate the macroscopic tensile response and corresponding microscopic fracture evolution behavior for uncharged and H-charged oligocrystals. This coupled modeling framework is implemented in Abaqus using the UMAT and UEL subroutines. This study emphasized the substantial impact of microstructure on susceptibility to hydrogen embrittlement. Specifically, it was observed that low-angle grain boundaries (LAGBs) and CSL (Coincident Site Lattice) $\Sigma 3$ grain boundaries exhibit resistance to hydrogen embrittlement, whereas random high-angle grain boundaries (RHAGBs) were found to be the most susceptible sites to hydrogen embrittlement. Moreover, the experimental results highlighted that the dynamic hydrogen redistribution (driven by stresses and mobile dislocations) and HELP-mediated localized accelerated dislocation activities are not necessary factors in causing IG fracture for the observed oligocrystals. In this study, the experimental results, corroborated by numerical simulations, suggest that intergranular (IG) fracture in hydrogen-charged oligocrystals results from the hydrogen trapped thermo-dynamically prior to deformation, which causes a significant reduction in fracture energy exclusively at the RHAGBs. Furthermore, the results provided validation that the primary function of plasticity prior to hydrogen-induced intergranular (IG) fracture is to induce work hardening, effectively increasing stress and stored energy levels to a critical threshold at the hydrogen-susceptible random high-angle grain boundaries (RHAGBs).

The third objective (Chapter 6) of this thesis work is dedicated to investigating the H-assisted degradation of pipeline steels. In addition to the complex multi-phase microstructure, one of the uncertainties associated with analyzing the H-assisted damage of pipeline steel material is its high susceptibility to hydrogen-induced cracking (HIC) in addition to hydrogen embrittlement. To comprehend the micro-mechanics of H-assisted damage in X65 grade pipeline steels, this work investigates the effect of hydrogen by using tensile testing and a short fatigue crack growth framework. Tensile test accompanied by fractographic evidence confirmed HELP and HEDE-dominated HE mechanisms at regions dominated by low and high concentrations of hydrogen, respectively. Furthermore, the easy decohesion of blisters (formed during H-charging) during tensile testing is expected to result in localized stress concentration, thereby promoting the activation of hydrogen embrittlement (HE) during tensile deformation. Through a short fatigue crack framework,

it is found that the presence of hydrogen in microstructure not only reduces the number of cycles for crack initiation but also accelerates crack growth. Moreover, the easy decohesion along the inclusions and M/A stringers facilitates faster short fatigue crack propagation under the hydrogen atmosphere. Coalescence of the short fatigue crack with the blisters resulted in a rapid increase in the crack length and reduced the number of cycles for propagation to the equivalent crack length. These results led to the conclusion that the presence of H-induced blisters (developed during the H-charging process prior to loading) can indeed accelerate the loss of structural integrity during external loading.

7.2   Scope for future studies

The possible immediate extensions of the current work for the future include:

- Development of coupled computation framework comprising crystal plasticity, phase field fracture, and hydrogen transport model to study the hydrogen-induced blistering phenomenon and the effect of hydrogen on short fatigue analysis.

- Application of novel identical oligocrystal framework for investigating the effect of various microstructural parameters and loading conditions on fatigue behavior.

- Experimentation using combined in-situ H-charging, digital image correlation (DIC) analysis, and atomic force microscopy (AFM) for oligocrystal samples to develop a deeper understanding and henceforth to calibrate crystal plasticity models more accurately.

References

[1] Y Yagodzinskyy, T Saukkonen, H Hänninen, F Tuomisto, S Barannikova, and L Zuev. Effect of hydrogen on plastic strain localization in single crystals of nickel and austenitic stainless steel. In *B.P. Somerday, P. Sofronis, R.C. Jones (Eds.), Proceedings of the International Hydrogen Conference, Wyoming, USA*, pages 97–104, 2008.

[2] Stéphanie Bouckaert, Araceli Fernandez Pales, Christophe McGlade, Uwe Remme, Brent Wanner, Laszlo Varro, Davide D'Ambrosio, and Thomas Spencer. Net zero by 2050: A roadmap for the global energy sector. 2021.

[3] Dubai Declaration IEA. Global hydrogen review 2021. *Public Report*, 2021.

[4] Alessandro Campari, Federico Ustolin, Antonio Alvaro, and Nicola Paltrinieri. A review on hydrogen embrittlement and risk-based inspection of hydrogen technologies. *International Journal of Hydrogen Energy*, 2023.

[5] Ian M Robertson, P Sofronis, A Nagao, ML Martin, S Wang, DW Gross, and KE Nygren. Hydrogen embrittlement understood. *Metallurgical and Materials Transactions A*, 46(6):2323–2341, 2015.

[6] Stan Lynch. Hydrogen embrittlement phenomena and mechanisms. *Corrosion reviews*, 30(3-4):105–123, 2012.

[7] Milos B Djukic, Gordana M Bakic, Vera Sijacki Zeravcic, Aleksandar Sedmak, and Bratislav Rajicic. The synergistic action and interplay of hydrogen embrittlement mechanisms in steels and iron: Localized plasticity and decohesion. *Engineering Fracture Mechanics*, 216:106528, 2019.

[8] William H Johnson. Ii. on some remarkable changes produced in iron and steel by the action of hydrogen and acids. *Proceedings of the Royal Society of London*, 23 (156-163):168–179, 1875.

[9] Osborne Reynolds. On the effect of acid on the interior of iron wire. *Journal of the Franklin Institute*, 99(1):70–72, 1875.

[10] Stan Lynch. Discussion of some recent literature on hydrogen-embrittlement mechanisms: addressing common misunderstandings. *Corrosion Reviews*, 37(5): 377–395, 2019.

[11] Alexander R Troiano. The role of hydrogen and other interstitials in the mechanical behavior of metals. *Transactions of the ASM*, 52:54–81, 1960.

[12] WW Gerberich, RA Oriani, M-J Lji, X Chen, and T Foecke. The necessity of both plasticity and brittleness in the fracture thresholds of iron. *Philosophical Magazine A*, 63(2):363–376, 1991.

[13] Howard K Birnbaum and Petros Sofronis. Hydrogen-enhanced localized plasticity—a mechanism for hydrogen-related fracture. *Materials Science and Engineering: A*, 176 (1-2):191–202, 1994.

[14] IM Robertson. The effect of hydrogen on dislocation dynamics. *Engineering fracture mechanics*, 68(6):671–692, 2001.

[15] ML Martin, BP Somerday, RO Ritchie, P Sofronis, and IM Robertson. Hydrogen-induced intergranular failure in nickel revisited. *Acta Materialia*, 60(6-7): 2739–2745, 2012.

[16] Milos B Djukic, V Sijacki Zeravcic, Gordana M Bakic, Aleksandar Sedmak, and Bratislav Rajicic. Hydrogen damage of steels: A case study and hydrogen embrittlement model. *Engineering Failure Analysis*, 58:485–498, 2015.

[17] May L Martin and Petros Sofronis. Hydrogen-induced cracking and blistering in steels: A review. *Journal of Natural Gas Science and Engineering*, 101:104547, 2022.

[18] Rakesh Kumar and Dhiraj K Mahajan. Hydrogen distribution in metallic polycrystals with deformation. *Journal of the Mechanics and Physics of Solids*, 135:103776, 2020.

[19] Gustavo M Castelluccio, Clint B Geller, and David L McDowell. A rationale for modeling hydrogen effects on plastic deformation across scales in fcc metals. *International Journal of Plasticity*, 111:72–84, 2018.

[20] Abdelrahman Hussein, Alfons HM Krom, Poulumi Dey, Gagus K Sunnardianto, Othonas A Moultos, and Carey L Walters. The effect of hydrogen content and yield strength on the distribution of hydrogen in steel: a diffusion coupled micromechanical fem study. *Acta Materialia*, 209:116799, 2021.

[21] HamadUl Hassan, Kishan Govind, and Alexander Hartmaier. Micromechanical modelling of coupled crystal plasticity and hydrogen diffusion. *Philosophical Magazine*, 99(1):92–115, 2019.

[22] Edmund Tarleton. Incorporating hydrogen in mesoscale models. *Computational Materials Science*, 163:282–289, 2019.

[23] Zachary D. Harris, Samantha K. Lawrence, Douglas L. Medlin, Gael Guetard, James T. Burns, and Brian P. Somerday. Elucidating the contribution of mobile hydrogen-deformation interactions to hydrogen-induced intergranular cracking in polycrystalline nickel. *Acta Materialia*, 158:180–192, 2018. ISSN 1359-6454.

[24] Kentaro Wada, Junichiro Yamabe, and Hisao Matsunaga. Visualization of trapped hydrogen along grain boundaries and its quantitative contribution to hydrogen-induced intergranular fracture in pure nickel. *Materialia*, 8:100478, 2019. ISSN 2589-1529.

[25] May L Martin, Mohsen Dadfarnia, Akihide Nagao, Shuai Wang, and Petros Sofronis. Enumeration of the hydrogen-enhanced localized plasticity mechanism for hydrogen embrittlement in structural materials. *Acta Materialia*, 165:734–750, 2019.

[26] D Hardie, EA Charles, and AH Lopez. Hydrogen embrittlement of high strength pipeline steels. *Corrosion Science*, 48(12):4378–4385, 2006.

[27] MA Mohtadi-Bonab, JA Szpunar, and SS Razavi-Tousi. A comparative study of hydrogen induced cracking behavior in api 5l x60 and x70 pipeline steels. *Engineering Failure Analysis*, 33:163–175, 2013.

[28] HB Xue and YF Cheng. Characterization of inclusions of x80 pipeline steel and its correlation with hydrogen-induced cracking. *Corrosion science*, 53(4):1201–1208, 2011.

[29] Gyu Tae Park, Sung Ung Koh, Hwan Gyo Jung, and Kyoo Young Kim. Effect of microstructure on the hydrogen trapping efficiency and hydrogen induced cracking of linepipe steel. *Corrosion science*, 50(7):1865–1871, 2008.

[30] CF Dong, XG Li, ZY Liu, and YR Zhang. Hydrogen-induced cracking and healing behaviour of x70 steel. *Journal of alloys and compounds*, 484(1-2):966–972, 2009.

[31] Mohsen Dadfarnia, Akihide Nagao, Shuai Wang, May L Martin, Brian P Somerday, and Petros Sofronis. Recent advances on hydrogen embrittlement of structural materials. *International Journal of Fracture*, 196(1):223–243, 2015a.

[32] D Guedes, L Cupertino Malheiros, A Oudriss, S Cohendoz, J Bouhattate, Jordi Creus, F Thébault, M Piette, and X Feaugas. The role of plasticity and hydrogen flux in the fracture of a tempered martensitic steel: A new design of mechanical test until fracture to separate the influence of mobile from deeply trapped hydrogen. *Acta Materialia*, 186:133–148, 2020.

[33] W. Gerberich. 8 - modeling hydrogen induced damage mechanisms in metals. In Richard P. Gangloff and Brian P. Somerday, editors, *Gaseous Hydrogen Embrittlement of Materials in Energy Technologies*, volume 1, pages 209–246. Woodhead Publishing, 2012. ISBN 978-0-85709-536-7.

[34] RA Oriani. A mechanistic theory of hydrogen embrittlement of steels. *Berichte der Bunsengesellschaft für physikalische Chemie*, 76(8):848–857, 1972.

[35] Cedric D Beachem. A new model for hydrogen-assisted cracking (hydrogen "embrittlement"). *Metallurgical and Materials Transactions B*, 3(2):441–455, 1972.

[36] PJ Ferreira, IM Robertson, and HK Birnbaum. Hydrogen effects on the interaction between dislocations. *Acta materialia*, 46(5):1749–1757, 1998.

[37] Shuai Wang, Naoyuki Hashimoto, and Somei Ohnuki. Effects of hydrogen on activation volume and density of mobile dislocations in iron-based alloy. *Materials Science and Engineering: A*, 562:101–108, 2013.

[38] Petros Sofronis. The influence of mobility of dissolved hydrogen on the elastic response of a metal. *Journal of the Mechanics and Physics of Solids*, 43(9): 1385–1407, 1995.

[39] D. Delafosse. Hydrogen effects on the plasticity of face centred cubic (fcc) crystals. In Richard P. Gangloff and Brian P. Somerday, editors, *Gaseous Hydrogen Embrittlement of Materials in Energy Technologies*, volume 1, pages 247–285. Woodhead Publishing, 2012. ISBN 978-0-85709-536-7.

[40] Yejun Gu and Jaafar A El-Awady. Quantifying the effect of hydrogen on dislocation dynamics: A three-dimensional discrete dislocation dynamics framework. *Journal of the Mechanics and Physics of Solids*, 112:491–507, 2018.

[41] Haiyang Yu, Alan CF Cocks, and Edmund Tarleton. Simulating hydrogen in fcc materials with discrete dislocation plasticity. *International Journal of Hydrogen Energy*, 45(28):14565–14577, 2020a.

[42] Haiyang Yu, Ivaylo H Katzarov, Anthony T Paxton, Alan CF Cocks, and Edmund Tarleton. Influence of hydrogen core force shielding on dislocation junctions in iron. *Physical Review Materials*, 4(3):033607, 2020b.

[43] Gaute Stenerud, Roy Johnsen, Jim Stian Olsen, Jianying He, and Afrooz Barnoush. Effect of hydrogen on dislocation nucleation in alloy 718. *International Journal of Hydrogen Energy*, 42(24):15933–15942, 2017.

[44] Afrooz Barnoush, Masoud Asgari, and Roy Johnsen. Resolving the hydrogen effect on dislocation nucleation and mobility by electrochemical nanoindentation. *Scripta Materialia*, 66(6):414–417, 2012.

[45] E Sirois and HK Birnbaum. Effects of hydrogen and carbon on thermally activated deformation in nickel. *Acta metallurgica et materialia*, 40(6):1377–1385, 1992.

[46] Shinya Taketomi, Ryosuke Matsumoto, and Noriyuki Miyazaki. Atomistic study of the competitive relationship between edge dislocation motion and hydrogen diffusion in alpha iron. *Journal of Materials Research*, 26(10):1269–1278, 2011.

[47] Haiyang Yu, Alan CF Cocks, and Edmund Tarleton. The influence of hydrogen on lomer junctions. *Scripta Materialia*, 166:173–177, 2019.

[48] Shulin Yuan, Yaxin Zhu, Minsheng Huang, Shuang Liang, and Zhenhuan Li. Dislocation-density based crystal plasticity model with hydrogen-enhanced localized plasticity in polycrystalline face-centered cubic metals. *Mechanics of Materials*, 148: 103472, 2020.

[49] JP Chateau, D Delafosse, and Th Magnin. Numerical simulations of hydrogen–dislocation interactions in fcc stainless steels.: part i: hydrogen–dislocation interactions in bulk crystals. *Acta Materialia*, 50(6): 1507–1522, 2002.

[50] RB Sills and W Cai. Free energy change of a dislocation due to a cottrell atmosphere. *Philosophical Magazine*, 98(16):1491–1510, 2018.

[51] Gouenou Girardin, C Huvier, David Delafosse, and X Feaugas. Correlation between dislocation organization and slip bands: Tem and afm investigations in hydrogen-containing nickel and nickel–chromium. *Acta Materialia*, 91:141–151, 2015.

[52] Shuai Wang, Akihide Nagao, Kaveh Edalati, Zenji Horita, and Ian M Robertson. Influence of hydrogen on dislocation self-organization in ni. *Acta Materialia*, 135: 96–102, 2017.

[53] Dmitrii N Ilin, Nicolas Saintier, Jean-Marc Olive, Remi Abgrall, and Isabelle Aubert. Simulation of hydrogen diffusion affected by stress-strain heterogeneity in polycrystalline stainless steel. *International Journal of Hydrogen Energy*, 39(5): 2418–2422, 2014.

[54] Yann Charles, Hung Tuan Nguyen, and Monique Gaspérini. Comparison of hydrogen transport through pre-deformed synthetic polycrystals and homogeneous samples by finite element analysis. *International Journal of Hydrogen Energy*, 42(31): 20336–20350, 2017.

[55] Yann Charles, Monique Gaspérini, Nicolas Fagnon, Kevin Ardon, and Anthony Duhamel. Finite element simulation of hydrogen transport during plastic bulging of iron submitted to gaseous hydrogen pressure. *Engineering Fracture Mechanics*, 218: 106580, 2019.

[56] Theodore Zirkle, Luke Costello, and David L McDowell. Crystal plasticity modeling of hydrogen and hydrogen-related defects in initial yield and plastic flow of single-crystal stainless steel 316l. *Metallurgical and Materials Transactions A*, 52 (9):3961–3977, 2021.

[57] IMA Ghermaoui, A Oudriss, A Metsue, R Milet, K Madani, and X Feaugas. Multiscale analysis of hydrogen-induced softening in fcc nickel single crystals oriented for multiple-slips: elastic screening effect. *Scientific Reports*, 9(1):1–10, 2019.

[58] BURAK Bal, M Koyama, D Canadinc, G Gerstein, HJ Maier, and K Tsuzaki. On the utility of crystal plasticity modeling to uncover the individual roles of

microdeformation mechanisms on the work hardening response of fe-23mn-0.5 c twip steel in the presence of hydrogen. *Journal of Engineering Materials and Technology*, 140(3):031002, 2018.

[59] Nikolaos Vasios. Crystal plasticity: A rate-independent constitutive model. the effect of hydrogen concentration. *University of Thessaly, Thessaly, Greece*, 2015.

[60] Eugene Ogosi, Amir Siddiq, Umair Bin Asim, and Mehmet E Kartal. Crystal plasticity based study to understand the interaction of hydrogen, defects and loading in austenitic stainless-steel single crystals. *International Journal of Hydrogen Energy*, 45(56):32632–32647, 2020.

[61] JCM Li, RA Oriani, and LS Darken. The thermodynamics of stressed solids. *Zeitschrift für Physikalische Chemie*, 49(3_5):271–290, 1966.

[62] Mohsen Dadfarnia, May L Martin, Akihide Nagao, Petros Sofronis, and Ian M Robertson. Modeling hydrogen transport by dislocations. *Journal of the Mechanics and Physics of Solids*, 78:511–525, 2015b.

[63] Richard A Oriani. The diffusion and trapping of hydrogen in steel. *Acta metallurgica*, 18(1):147–157, 1970.

[64] Alfons HM Krom, Ronald WJ Koers, and AD Bakker. Hydrogen transport near a blunting crack tip. *Journal of the Mechanics and Physics of Solids*, 47(4):971–992, 1999.

[65] EH Lee and DT Liu. Finite-strain elastic—plastic theory with application to plane-wave analysis. *Journal of applied physics*, 38(1):19–27, 1967.

[66] E Orowan. Problems of plastic gliding. *Proceedings of the Physical Society (1926-1948)*, 52(1):8, 1940.

[67] Philipp Engels, Anxin Ma, and Alexander Hartmaier. Continuum simulation of the evolution of dislocation densities during nanoindentation. *International journal of plasticity*, 38:159–169, 2012.

[68] H Mecking and UF Kocks. Kinetics of flow and strain-hardening. *Acta metallurgica*, 29(11):1865–1875, 1981.

[69] P Franciosi and A Zaoui. Multislip in fcc crystals a theoretical approach compared with experimental data. *Acta Metallurgica*, 30(8):1627–1637, 1982.

[70] Curt Allan Bronkhorst, Jason Rhea Mayeur, Veronica Livescu, R Pokharel, Donald William Brown, and George Thompson Gray III. Structural representation of additively manufactured 316l austenitic stainless steel. *International Journal of Plasticity*, 118:70–86, 2019.

[71] Benoit Devincre, Ladislas Kubin, and Thierry Hoc. Physical analyses of crystal plasticity by dd simulations. *Scripta materialia*, 54(5):741–746, 2006.

[72] Qian Liu and Andrej Atrens. A critical review of the influence of hydrogen on the mechanical properties of medium-strength steels. *Corrosion Reviews*, 31(3-6): 85–103, 2013.

[73] Suzhi Li, Yonggang Li, Yu-Chieh Lo, Thirumalai Neeraj, Rajagopalan Srinivasan, Xiangdong Ding, Jun Sun, Liang Qi, Peter Gumbsch, and Ju Li. The interaction of dislocations and hydrogen-vacancy complexes and its importance for deformation-induced proto nano-voids formation in α-fe. *International Journal of Plasticity*, 74:175–191, 2015.

[74] RB Sills and W Cai. Solute drag on perfect and extended dislocations. *Philosophical Magazine*, 96(10):895–921, 2016.

[75] Gregory J Schebler. On the mechanics of the hydrogen interaction with single crystal plasticity. *University of Illinois at Urbana-Champaign, Illinois, United States*, 2010.

[76] O Barrera, E Tarleton, HW Tang, and ACF Cocks. Modelling the coupling between hydrogen diffusion and the mechanical behaviour of metals. *Computational Materials Science*, 122:219–228, 2016.

[77] Pauli Virtanen, Ralf Gommers, Travis E Oliphant, Matt Haberland, Tyler Reddy, David Cournapeau, Evgeni Burovski, Pearu Peterson, Warren Weckesser, Jonathan Bright, et al. Scipy 1.0: fundamental algorithms for scientific computing in python. *Nature methods*, 17(3):261–272, 2020.

[78] Rémi Delaporte-Mathurin, Etienne A Hodille, Jonathan Mougenot, Yann Charles, and Christian Grisolia. Parametric optimisation based on tds experiments for rapid and efficient identification of hydrogen transport materials properties. *Nuclear Materials and Energy*, 27:100984, 2021.

[79] Aritra Chakraborty and Philip Eisenlohr. Evaluation of an inverse methodology for estimating constitutive parameters in face-centered cubic materials from single crystal indentations. *European Journal of Mechanics-A/Solids*, 66:114–124, 2017.

[80] Romain Quey, PR Dawson, and Fabrice Barbe. Large-scale 3d random polycrystals for the finite element method: Generation, meshing and remeshing. *Computer Methods in Applied Mechanics and Engineering*, 200(17-20):1729–1745, 2011.

[81] Nicolo Grilli, Edmund Tarleton, and Alan CF Cocks. Neper2cae and pycigen: Scripts to generate polycrystals and interface elements in abaqus. *SoftwareX*, 13:100651, 2021.

[82] L Kubin, B Devincre, and T Hoc. Modeling dislocation storage rates and mean free paths in face-centered cubic crystals. *Acta materialia*, 56(20):6040–6049, 2008.

[83] James E Angelo, Neville R Moody, and Michael I Baskes. Trapping of hydrogen to lattice defects in nickel. *Modelling and Simulation in Materials Science and Engineering*, 3(3):289–307, 1995.

[84] J Li, A Oudriss, A Metsue, J Bouhattate, and X Feaugas. Anisotropy of hydrogen diffusion in nickel single crystals: the effects of self-stress and hydrogen concentration on diffusion. *Scientific reports*, 7(1):1–9, 2017.

[85] Samantha K Lawrence, Yuriy Yagodzinskyy, Hannu Hänninen, Esa Korhonen, Filip Tuomisto, Zachary D Harris, and Brian P Somerday. Effects of grain size and deformation temperature on hydrogen-enhanced vacancy formation in ni alloys. *Acta Materialia*, 128:218–226, 2017.

[86] Ryan B Sills and BL Boyce. Void growth by dislocation adsorption. *Materials Research Letters*, 8(3):103–109, 2020.

[87] May L Martin, Jamey A Fenske, Grace S Liu, Petros Sofronis, and Ian M Robertson. On the formation and nature of quasi-cleavage fracture surfaces in hydrogen embrittled steels. *Acta Materialia*, 59(4):1601–1606, 2011.

[88] T Boniszewski and G.C Smith. The influence of hydrogen on the plastic deformation ductility, and fracture of nickel in tension. *Acta Metallurgica*, 11(3):165–178, 1963. ISSN 0001-6160.

[89] S. Bechtle, M. Kumar, B.P. Somerday, M.E. Launey, and R.O. Ritchie. Grain-boundary engineering markedly reduces susceptibility to intergranular hydrogen embrittlement in metallic materials. *Acta Materialia*, 57(14):4148–4157, 2009. ISSN 1359-6454.

[90] Hydrogen-induced compatibility constraints across grain boundaries drive intergranular failure of ni. *Materials Science and Engineering: A*, 760:58–67, 2019. ISSN 0921-5093. doi: https://doi.org/10.1016/j.msea.2019.05.036.

[91] A. Oudriss, J. Creus, J. Bouhattate, E. Conforto, C. Berziou, C. Savall, and X. Feaugas. Grain size and grain-boundary effects on diffusion and trapping of hydrogen in pure nickel. *Acta Materialia*, 60(19):6814–6828, 2012. ISSN 1359-6454.

[92] A. Alvaro, I. Thue Jensen, N. Kheradmand, O.M. Løvvik, and V. Olden. Hydrogen embrittlement in nickel, visited by first principles modeling, cohesive zone simulation and nanomechanical testing. *International Journal of Hydrogen Energy*, 40(47): 16892–16900, 2015. ISSN 0360-3199. Special issue on 1st International Conference on Hydrogen Storage, Embrittlement and Applications (Hy-SEA 2014), 26-30 October 2014, Rio de Janeiro, Brazil.

[93] Vishal Singh, Rakesh Kumar, Yann Charles, and Dhiraj K. Mahajan. Coupled diffusion-mechanics framework for simulating hydrogen assisted deformation and

failure behavior of metals. *International Journal of Plasticity*, 157:103392, 2022. ISSN 0749-6419.

[94] Tadao Watanabe. The impact of grain boundary character distribution on fracture in polycrystals. *Materials Science and Engineering: A*, 176(1):39–49, 1994. ISSN 0921-5093.

[95] Tarlan Hajilou, Iman Taji, Frederic Christien, Shuang He, Daniel Scheiber, Werner Ecker, Reinhard Pippan, Vsevolod I. Razumovskiy, and Afrooz Barnoush. Hydrogen-enhanced intergranular failure of sulfur-doped nickel grain boundary: In situ electrochemical micro-cantilever bending vs. dft. *Materials Science and Engineering: A*, 794:139967, 2020. ISSN 0921-5093.

[96] A. Oudriss, S. Le Guernic, Z. Wang, B. Osman Hoch, J. Bouhattate, E. Conforto, Z. Zhu, D.S. Li, and X. Feaugas. Meso-scale anisotropic hydrogen segregation near grain-boundaries in polycrystalline nickel characterized by ebsd/sims. *Materials Letters*, 165:217–222, 2016. ISSN 0167-577X.

[97] Honglei Hu, Mingjiu Zhao, Shenghu Chen, and Lijian Rong. Effect of grain boundary character distribution on hydrogen embrittlement in fe–ni based alloy. *Materials Science and Engineering: A*, 780:139201, 2020. ISSN 0921-5093.

[98] Han Lin Mai, Xiang-Yuan Cui, Daniel Scheiber, Lorenz Romaner, and Simon P. Ringer. An understanding of hydrogen embrittlement in nickel grain boundaries from first principles. *Materials Design*, 212:110283, 2021. ISSN 0264-1275.

[99] Davide Di Stefano, Matous Mrovec, and Christian Elsässer. First-principles investigation of hydrogen trapping and diffusion at grain boundaries in nickel. *Acta Materialia*, 98:306–312, 2015. ISSN 1359-6454.

[100] Yu Ding, Haiyang Yu, Meichao Lin, Kai Zhao, Senbo Xiao, Alexey Vinogradov, Lijie Qiao, Michael Ortiz, Jianying He, and Zhiliang Zhang. Hydrogen-enhanced grain boundary vacancy stockpiling causes transgranular to intergranular fracture transition. *Acta Materialia*, 239:118279, 2022. ISSN 1359-6454.

[101] Matteo Seita, John P Hanson, Silvija Gradečak, and Michael J Demkowicz. The dual role of coherent twin boundaries in hydrogen embrittlement. *Nature communications*, 6(1):6164, 2015.

[102] D.H. Lassila and H.K. Birnbaum. Intergranular fracture of nickel: the effect of hydrogen-sulfur co-segregation. *Acta Metallurgica*, 35(7):1815–1822, 1987. ISSN 0001-6160.

[103] Eralp Demir and Ivan Gutierrez-Urrutia. Investigation of strain hardening near grain boundaries of an aluminum oligocrystal: Experiments and crystal based finite element method. *International Journal of Plasticity*, 136:102898, 2021. ISSN 0749-6419.

[104] Hojun Lim, Jay D. Carroll, Corbett C. Battaile, Brad L. Boyce, and Christopher R. Weinberger. Quantitative comparison between experimental measurements and cp-fem predictions of plastic deformation in a tantalum oligocrystal. *International Journal of Mechanical Sciences*, 92:98–108, 2015. ISSN 0020-7403.

[105] Z. Zhao, M. Ramesh, D. Raabe, A.M. Cuitiño, and R. Radovitzky. Investigation of three-dimensional aspects of grain-scale plastic surface deformation of an aluminum oligocrystal. *International Journal of Plasticity*, 24(12):2278–2297, 2008. ISSN 0749-6419.

[106] Yongjun Guan, Bo Chen, Jinwen Zou, T. Ben Britton, Jun Jiang, and Fionn P.E. Dunne. Crystal plasticity modelling and hr-dic measurement of slip activation and strain localization in single and oligo-crystal ni alloys under fatigue. *International Journal of Plasticity*, 88:70–88, 2017. ISSN 0749-6419.

[107] P. Lorenzino, A. Navarro, and U. Krupp. Naked eye observations of microstructurally short fatigue cracks. *International Journal of Fatigue*, 56:8–16, 2013. ISSN 0142-1123.

[108] Zhaoxiang Ma, Xilin Xiong, and Yanjing Su. Study on hydrogen segregation at individual grain boundaries in pure nickel by scanning kelvin probe force microscopy. *Materials Letters*, 303:130528, 2021. ISSN 0167-577X.

[109] Qingqing Sun, Jinhua Han, Jiaxing Li, Fahe Cao, and Shuai Wang. Tailoring hydrogen embrittlement resistance of pure ni by grain boundary engineering. *Corrosion Communications*, 6:48–51, 2022. ISSN 2667-2669.

[110] Vishal Singh, Rajwinder Singh, Kanwer Singh Arora, and Dhiraj K. Mahajan. Hydrogen induced blister cracking and mechanical failure in x65 pipeline steels. *International Journal of Hydrogen Energy*, 44(39):22039–22049, 2019. ISSN 0360-3199.

[111] M.D. McMurtrey, G.S. Was, L. Patrick, and D. Farkas. Relationship between localized strain and irradiation assisted stress corrosion cracking in an austenitic alloy. *Materials Science and Engineering: A*, 528(10):3730–3740, 2011. ISSN 0921-5093.

[112] E. Pouillier, A.-F. Gourgues, D. Tanguy, and E.P. Busso. A study of intergranular fracture in an aluminium alloy due to hydrogen embrittlement. *International Journal of Plasticity*, 34:139–153, 2012. ISSN 0749-6419.

[113] E.A. West and G.S. Was. A model for the normal stress dependence of intergranular cracking of irradiated 316l stainless steel in supercritical water. *Journal of Nuclear Materials*, 408(2):142–152, 2011. ISSN 0022-3115.

[114] Naohiro Kobayashi, Motomichi Koyama, Misaho Yamamura, Tomohiko Hojo, and Eiji Akiyama. Cr effects on the local plasticity evolution and fracture

behaviors of ni–cr alloys tensile-tested under hydrogen charging. *MATERIALS TRANSACTIONS*, 64(1):212–219, 2023. doi: 10.2320/matertrans.MT-M2022140.

[115] A. Tehranchi and W.A. Curtin. Atomistic study of hydrogen embrittlement of grain boundaries in nickel: I. fracture. *Journal of the Mechanics and Physics of Solids*, 101:150–165, 2017. ISSN 0022-5096.

[116] Shuai Wang, May L. Martin, Ian M. Robertson, and Petros Sofronis. Effect of hydrogen environment on the separation of fe grain boundaries. *Acta Materialia*, 107:279–288, 2016. ISSN 1359-6454.

[117] Abdelrahman Hussein, Alfons H.M. Krom, Poulumi Dey, Gagus K. Sunnardianto, Othonas A. Moultos, and Carey L. Walters. The effect of hydrogen content and yield strength on the distribution of hydrogen in steel: a diffusion coupled micromechanical fem study. *Acta Materialia*, 209:116799, 2021. ISSN 1359-6454.

[118] Di Wan, Yun Deng, Jan Inge Hammer Meling, Antonio Alvaro, and Afrooz Barnoush. Hydrogen-enhanced fatigue crack growth in a single-edge notched tensile specimen under in-situ hydrogen charging inside an environmental scanning electron microscope. *Acta Materialia*, 170:87–99, 2019. ISSN 1359-6454.

[119] Alisa Stratulat, Jonathan A. Duff, and T. James Marrow. Grain boundary structure and intergranular stress corrosion crack initiation in high temperature water of a thermally sensitised austenitic stainless steel, observed in situ. *Corrosion Science*, 85:428–435, 2014. ISSN 0010-938X.

[120] T Boniszewski and GC Smith. The influence of hydrogen on the plastic deformation ductility, and fracture of nickel in tension. *Acta metallurgica*, 11(3):165–178, 1963.

[121] Burak Bal, Motonnchi Koyama, Gregory Gerstein, Hans Juergen Maier, and Kaneaki Tsuzaki. Effect of strain rate on hydrogen embrittlement susceptibility of twinning-induced plasticity steel pre-charged with high-pressure hydrogen gas. *international journal of hydrogen energy*, 41(34):15362–15372, 2016.

[122] CD Gu, JS Lian, Q Jiang, and WT Zheng. Experimental and modelling investigations on strain rate sensitivity of an electrodeposited 20 nm grain sized ni. *Journal of Physics D: Applied Physics*, 40(23):7440, 2007.

[123] Maxim N Gussev and Keith J Leonard. In situ sem-ebsd analysis of plastic deformation mechanisms in neutron-irradiated austenitic steel. *Journal of Nuclear Materials*, 517:45–56, 2019.

[124] FT Meissonnier, EP Busso, and NP O'Dowd. Finite element implementation of a generalised non-local rate-dependent crystallographic formulation for finite strains. *International Journal of Plasticity*, 17(4):601–640, 2001.

[125] Surya R Kalidindi. Modeling anisotropic strain hardening and deformation textures in low stacking fault energy fcc metals. *International Journal of Plasticity*, 17(6): 837–860, 2001.

[126] Anxin Ma and Alexander Hartmaier. On the influence of isotropic and kinematic hardening caused by strain gradients on the deformation behaviour of polycrystals. *Philosophical Magazine*, 94(2):125–140, 2014.

[127] Franz Roters, Philip Eisenlohr, Thomas R Bieler, and Dierk Raabe. *Crystal plasticity finite element methods: in materials science and engineering*. John Wiley & Sons, 2011.

[128] Franz Roters, Martin Diehl, Pratheek Shanthraj, Philip Eisenlohr, C Reuber, Su Leen Wong, Tias Maiti, Alireza Ebrahimi, Thomas Hochrainer, H-O Fabritius, et al. Damask–the düsseldorf advanced material simulation kit for modeling multi-physics crystal plasticity, thermal, and damage phenomena from the single crystal up to the component scale. *Computational Materials Science*, 158:420–478, 2019.

[129] Sergio Lucarini, Fionn PE Dunne, and Emilio Martínez-Pañeda. An fft-based crystal plasticity phase-field model for micromechanical fatigue cracking based on the stored energy density. *International Journal of Fatigue*, 172:107670, 2023.

[130] Nicolas Moës, John Dolbow, and Ted Belytschko. A finite element method for crack growth without remeshing. *International journal for numerical methods in engineering*, 46(1):131–150, 1999.

[131] Ivo Babuška, Uday Banerjee, and John E Osborn. Generalized finite element methods—main ideas, results and perspective. *International Journal of Computational Methods*, 1(01):67–103, 2004.

[132] Bernardo Cockburn. Discontinuous galerkin methods. *ZAMM-Journal of Applied Mathematics and Mechanics/Zeitschrift für Angewandte Mathematik und Mechanik: Applied Mathematics and Mechanics*, 83(11):731–754, 2003.

[133] OC Zienkiewicz, RL Taylor, SJ Sherwin, and J20092031032 Peiro. On discontinuous galerkin methods. *International journal for numerical methods in engineering*, 58 (8):1119–1148, 2003.

[134] A Needleman. An analysis of tensile decohesion along an interface. *Journal of the Mechanics and Physics of Solids*, 38(3):289–324, 1990.

[135] Michael Ortiz and Anna Pandolfi. Finite-deformation irreversible cohesive elements for three-dimensional crack-propagation analysis. *International journal for numerical methods in engineering*, 44(9):1267–1282, 1999.

[136] David Wilson and Fionn PE Dunne. A mechanistic modelling methodology for microstructure-sensitive fatigue crack growth. *Journal of the Mechanics and Physics of Solids*, 124:827–848, 2019.

[137] Farukh Farukh, LG Zhao, Rong Jiang, P Reed, Daniela Proprentner, and Barbara A Shollock. Realistic microstructure-based modelling of cyclic deformation and crack growth using crystal plasticity. *Computational Materials Science*, 111:395–405, 2016.

[138] Xiaoxian Zhang and Fionn PE Dunne. 3d cp-xfem modelling of short crack propagation interacting with twist/tilt nickel grain boundaries. *Journal of the Mechanics and Physics of Solids*, 168:105028, 2022.

[139] Qi Zhao, Magd Abdel Wahab, Yong Ling, and Zhiyi Liu. Fatigue crack propagation within al-cu-mg single crystals based on crystal plasticity and xfem combined with cohesive zone model. *Materials & Design*, 210:110015, 2021.

[140] Henry Proudhon, Jia Li, F Wang, A Roos, Vincent Chiaruttini, and Samuel Forest. 3d simulation of short fatigue crack propagation by finite element crystal plasticity and remeshing. *International Journal of fatigue*, 82:238–246, 2016.

[141] Nicolò Grilli, Alan CF Cocks, and Edmund Tarleton. Modelling the nucleation and propagation of cracks at twin boundaries. *International Journal of Fracture*, pages 1–22, 2022.

[142] M Cervera, GB Barbat, Michele Chiumenti, and J-Y Wu. A comparative review of xfem, mixed fem and phase-field models for quasi-brittle cracking. *Archives of Computational Methods in Engineering*, 29(2):1009–1083, 2022.

[143] Jiahao Cheng, Xiaohui Tu, and Somnath Ghosh. Wavelet-enriched adaptive hierarchical fe model for coupled crystal plasticity-phase field modeling of crack propagation in polycrystalline microstructures. *Computer Methods in Applied Mechanics and Engineering*, 361:112757, 2020.

[144] Blaise Bourdin, Gilles A Francfort, and Jean-Jacques Marigo. The variational approach to fracture. *Journal of elasticity*, 91:5–148, 2008.

[145] Christian Miehe, Fabian Welschinger, and Martina Hofacker. Thermodynamically consistent phase-field models of fracture: Variational principles and multi-field fe implementations. *International journal for numerical methods in engineering*, 83 (10):1273–1311, 2010.

[146] Christian Miehe, Martina Hofacker, L-M Schänzel, and Fadi Aldakheel. Phase field modeling of fracture in multi-physics problems. part ii. coupled brittle-to-ductile failure criteria and crack propagation in thermo-elastic–plastic solids. *Computer Methods in Applied Mechanics and Engineering*, 294:486–522, 2015.

[147] Christian Miehe and Steffen Mauthe. Phase field modeling of fracture in multi-physics problems. part iii. crack driving forces in hydro-poro-elasticity and hydraulic fracturing of fluid-saturated porous media. *Computer Methods in Applied Mechanics and Engineering*, 304:619–655, 2016.

[148] JD Clayton and JJCMS Knap. Phase field modeling of directional fracture in anisotropic polycrystals. *Computational Materials Science*, 98:158–169, 2015.

[149] Colin McAuliffe and Haim Waisman. A coupled phase field shear band model for ductile–brittle transition in notched plate impacts. *Computer Methods in Applied Mechanics and Engineering*, 305:173–195, 2016.

[150] Marreddy Ambati, Tymofiy Gerasimov, and Laura De Lorenzis. A review on phase-field models of brittle fracture and a new fast hybrid formulation. *Computational Mechanics*, 55:383–405, 2015.

[151] Blaise Bourdin, Gilles A Francfort, and Jean-Jacques Marigo. Numerical experiments in revisited brittle fracture. *Journal of the Mechanics and Physics of Solids*, 48(4):797–826, 2000.

[152] Emilio Martínez-Pañeda, Alireza Golahmar, and Christian F Niordson. A phase field formulation for hydrogen assisted cracking. *Computer Methods in Applied Mechanics and Engineering*, 342:742–761, 2018.

[153] Gilles A Francfort and J-J Marigo. Revisiting brittle fracture as an energy minimization problem. *Journal of the Mechanics and Physics of Solids*, 46(8): 1319–1342, 1998.

[154] Tymofiy Gerasimov and Laura De Lorenzis. A line search assisted monolithic approach for phase-field computing of brittle fracture. *Computer Methods in Applied Mechanics and Engineering*, 312:276–303, 2016.

[155] Michael J Borden, Thomas JR Hughes, Chad M Landis, and Clemens V Verhoosel. A higher-order phase-field model for brittle fracture: Formulation and analysis within the isogeometric analysis framework. *Computer Methods in Applied Mechanics and Engineering*, 273:100–118, 2014.

[156] José Reinoso, A Arteiro, Marco Paggi, and PP Camanho. Strength prediction of notched thin ply laminates using finite fracture mechanics and the phase field approach. *Composites Science and Technology*, 150:205–216, 2017.

[157] Michael J Borden, Thomas JR Hughes, Chad M Landis, Amin Anvari, and Isaac J Lee. A phase-field formulation for fracture in ductile materials: Finite deformation balance law derivation, plastic degradation, and stress triaxiality effects. *Computer Methods in Applied Mechanics and Engineering*, 312:130–166, 2016.

[158] Gergely Molnár and Anthony Gravouil. 2d and 3d abaqus implementation of a robust staggered phase-field solution for modeling brittle fracture. *Finite Elements in Analysis and Design*, 130:27–38, 2017.

[159] Yousef Navidtehrani, Covadonga Betegon, and Emilio Martinez-Paneda. A unified abaqus implementation of the phase field fracture method using only a user material subroutine. *Materials*, 14(8):1913, 2021.

[160] A Valverde-González, E Martínez-Pañeda, A Quintanas-Corominas, J Reinoso, and M Paggi. Computational modelling of hydrogen assisted fracture in polycrystalline materials. *international journal of hydrogen energy*, 47(75):32235–32251, 2022.

[161] Christian Miehe, Martina Hofacker, and Fabian Welschinger. A phase field model for rate-independent crack propagation: Robust algorithmic implementation based on operator splits. *Computer Methods in Applied Mechanics and Engineering*, 199 (45-48):2765–2778, 2010.

[162] Z Liu, J Reinoso, and M Paggi. Phase field modeling of brittle fracture in large-deformation solid shells with the efficient quasi-newton solution and global–local approach. *Computer Methods in Applied Mechanics and Engineering*, 399:115410, 2022.

[163] Marreddy Ambati, Tymofiy Gerasimov, and Laura De Lorenzis. Phase-field modeling of ductile fracture. *Computational Mechanics*, 55:1017–1040, 2015.

[164] Christian Miehe, Fadi Aldakheel, and Stephan Teichtmeister. Phase-field modeling of ductile fracture at finite strains: A robust variational-based numerical implementation of a gradient-extended theory by micromorphic regularization. *International Journal for Numerical Methods in Engineering*, 111(9):816–863, 2017.

[165] Roberto Alessi, Jean-Jacques Marigo, Corrado Maurini, and Stefano Vidoli. Coupling damage and plasticity for a phase-field regularisation of brittle, cohesive and ductile fracture: One-dimensional examples. *International Journal of Mechanical Sciences*, 149:559–576, 2018.

[166] Dongyang Chu, Xiang Li, Zhanli Liu, Junbo Cheng, Tao Wang, Zhijie Li, and Zhuo Zhuang. A unified phase field damage model for modeling the brittle-ductile dynamic failure mode transition in metals. *Engineering Fracture Mechanics*, 212:197–209, 2019.

[167] Weijie Mai and Soheil Soghrati. A phase field model for simulating the stress corrosion cracking initiated from pits. *Corrosion Science*, 125:87–98, 2017.

[168] Chuanjie Cui, Rujin Ma, and Emilio Martínez-Pañeda. A generalised, multi-phase-field theory for dissolution-driven stress corrosion cracking and hydrogen embrittlement. *Journal of the Mechanics and Physics of Solids*, 166:104951, 2022.

[169] Fernando P Duda, Angel Ciarbonetti, Sebastian Toro, and Alfredo Edmundo Huespe. A phase-field model for solute-assisted brittle fracture in elastic-plastic solids. *International Journal of Plasticity*, 102:16–40, 2018.

[170] Lallit Anand, Yunwei Mao, and Brandon Talamini. On modeling fracture of ferritic steels due to hydrogen embrittlement. *Journal of the Mechanics and Physics of Solids*, 122:280–314, 2019.

[171] Jian-Ying Wu, Tushar Kanti Mandal, and Vinh Phu Nguyen. A phase-field regularized cohesive zone model for hydrogen assisted cracking. *Computer Methods in Applied Mechanics and Engineering*, 358:112614, 2020.

[172] Chuanshi Huang and Xiaosheng Gao. Phase field modeling of hydrogen embrittlement. *International Journal of Hydrogen Energy*, 45(38):20053–20068, 2020.

[173] Emilio Martínez-Pañeda, Zachary D Harris, Sandra Fuentes-Alonso, John R Scully, and James T Burns. On the suitability of slow strain rate tensile testing for assessing hydrogen embrittlement susceptibility. *Corrosion Science*, 163:108291, 2020.

[174] Laura De Lorenzis, Andrew McBride, and Batmanathan D Reddy. Phase-field modelling of fracture in single crystal plasticity. *GAMM-Mitteilungen*, 39(1):7–34, 2016.

[175] Pratheek Shanthraj, Luv Sharma, Bob Svendsen, Franz Roters, and Dierk Raabe. A phase field model for damage in elasto-viscoplastic materials. *Computer Methods in Applied Mechanics and Engineering*, 312:167–185, 2016.

[176] Xiaohui Tu, Arunava Ray, and Somnath Ghosh. A coupled crystal plasticity fem and phase-field model for crack evolution in microstructures of 7000 series aluminum alloys. *Engineering Fracture Mechanics*, 230:106970, 2020.

[177] Samad Vakili, Pratheek Shanthraj, Franz Roters, Jaber R Mianroodi, and Dierk Raabe. Phase-field modeling of coupled brittle-ductile fracture in aluminum alloys. *arXiv preprint arXiv:2204.13994*, 2022.

[178] Thirupathi Maloth and Somnath Ghosh. Coupled crystal plasticity phase-field model for ductile fracture in polycrystalline microstructures. *International Journal for Multiscale Computational Engineering*, 21(2), 2023.

[179] Christian Miehe, Lisa-Marie Schaenzel, and Heike Ulmer. Phase field modeling of fracture in multi-physics problems. part i. balance of crack surface and failure criteria for brittle crack propagation in thermo-elastic solids. *Computer Methods in Applied Mechanics and Engineering*, 294:449–485, 2015.

[180] Christian Miehe, Fadi Aldakheel, and Arun Raina. Phase field modeling of ductile fracture at finite strains: A variational gradient-extended plasticity-damage theory. *International Journal of Plasticity*, 84:1–32, 2016.

[181] Gergely Molnár, Anthony Gravouil, Rian Seghir, and Julien Réthoré. An open-source abaqus implementation of the phase-field method to study the effect of plasticity on the instantaneous fracture toughness in dynamic crack propagation. *Computer Methods in Applied Mechanics and Engineering*, 365:113004, 2020.

[182] Thaís C da Costa-Haveroth, Geovane Augusto Haveroth, Marco Lúcio Bittencourt, and Jose Luiz Boldrini. A damage phase-field model for fractional viscoelastic materials in finite strain. *Computational Mechanics*, 69(6):1365–1393, 2022.

[183] Tobias Waffenschmidt, César Polindara, Andreas Menzel, and Sergio Blanco. A gradient-enhanced large-deformation continuum damage model for fibre-reinforced materials. *Computer Methods in Applied Mechanics and Engineering*, 268:801–842, 2014.

[184] Richard Ostwald, Ellen Kuhl, and Andreas Menzel. On the implementation of finite deformation gradient-enhanced damage models. *Computational Mechanics*, 64:847–877, 2019.

[185] Ahmad Shahba and Somnath Ghosh. Coupled phase field finite element model for crack propagation in elastic polycrystalline microstructures. *International Journal of Fracture*, 219:31–64, 2019.

[186] Jianguang Fang, Chengqing Wu, Timon Rabczuk, Chi Wu, Conggan Ma, Guangyong Sun, and Qing Li. Phase field fracture in elasto-plastic solids: Abaqus implementation and case studies. *Theoretical and Applied Fracture Mechanics*, 103: 102252, 2019.

[187] Yi Xiong, Nicolò Grilli, Phani S Karamched, Bo-Shiuan Li, Edmund Tarleton, and Angus J Wilkinson. Cold dwell behaviour of ti6al alloy: Understanding load shedding using digital image correlation and dislocation based crystal plasticity simulations. *Journal of Materials Science & Technology*, 128:254–272, 2022.

[188] Thanh-Tung Nguyen, Julien Yvonnet, Q-Z Zhu, Michel Bornert, and Camille Chateau. A phase-field method for computational modeling of interfacial damage interacting with crack propagation in realistic microstructures obtained by microtomography. *Computer Methods in Applied Mechanics and Engineering*, 312: 567–595, 2016.

[189] Peng Zhang, Xiaofei Hu, Shangtong Yang, and Weian Yao. Modelling progressive failure in multi-phase materials using a phase field method. *Engineering Fracture Mechanics*, 209:105–124, 2019.

[190] Avtar Singh and Siladitya Pal. Chemo-mechanical modeling of inter-and intra-granular fracture in heterogeneous cathode with polycrystalline particles for lithium-ion battery. *Journal of the Mechanics and Physics of Solids*, 163:104839, 2022.

[191] Jie Chen and Avinash M Dongare. Role of grain boundary character on oxygen and hydrogen segregation-induced embrittlement in polycrystalline ni. *Journal of Materials Science*, 52:30–45, 2017.

[192] Mariana Cristina de Oliveira, Rodrigo Monzon Figueredo, Heloisa Andrea Acciari, and Eduardo Norberto Codaro. Corrosion behavior of api 5l x65 steel subject to plastic deformation. *Journal of materials research and technology*, 7(3):314–318, 2018.

[193] Enyinnaya Ohaeri, Ubong Eduok, and Jerzy Szpunar. Hydrogen related degradation in pipeline steel: A review. *International Journal of Hydrogen Energy*, 43(31): 14584–14617, 2018.

[194] Rong Wang. Effects of hydrogen on the fracture toughness of a x70 pipeline steel. *Corrosion Science*, 51(12):2803–2810, 2009.

[195] Teng An, Huangtao Peng, Pengpeng Bai, Shuqi Zheng, Xiangli Wen, and Lin Zhang. Influence of hydrogen pressure on fatigue properties of x80 pipeline steel. *International Journal of Hydrogen Energy*, 42(23):15669–15678, 2017.

[196] Teng An, Shuqi Zheng, Huangtao Peng, Xiangli Wen, Liqiang Chen, and Lin Zhang. Synergistic action of hydrogen and stress concentration on the fatigue properties of x80 pipeline steel. *Materials Science and Engineering: A*, 700:321–330, 2017.

[197] Motomichi Koyama, Eiji Akiyama, Young-Kook Lee, Dierk Raabe, and Kaneaki Tsuzaki. Overview of hydrogen embrittlement in high-mn steels. *international journal of hydrogen energy*, 42(17):12706–12723, 2017.

[198] Qinglong Liu, Qingjun Zhou, Jeffrey Venezuela, Mingxing Zhang, and Andrej Atrens. Hydrogen influence on some advanced high-strength steels. *Corrosion Science*, 125:114–138, 2017.

[199] Sandeep Kumar Dwivedi and Manish Vishwakarma. Hydrogen embrittlement in different materials: A review. *International Journal of Hydrogen Energy*, 43(46): 21603–21616, 2018.

[200] EV Chatzidouros, A Traidia, RS Devarapalli, DI Pantelis, TA Steriotis, and M Jouiad. Effect of hydrogen on fracture toughness properties of a pipeline steel under simulated sour service conditions. *International Journal of Hydrogen Energy*, 43(11):5747–5759, 2018.

[201] P Fassina, Maria Francesca Brunella, Luciano Lazzari, G Re, Laura Vergani, and Augusto Sciuccati. Effect of hydrogen and low temperature on fatigue crack growth of pipeline steels. *Engineering Fracture Mechanics*, 103:10–25, 2013.

[202] Nicholas Nanninga, Andrew Slifka, Yaakov Levy, and Calvin White. A review of fatigue crack growth for pipeline steels exposed to hydrogen. *Journal of research of the national institute of standards and technology*, 115(6):437, 2010.

[203] Andrew J Slifka, Elizabeth S Drexler, Nicholas E Nanninga, Yaakov S Levy, J David McColskey, Robert L Amaro, and April E Stevenson. Fatigue crack growth of two pipeline steels in a pressurized hydrogen environment. *Corrosion Science*, 78: 313–321, 2014.

[204] Druce P Dunne, Daniel Hejazi, Ahmed A Saleh, Ayesha J Haq, Andrzej Calka, and Elena V Pereloma. Investigation of the effect of electrolytic hydrogen charging of x70 steel: I. the effect of microstructure on hydrogen-induced cold cracking and blistering. *international journal of hydrogen energy*, 41(28):12411–12423, 2016.

[205] MA Mohtadi-Bonab, JA Szpunar, R Basu, and M Eskandari. The mechanism of failure by hydrogen induced cracking in an acidic environment for api 5l x70 pipeline steel. *International journal of hydrogen energy*, 40(2):1096–1107, 2015.

[206] Lei Zhang, Hongjie Shen, Kuangda Lu, Wenhai Cao, Yanni Sun, Yichen Fang, Yunying Xing, Yanxia Du, and Minxu Lu. Investigation of hydrogen concentration and hydrogen damage on api x80 steel surface under cathodic overprotection. *International Journal of Hydrogen Energy*, 42(50):29888–29896, 2017.

[207] XueChong Ren, QingJun Zhou, WuYang Chu, JinXu Li, YanJing Su, and LiJie Qiao. The mechanism of nucleation of hydrogen blister in metals. *Chinese Science Bulletin*, 52:2000–2005, 2007.

[208] XC Ren, QJ Zhou, GB Shan, WY Chu, JX Li, YJ Su, and LJ Qiao. A nucleation mechanism of hydrogen blister in metals and alloys. *Metallurgical and materials transactions A*, 39:87–97, 2008.

[209] S Ayadi, Y Charles, M Gaspérini, I Caron Lemaire, and T Da Silva Botelho. Effect of loading mode on blistering in iron submitted to plastic prestrain before hydrogen cathodic charging. *international journal of hydrogen energy*, 42(15):10555–10567, 2017.

[210] D Pérez Escobar, C Miñambres, L Duprez, Kim Verbeken, and Marc Verhaege. Internal and surface damage of multiphase steels and pure iron after electrochemical hydrogen charging. *Corrosion Science*, 53(10):3166–3176, 2011.

[211] M Elboujdaini and RW Revie. Metallurgical factors in stress corrosion cracking (scc) and hydrogen-induced cracking (hic). *Journal of solid state electrochemistry*, 13(7): 1091–1099, 2009.

[212] Goutam Ghosh, Paul Rostron, Rajnish Garg, and Ashoutosh Panday. Hydrogen induced cracking of pipeline and pressure vessel steels: A review. *Engineering Fracture Mechanics*, 199:609–618, 2018.

[213] CA Zapffe and CE Sims. Hydrogen embrittlement, internal stress and defects in steel. *Trans. Aime*, 145(1941):225–271, 1941.

[214] Ren Xuechong, Shan Guangbin, Chu Wuyang, Su Yanjing, Gao Kewei, Qiao Lijie, Jiang Bo, Chen Gang, and Cui Yinhui. Initiating, growing and cracking of hydrogen blisters. *Chinese science bulletin*, 50:1962–1965, 2005.

[215] Axel Griesche, Eitan Dabah, Thomas Kannengiesser, Nikolay Kardjilov, André Hilger, and Ingo Manke. Three-dimensional imaging of hydrogen blister in iron with neutron tomography. *Acta Materialia*, 78:14–22, 2014.

[216] MA Mohtadi-Bonab, M Eskandari, and JA Szpunar. Role of cold rolled followed by annealing on improvement of hydrogen induced cracking resistance in pipeline steel. *Engineering Failure Analysis*, 91:172–181, 2018.

[217] Rosalia Rementeria, Lucia Morales-Rivas, Matthias Kuntz, Carlos Garcia-Mateo, Eberhard Kerscher, Thomas Sourmail, and Francisca G Caballero. On the role of microstructure in governing the fatigue behaviour of nanostructured bainitic steels. *Materials Science and Engineering: A*, 630:71–77, 2015.

[218] Maria Natalia Batista, María Cecilia Marinelli, and I Alvarez-Armas. Effect of initial microstructure on surface relief and fatigue crack initiation in aisi 410 ferritic-martensitic steel. *Fatigue & Fracture of Engineering Materials & Structures*, 42(1):61–68, 2019.

[219] Y Nishimura, K Yanase, Y Ikeda, Y Tanaka, N Miyamoto, S Miyakawa, and M Endo. Fatigue strength of spring steel with small scratches. *Fatigue & Fracture of Engineering Materials & Structures*, 41(7):1514–1528, 2018.

[220] Bernd M Schönbauer, Keiji Yanase, and Masahiro Endo. The influence of various types of small defects on the fatigue limit of precipitation-hardened 17-4ph stainless steel. *Theoretical and applied fracture mechanics*, 87:35–49, 2017.

[221] Ulrich Krupp. *Fatigue crack propagation in metals and alloys: microstructural aspects and modelling concepts*. Wiley Online Library, 2007.

[222] S Pearson. Initiation of fatigue cracks in commercial aluminium alloys and the subsequent propagation of very short cracks. *Engineering Fracture Mechanics*, 7(2): 235–247, 1975.

[223] S Suresh and RO Ritchie. Propagation of short fatigue cracks. *International metals reviews*, 29(1):445–475, 1984.

[224] Bo Alfredsson, Martin Öberg, and J Lai. Propagation of physically short cracks in a bainitic high strength bearing steel due to fatigue load. *International Journal of Fatigue*, 90:166–180, 2016.

[225] Rajwinder Singh, Amanjot Singh, Pawan K Singh, and Dhiraj K Mahajan. Role of prior austenite grain boundaries in short fatigue crack growth in hydrogen charged rpv steel. *International Journal of Pressure Vessels and Piping*, 171:242–252, 2019.

[226] Volker Schippl, Sven Brück, Hans-Jürgen Christ, Claus-Peter Fritzen, Martina Schwarz, and Stefan Weihe. Modeling of hydrogen effects on short crack propagation in a metastable austenitic stainless steel (x2crni19-11). In *MATEC Web of Conferences*, volume 165, page 22005. EDP Sciences, 2018.

[227] MA Mohtadi-Bonab, J Aa Szpunar, L Collins, and R Stankievech. Evaluation of hydrogen induced cracking behavior of api x70 pipeline steel at different heat treatments. *International journal of hydrogen energy*, 39(11):6076–6088, 2014.

[228] TY Jin, ZY Liu, and YF Cheng. Effect of non-metallic inclusions on hydrogen-induced cracking of api5l x100 steel. *International Journal of Hydrogen Energy*, 35(15):8014–8021, 2010.

[229] RA Oriani and PH Josephic. Effects of hydrogen on the plastic properties of medium-carbon steels. *Metallurgical Transactions A*, 11:1809–1820, 1980.

[230] XQ Wu and In Sup Kim. Effects of strain rate and temperature on tensile behavior of hydrogen-charged sa508 cl. 3 pressure vessel steel. *Materials Science and Engineering: A*, 348(1-2):309–318, 2003.

[231] De-jun Kong, Yong-zhong Wu, and LONG Dan. Stress corrosion of x80 pipeline steel welded joints by slow strain test in nace h2s solutions. *Journal of Iron and Steel Research, International*, 20(1):40–46, 2013.

[232] Timing Zhang, Weimin Zhao, Tingting Li, Yujiao Zhao, Qiushi Deng, Yong Wang, and Wenchun Jiang. Comparison of hydrogen embrittlement susceptibility of three cathodic protected subsea pipeline steels from a point of view of hydrogen permeation. *Corrosion Science*, 131:104–115, 2018.

[233] Marie C Tiegel, May L Martin, Annegret K Lehmberg, Martin Deutges, Christine Borchers, and Reiner Kirchheim. Crack and blister initiation and growth in purified iron due to hydrogen loading. *Acta Materialia*, 115:24–34, 2016.

[234] Motomichi Koyama, Cemal Cem Tasan, Eiji Akiyama, Kaneaki Tsuzaki, and Dierk Raabe. Hydrogen-assisted decohesion and localized plasticity in dual-phase steel. *Acta Materialia*, 70:174–187, 2014.

[235] K Obrtlík, J Polák, M Hájek, and A Vašek. Short fatigue crack behaviour in 316l stainless steel. *International journal of fatigue*, 19(6):471–475, 1997.

[236] Vishal Singh, Rajwinder Singh, Amanjot Singh, and Dhiraj K Mahajan. Tracking hydrogen embrittlement using short fatigue crack behavior of metals. *Procedia Structural Integrity*, 13:1427–1432, 2018.

[237] ER De los Rios, ZY Sun, and KJ Miller. The effect of hydrogen on short fatigue crack growth in an al-li alloy. *Fatigue & Fracture of Engineering Materials & Structures*, 16(12):1299–1308, 1993.

Chapter A

Appendices

A.1 Appendix-I

The interaction matrix for FCC is given below, where A2, A3, A6, B2, B4, B5, C1, C3, C5, D1, D4, D6 are the considered slip systems as per Schmid and Boas notation. A, B, C and D corresponds to $(\bar{1}11), (111), (\bar{1}\bar{1}1)$, and $(1\bar{1}1)$ slip planes, whereas integers 1 to 6 are representing $[011], [0\bar{1}1], [101], [\bar{1}01][\bar{1}10]$ and $[110]$ slip directions, respectively [69].

	A2	A3	A6	B2	B4	B5	C1	C3	C5	D1	D4	D6
$A2$	a_0	a_1	a_1	a_3	a_4	a_4	a_2	a_4	a_5	a_2	a_5	a_4
$A3$		a_0	a_1	a_4	a_2	a_5	a_4	a_3	a_4	a_5	a_2	a_4
$A6$			a_0	a_4	a_5	a_2	a_5	a_4	a_2	a_4	a_4	a_3
$B2$				a_0	a_1	a_1	a_2	a_5	a_4	a_2	a_4	a_5
$B4$					a_0	a_1	a_5	a_2	a_4	a_4	a_3	a_4
$B5$						a_0	a_4	a_4	a_3	a_5	a_4	a_2
$C1$							a_0	a_1	a_1	a_3	a_5	a_4
$C3$								a_0	a_1	a_4	a_2	a_5
$C5$									a_0	a_4	a_5	a_2
$D1$										a_0	a_1	a_1
$D4$											a_0	a_1
$D6$												a_0

A.2   Appendix-II

The summary of governing equations and boundary conditions for the coupled displacement-diffusion problem solved in Chapter 2 is as follows,

1. The equation of local macroscopic force balance in a quasi-static state and in the absence of body forces is,

$$\boldsymbol{\nabla}.\boldsymbol{\sigma} = 0 \qquad \text{in } \Omega \tag{A.1}$$

where, $\boldsymbol{\sigma}$ is the Cauchy stress tensor obtained using push forward approach as $\boldsymbol{\sigma} = J^{e^{-1}}\mathbf{F}_e\mathbf{S}\mathbf{F}_e^T$, with $\mathbf{S}(= \mathcal{C}^e : \mathbf{E}^e)$ as the second Piola stress tensor. Denoting, $\partial\Omega_u$ and $\partial\Omega_t$ as complementary segments of the boundary $\partial\Omega$ of Ω in the deformed configuration such that $\partial\Omega_u \cup \partial\Omega_t = \partial\Omega$ and $\partial\Omega_u \cap \partial\Omega_t = \emptyset$. Then for a time interval of $t \in [0,T]$, a pair of boundary conditions in which the displacement $\boldsymbol{u}$ is specified on $\partial\Omega_u$ and the surface traction on $\partial\Omega_t$ are considered as,

$$\boldsymbol{u} = \bar{\boldsymbol{u}} \qquad \text{on } \partial\Omega_u \times [0,T] \tag{A.2}$$

$$\boldsymbol{\sigma}.\boldsymbol{n} = \bar{\boldsymbol{t}} \qquad \text{on } \partial\Omega_t \times [0,T] \tag{A.3}$$

where, $\boldsymbol{n}$ is the outer normal to the boundary $\partial\Omega$.

2. The equation for the balance of hydrogen concentration is,

$$\left(1 + \sum_{\alpha=1}^{N_s} \frac{\partial C_T^\alpha}{\partial C_L}\right) \frac{\partial C_L}{\partial t} - \boldsymbol{\nabla}.(D_L\boldsymbol{\nabla}C_L) + \boldsymbol{\nabla}.\left(\frac{D_LC_LV_H}{RT}\boldsymbol{\nabla}\sigma_H\right)$$
$$+ \sum_{\alpha=1}^{N_s}\left(\theta_T^\alpha \frac{\partial N_T^\alpha}{\partial\rho^\alpha}\frac{\partial\rho^\alpha}{\partial\gamma^\alpha}|\dot{\gamma}^\alpha|\right) = 0 \; in \; \Omega \tag{A.4}$$

Denoting, the $\partial\Omega_{C_L}$ and $\partial\Omega_j$ be the complementary segments of $\partial\Omega$ such that $\partial\Omega_{C_L} \cup \partial\Omega_j = \partial\Omega$ and $\partial\Omega_{C_L} \cap \partial\Omega_j = \emptyset$. A pair of boundary conditions considering the lattice hydrogen concentration specified on $\partial\Omega_{C_L}$ and the lattice hydrogen flux on $\partial\Omega_j$ are considered as,

$$C_L = \bar{C}_L \qquad \text{on } \partial\Omega_{C_L} \times [0,\text{T}] \tag{A.5}$$

$$\boldsymbol{J}.\boldsymbol{n} = j \qquad \text{on } \partial\Omega_j \times [0,\text{T}] \tag{A.6}$$

Details regarding the implementation of the coupled displacement-diffusion problem by using UMAT and UMATHT subroutines in Abaqus can be found in [18, 21, 76, 124].

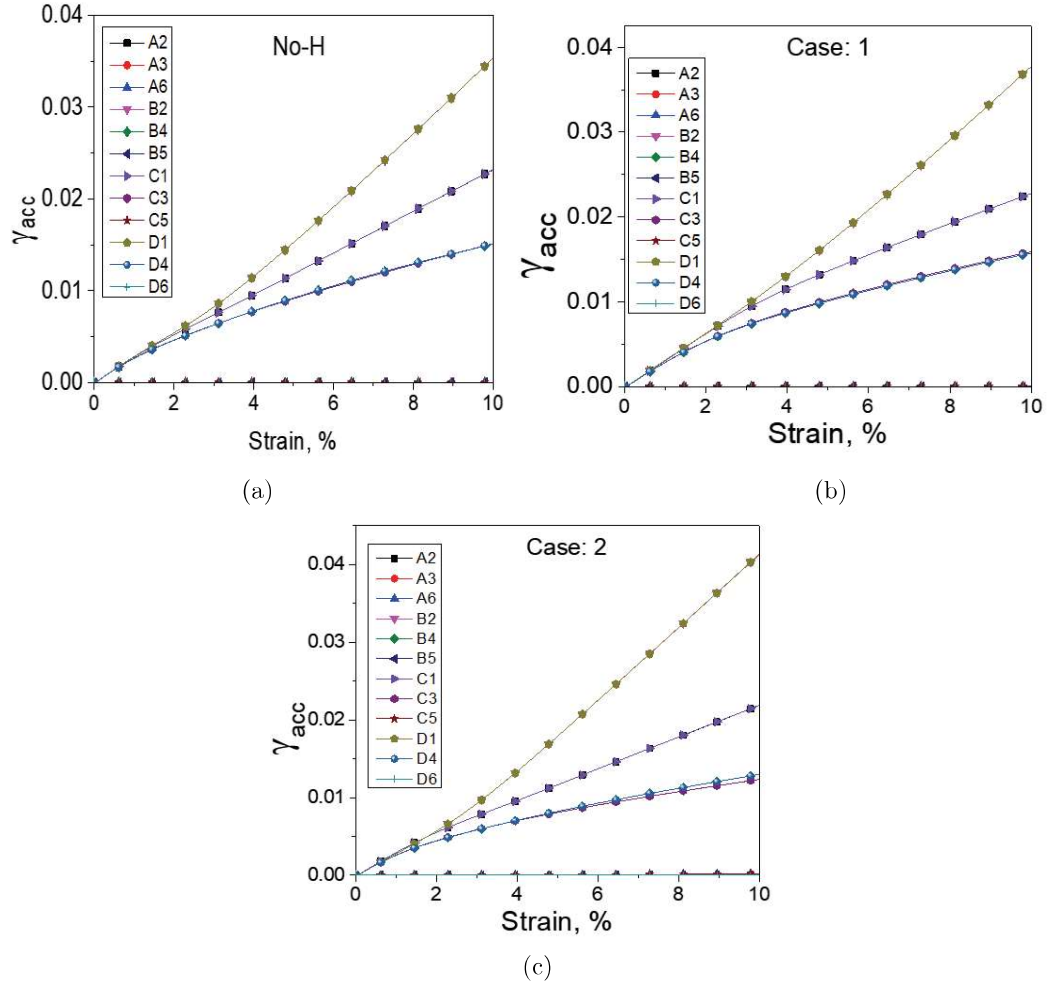## A.3 Appendix-III

(a)

(b)

(c)

Figure A.1: Evolution of accumulated slip during deformation of single crystal oriented for multi-slip (a) without hydrogen (No-H), and with hydrogen for (b) Case 1, and (c) Case 2. Note that in these figures, there is overlap between the active slip systems (i.e., D1 is overlapped with B2, A2 is overlapped with C1, and A3, B4, C3, and D4 overlap with each other).
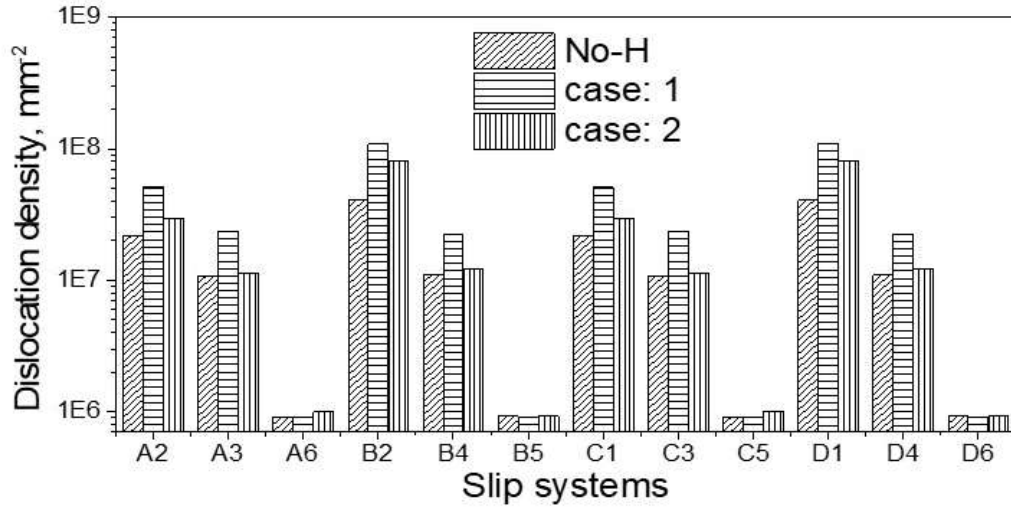
Figure A.2: Dislocation density on various slip systems at the end of deformation for single crystal with multi-slip orientation for without (No-H) and with hydrogen (Case 1 and Case 2)

A.4 Appendix-IV

The summary of governing equations and boundary conditions for the coupled displacement-phase field fracture problem solved in Chapter 5 is as follows,

1. The equation of local macroscopic force balance in a quasi-static state and in the absence of body forces is,

$$\boldsymbol{\nabla}.\boldsymbol{\sigma} = 0 \qquad \text{in } \Omega \tag{A.7}$$

where, $\boldsymbol{\sigma}$ is the Cauchy stress tensor obtained using push forward approach as $\boldsymbol{\sigma} = J^{e^{-1}}\mathbf{F}_e\mathbf{S}\mathbf{F}_e^T$, with $\mathbf{S} = (g(\phi)\mathcal{C}^e : \mathbf{E}^e)$ as the second Piola stress tensor. Denoting, $\partial\Omega_u$ and $\partial\Omega_t$ as complementary segments of the boundary $\partial\Omega$ of Ω in the deformed configuration such that $\partial\Omega_u \cup \partial\Omega_t = \partial\Omega$ and $\partial\Omega_u \cap \partial\Omega_t = \emptyset$. Then for a time interval of $t \in [0, T]$, a pair of boundary conditions in which the displacement $\boldsymbol{u}$ is specified on $\partial\Omega_u$ and the surface traction on $\partial\Omega_t$ are considered as,

$$\boldsymbol{u} = \bar{\boldsymbol{u}} \qquad \text{on } \partial\Omega_u \times [0, T] \tag{A.8}$$

$$\boldsymbol{\sigma}.\boldsymbol{n} = \bar{\boldsymbol{t}} \qquad \text{on } \partial\Omega_t \times [0, T] \tag{A.9}$$

where, $\boldsymbol{n}$ is the outer normal to the boundary $\partial\Omega$.

2. The balance equation for the phase-field fracture parameter is,

$$\left\langle \left(-\frac{\partial\psi^e}{\partial\phi} - \frac{\partial\psi^p}{\partial\phi} \right) - 2w_c(1 - \phi) \right\rangle_+ - 2w_c\phi + 2w_c l_\phi^2 \boldsymbol{\nabla}.[\boldsymbol{\nabla}\phi] = 0 \tag{A.10}$$

Denoting the $\partial\Omega_\phi$ and $\partial\Omega_\zeta$ as the boundary $\partial\Omega$ of Ω such that $\partial\Omega_\phi \cup \partial\Omega_\zeta = \partial\Omega$ and $\partial\Omega_\phi \cap \partial\Omega_\zeta = \emptyset$. The boundary conditions for the evolution of ϕ are:

$$\phi = \bar{\phi} \quad \text{on } \partial\Omega_\phi \times [0, T] \tag{A.11}$$

$$\boldsymbol{\nabla}\phi \cdot \boldsymbol{n} = 0 \quad \text{on } \partial\Omega_\zeta \times [0, T] \tag{A.12}$$

Details regarding the implementation of the staggered algorithm in Abaqus using UMAT and UEL subroutines can be found in [158, 186].